Nanostructured materials



2001 Rep. Prog. Phys. 64 297

(http://iopscience.iop.org/0034-4885/64/3/201)

INSTITUTE OF PHYSICS PUBLISHING REPORTS ON PROGRESS IN PHYSICS

Rep. Prog. Phys. **64** (2001) 297–381 www.iop.org/Journals/rp PII: S0034-4885(01)04041-6

# Nanostructured materials

**Philip Moriarty**[1]

School of Physics and Astronomy, University of Nottingham, Nottingham NG7 2RD, UK

E-mail: philip.moriarty@nottingham.ac.uk

Received 7 September 2000

## Abstract

Nanostructured materials may be defined as those materials whose structural elements—clusters, crystallites or molecules—have dimensions in the 1 to 100 nm range. The explosion in both academic and industrial interest in these materials over the past decade arises from the remarkable variations in fundamental electrical, optical and magnetic properties that occur as one progresses from an 'infinitely extended' solid to a particle of material consisting of a countable number of atoms. This review details recent advances in the synthesis and investigation of functional nanostructured materials, focusing on the novel size-dependent physics and chemistry that results when electrons are confined within nanoscale semiconductor and metal clusters and colloids. Carbon-based nanomaterials and nanostructures including fullerenes and nanotubes play an increasingly pervasive role in nanoscale science and technology and are thus described in some depth. Current nanodevice fabrication methods and the future prospects for nanostructured materials and nanodevices are discussed.

[1] http://www.ccc.nottingham.ac.uk/p̃pzstm/home.html.

0034-4885/01/030297+85$90.00  

## Contents

## 1. Introduction and scope of the review

Although it is now almost traditional to quote from R P Feynman's visionary 1959 lecture *'There is plenty of room at the bottom'* (Feynman 1959) when introducing the topic of nanoscale science and nanotechnology, perhaps the following statement from the US President's Advisor for Science and Technology more topically highlights the widely perceived potential of nanoscale science in the coming decades:

> 'If I were asked for an area of science and engineering that will most likely produce the breakthroughs of tomorrow, I would point to nanoscale science and engineering'. (*A Lane*, from the introduction to *National Nanotechnology Initiative: Leading to the Next Industrial Revolution*, US National Science and Technology Council, February 2000[2]).

The US National Nanotechnology Initiative was announced on 21 January 2000 and will bring the US government's investment in nanoscale science to a total of $500 million in the 2001 financial year (an increase of 83% compared with 2000). The US initiative follows a Japanese project of comparable focus, *Research and Development of Ultimate Manipulation of Atoms and Molecules*, a 25 billion yen, ten-year programme that started in 1992 and involved the construction of the Joint Research Centre for Atom Technology (JRCAT). Similar nanoscience initiatives have been funded throughout Europe, in the form of both national programmes and as international collaborations (including the ESPRIT *Microelectronics Research Initiative* and the *PHANTOMS (Physics and Technology of Mesoscale Systems*) and *PRONANO (Synthesis and Processing of Nanoparticle Materials)* Networks of Excellence). Indeed, in the UK, the National Initiative on Nanotechnology (NION) was established by the National Physical Laboratory and the Department of Trade and Industry 'as long ago' as 1986 to promote the awareness of nanometre-scale science and engineering.

Why has nanoscience attracted such intense global interest? To answer this, a broad definition and brief description of the field are required. Nanoscale science, engineering and technology are concerned with the manipulation of matter on the nanometre length scale, which is now generally taken as the 1 to 100 nm range. Although nanoscience might simply be seen as a natural and necessary progression from the (sub)micron-scale engineering that has driven the microelectronics and computing industries thus far, it is not merely the trend towards higher levels of miniaturization but the wealth of novel physical, chemical and biological behaviour that occurs on the nanometre scale that makes nanoscience such a fundamentally exciting and technologically relevant area of research.

The length scales appropriate to nanoscience are such that the field might be thought of as 'straddling' solid-state and atomic/molecular physics and chemistry. That is, instead of dealing with an 'infinitely' extended solid or *individual* atoms and molecules, nanoscience is concerned with the properties, interactions and processing of units containing a countable number of atoms. These units—whether they are, for example, clusters of atoms (quantum dots), fullerenes, carbon nanotubes or biomolecules—have novel electronic, optical and chemical properties by virtue of their nanometre dimensions. Furthermore, by varying the size of the units and—equally importantly—controlling their interactions, the fundamental properties of nanostructured materials synthesized from these building blocks may be tuned.

The synthesis of a material from nanoscale building blocks—'building from the bottom up'—differs radically from the 'top-down', lithographic approach conventionally used to fabricate submicron devices both industrially and in the majority of experimental solid-state and low-dimensional physics. In '*There is Plenty of Room at the Bottom*' (Feynman

[2] The full text of the report is available at http://itri.loyola.edu/nano/IWGN/#reports.

1959) Feynman noted that nanometre-scale engineering would require the development of complex instrumentation that could act as our 'eyes' and 'fingers' in the nanoworld. This vision was realized in the early 1980s by the invention of the scanning tunnelling microscope (STM) (Binnig *et al* 1982a, b), an instrument that exploits the quantum mechanical tunnel current flowing between a sharp metal tip and a conducting substrate to generate atomically resolved surface images. A family of related scanning probe instruments (including the atomic force microscope (AFM), magnetic force microscope (MFM) and scanning near-field optical microscope (SNOM)) were developed in the decade following the invention of the STM (see Wiesendanger (1994) and Stroscio and Kaiser (1993) for detailed accounts of scanning probe instrumentation and science). With each new scanning probe instrument came a new method of investigating material properties at the nanometre level. It is thus widely accepted that scanning probe microscopes (SPM) heralded the emergence of nanoscience and nanotechnology.

With the STM, not only is it possible to image atoms or molecules at—or adsorbed on—a surface, but, by careful control of tip–surface interactions, individual adsorbates may be controllably positioned. Eigler and Schweizer pioneered STM-based atomic-scale engineering in 1990, when they positioned Xe atoms adsorbed on a Ni surface to 'write' the letters *IBM* (Eigler and Schweizer (1990), figure 1(a)). Eigler's group has since extended that work to carry out a series of beautiful experiments which exploit the free-electron-like properties of the Cu(111) surface states to form quantum corrals. Figures 1(b) and 1(c) show two such corrals (formed by the manipulation of Fe atoms on Cu(111)). In figure 1(b) the eigenstate density of the corral (arising from quantum confinement of the Cu(111) electrons) is clearly visible as rings within the circular arrangement of Fe atoms (Crommie *et al* 1993) (note that somewhat similar quantization effects were observed by Avouris and Lyo in naturally formed metal islands (Avouris and Lyo 1994)). Most recently, quantum 'mirages' arising from the interaction of the spin of a ferromagnetic impurity within a corral with the spin states of the surface electrons (the Kondo effect) have been reported (figure 1(c), Manoharan *et al* (2000)).

Lee and Ho (1999) recently reported the first demonstration of molecular synthesis using an STM (i.e. the construction of a molecule by bringing together individual atoms/molecules). A CO molecule was transferred from a Ag(110) surface to the STM tip, the tip (with the transferred CO molecule) positioned over an Fe atom and, via a reversal of the direction of the electric field and the flow of tunnelling electrons, the CO molecule moved from the tip to form an Fe(CO) complex on the surface (figure 1(d)).

The STM-based atomic manipulation described in the preceding paragraphs was carried out on metal surfaces at cryogenic temperatures. Low temperatures are necessary to inhibit atomic diffusion on metals where surface diffusion barriers are small. It is only within the last few years that it has become possible to manipulate adsorbates at *room temperature (RT)* using the STM. The difficulty in achieving controlled positioning at RT arises from the relatively small number of adsorbate–substrate systems where the diffusion barrier for the adsorbate is large enough that diffusion at room temperature is inhibited yet the adsorbate–substrate bond is sufficiently weak (or the diffusion barrier still sufficiently small) that the STM tip can controllably move the adsorbate.

Adsorbed fullerene molecules (see section 7.1.3) were found to be particularly amenable to RT STM manipulation (Beton *et al* 1995a, Moriarty *et al* 1998a, b) and have been controllably positioned at the subnanometre level on both semiconducting (Si) (Beton *et al* 1995a, Moriarty *et al* 1998a, b) and metallic substrates (Cuberes *et al* 1996) (figure 1(e) and figure 1(f) respectively). The number of examples of controlled STM manipulation at room temperature not involving fullerenes remains small—to date only porphyrin molecules (Jung *et al* 1996) and halogen atoms (Fishlock *et al* 2000) on metal surfaces have been successfully positioned.

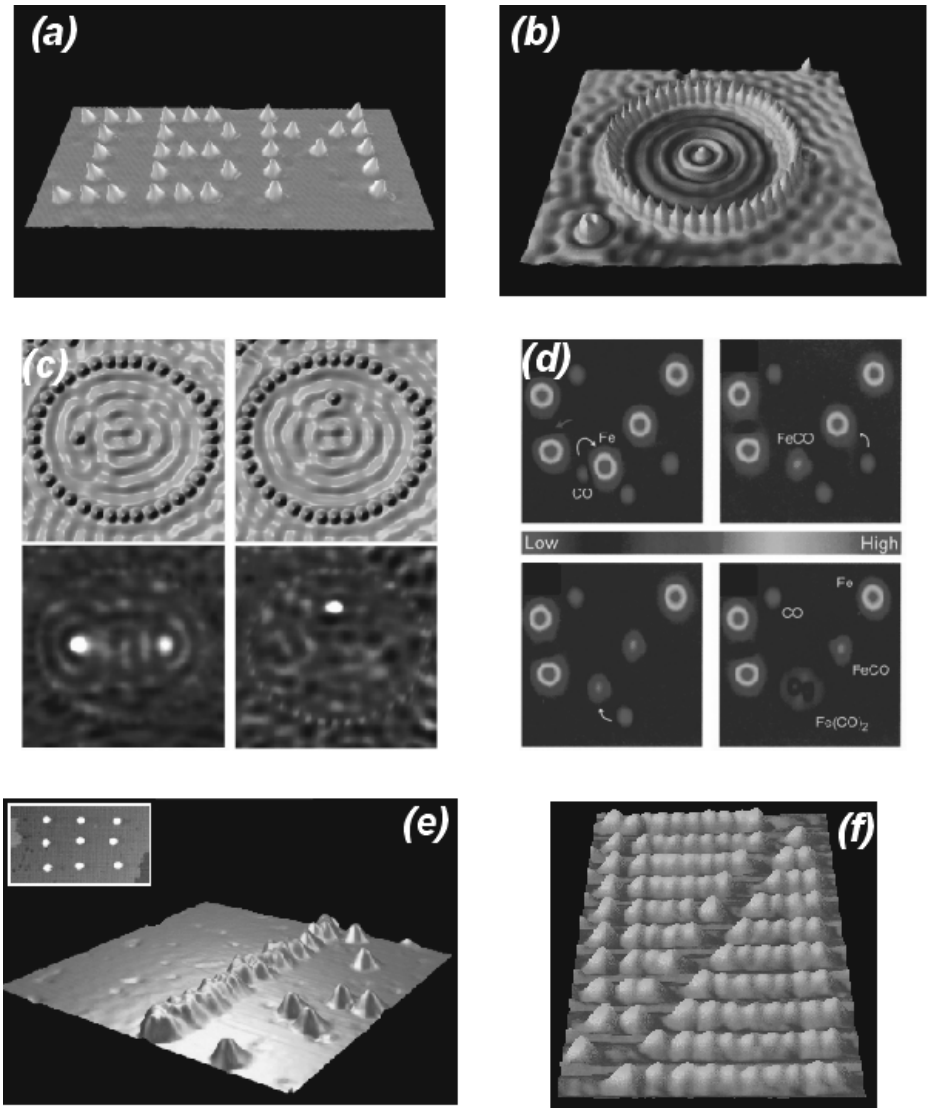


**Figure 1.** STM-constructed nanoscale and molecular structures: (a) individual Xe atoms positioned on a Ni surface at 4 K to form the *IBM* logo (Eigler and Schweizer 1990); (b) a quantum corral formed by Fe atoms on a Cu(111) surface—the ripples within the corral arise from scattering of surface state electrons (Crommie *et al* 1993); (c) quantum mirages—the upper images are conventional topographic STM data whereas the lower images are $\mathrm{d}I/\mathrm{d}V$ maps. In the topographic images on the left and right, an individual magnetic impurity (a Co atom) has been positioned within an elliptical corral formed from Co atoms. When the single Co atom is at a focus of the ellipse, the spectroscopic signature associated with the Kondo effect is projected to the other focus (the spectroscopic map on the left). When the Co atom is moved off focus the spectroscopic signature (the 'quantum mirage') vanishes the $\mathrm{d}I/\mathrm{d}V$ map on the right) (Manoharan *et al* 2000). (d) Synthesis of individual molecular complexes. Both an FeCO and an $Fe(CO)_2$ molecule have been synthesized (Lee and Ho 1999). (e) Room temperature molecular manipulation—formation of a wire of $C_{60}$ molecules ($\sim$25 nm long) on Si(100)($2 \times 1$). The inset is a 2D array of $C_{60}$ molecules on Si(100) (Moriarty *et al* 1998a, b). (f ) A molecular abacus formed from $C_{60}$ molecules aligned along a step on a Cu surface (Cuberes *et al* 1996). The figure is a composite of a number of separate images each taken following the movement of a fullerene molecule along the step edge.

The STM might therefore be thought of as the nanotechnological tool of choice in that it enables the ultimate control of matter: single atoms and molecules may be positioned with atomic-scale precision. In fundamental nanoscience, where the basic physical/chemical properties of nanometre-scale objects and the interactions of those objects with each other and their environment are of key interest, the STM (and other SPM techniques) will continue to play a pivotal role in both nanostructure fabrication and study. However, in the synthesis of nanostructured materials and the generation of commercial nanoelectronic devices, STM nanofabrication techniques have a significant drawback: they are very slow.

To improve the efficiency of SPM-based fabrication, a number of research groups have developed innovative methods of parallel feature writing with multi-tip SPM instruments (Vettiger *et al* 2000, Hang and Mirkin 2000, Cooper *et al* 1999). These methods have succeeded in producing features with linewidths of $\sim$15 nm (Hang and Mirkin 2000) and areal densities of 100–200 Gb in$^{-1}$ (Vettiger *et al* 2000). Here the goal (at least thus far) is not the construction of a structure 'from the bottom up' (i.e. where the placement of individual atoms/molecules is predetermined and carefully controlled) but the development of SPM as a patterning tool that can surpass the resolution of current lithographic techniques without sacrificing speed.

A useful analogy may be drawn between the STM atom-by-atom approach to nanostructure fabrication and the approach of synthetic chemists. In each case a rather unwieldy bottom-up strategy is used to assemble molecules from their constituent atoms. For synthetic chemistry, the syntheses tend to follow rather tortuous routes characterized by a general lack of specificity in the reactions. This lack of specificity largely precludes supramolecular organization (which although *in principle* possible using STM-based assembly is in practice ruled out due to the long timescales necessary to controllably position even a few tens of molecules). However, a wide range of natural biological systems including amino acids, nucleic acids (DNA, RNA) and viruses exhibit an unparalleled propensity for *self-assembly*, *self-organization* and *self-replication*. These latter three areas are increasingly the focus of a great deal of current nanoscientific research whose long term aim is to harness the self-organization capabilities of biomolecules to assemble functional nanostructures and nanostructured materials.

The application of biomolecular assembly processes to nanostructure synthesis is just one example of the strong cross-disciplinary character of nanoscale science and engineering. Nanoscience thrives on multidisciplinarity—in fact, it could be argued that the traditional boundaries between the physical, chemical, biological and material sciences vanish at the nanometre scale. It is this convergence of the sciences that makes nanoscience such a vibrant, exciting field and there will be many examples of the importance of cross-disciplinary research throughout this review.

In a relatively short review, it is impossible to present a comprehensive overview of *all* areas of research that may be classified under the 'nanostructured materials' banner. The choice of topics has been informed both by the author's research interests and, in the author's opinion, the most significant advances in the synthesis and understanding of the fundamental properties of nanostructured materials over the past decade. Nanoclusters are the archetypal building block for nanostructured materials and they exemplify a broad subset of the novel physics common to nanostructured systems. As such, a discussion of metallic, semiconducting and magnetic nanoclusters forms the core of this review. $C_{60}$ (buckminsterfullerene) represents the prototypical nanocluster. The fullerene family of molecules—particularly, of late, carbon nanotubes—have been at the centre of a huge research effort whose focus is an elucidation of the properties of carbon-based nanomaterials. Section 7 of the review therefore deals with recent fascinating work in this area, with a specific focus on the novel low-dimensional physics exhibited by nanotube systems.

## 2. Nanoclusters and nanocrystals

A *nanocluster* or *nanocrystal* is a fragment of solid comprising somewhere between a few atoms and a few tens of thousands of atoms. Over the past ten years huge advances have been made both in the synthesis of size-tunable, monodisperse nanoclusters of various chemical compositions and in the development of techniques for their assembly into well-ordered nanostructured solids (facilitating the synthesis of what have been termed 'designer materials'). Alongside the advances in nanocluster synthesis, spectroscopies capable of studying individual clusters have been developed and these—together with more conventional structural, electronic and optical probes—have produced detailed information on and key insights into the properties of single clusters, cluster ensembles and cluster-based materials. In the following sections a broad review of nanocluster science over the past decade is presented.

## 3. Nanocluster synthesis

On first consideration, one might imagine that a prototypical nanocluster should consist of a size-selected collection of atoms, isolated in the gas-phase and synthesized under (ultra)high-vacuum conditions (to ensure the absence of foreign chemical species either in the cluster volume or at its surface). Indeed, this is generally the case in fundamental cluster science where dedicated cluster sources are used to provide beams of nanoclusters of almost any element with sizes ranging from several atoms to several tens of thousands of atoms. As this review is concerned with nanostructured *materials* where cluster adsorption on a substrate is a prerequisite for material synthesis, free, unsupported clusters will not be discussed (however, see de Heer (1993) for an excellent review).

In fact, from the perspective of functional nanostructured materials and nanodevices the unsupported gas-phase cluster has somewhat less than ideal properties (Alivisatos 1996). This is largely due to the very high surface-to-volume ratio in nanoclusters. For example, a 1000-atom cluster will generally have approximately 25% of its atoms at the surface. This in turn means that free nanoclusters have a high density of unsatisfied, *dangling* bonds and, correspondingly, high surface free energies. The surfaces of bulk inorganic semiconductors (for example, III–V, II–VI compounds and group IV (Si, Ge) elements) generally *reconstruct* (Lüth 1997, Woodruff and Delchar 1994). That is, the atoms in the uppermost layers of the solid spontaneously rearrange and rebond to lower the dangling-bond density and, thus, reduce the surface free energy. (There are notable exceptions but we need not be concerned with those.) An unreconstructed semiconductor surface will have a high density of surface states *within* the bulk band gap (the surface states arise from the truncation of the solid and thus cannot be described by the same Bloch waves as describe the electrons in the interior of the crystal). Since the pioneering work of Bardeen (1947) it has been well established that these mid-gap surface states play a very significant role in determining the electrical and optical properties of semiconductor devices, pinning the semiconductor Fermi level and strongly reducing quantum efficiencies due to increased levels of non-radiative recombination.

High surface free energies also mean high cluster reactivities. Hence, a semiconductor cluster prepared under high-vacuum conditions will readily oxidize on exposure to the atmosphere. Again, this generally (though not always—see section 5.3) significantly degrades the electrical and optical properties of the cluster. For metallic clusters and, in particular, ferromagnetic clusters where the spin state of the cluster will be dramatically affected by contamination, oxidation and aggregation of nanoclusters created under (ultra)high vacuum and exposed to ambient conditions are particularly acute problems.

*Passivation* of the cluster surface, i.e. the termination of cluster dangling bonds with either an organic or inorganic addend, significantly reduces the chemical reactivity of the cluster and, for semiconductor clusters, may lead to a reduction in mid-gap states. Perhaps a more significant consequence of termination of the cluster surface is that the correct choice of addend can lead to an effective functionalization of the cluster. That is, intercluster interactions can be mediated by, for example, organic ligands, including, as described in 2.1.3 below, nucleic acids. Colloidal chemistry has been used extensively to synthesize nanoclusters with narrow size distributions and functionalized surfaces enabling both the formation of cluster superlattices and the controlled tethering of clusters to solid substrates.

The following sections (3.1 to 3.3) describe advances made in cluster synthesis over the last decade or so from a number of perspectives. In each case the emphasis will be on the use of these methods to prepare nanostructured materials or 'precursors' to nanostructured materials such as cluster aggregates or cluster films.

### *3.1. Gas-phase cluster synthesis*

By 'gas-phase' cluster synthesis, we mean processes whereby clusters are formed in the gas phase (so-called 'pre-formed' clusters) prior to their deposition on a solid substrate. These methods include gas aggregation, laser vaporization or ion sputtering which may be by cluster mass selection using quadrupole mass filtration or time-of-flight mass spectrometry. Space constraints prohibit a detailed description of the various types of cluster source. However, de Heer (1993) discusses gas-phase cluster synthesis in considerable detail and the reader is referred to that work for a comprehensive discussion of cluster source instrumentation.

Graphite, due to its extreme inertness and ease of preparation, has been a popular choice of substrate for the deposition of pre-formed clusters. Cluster–surface interactions (which will largely determine the morphology and therefore the functionality of cluster-assembled thin films) and, in particular, dynamics have proved to be rather complex, with cluster diffusion and coalescence attracting particular attention. Bardotti *et al* (1995) have shown that Sb clusters with as many as 2300 atoms are mobile on graphite, forming ramified islands (see figure 2(a)) with branch widths equivalent to the deposited cluster size. On the basis of earlier work on cluster diffusion (Kern *et al* 1979) the authors suggested that the large values of diffusion coefficients they observed for the Sb clusters could only be explained by invoking a mechanism involving collective motion of the cluster atoms as opposed to single-atom diffusion processes.

Yoon *et al* (1999) have recently extended the investigation of Sb cluster adsorption to amorphous carbon and ion-bombarded graphite substrates and to a wider range of cluster sizes. The effect of cluster size variation is clearly shown in figure 2(b) where Yoon *et al* find that only for the largest clusters studied (2300-atom clusters) are the branch widths equal to the diameters of the incident clusters. They interpret these results in terms of a competition between the cluster coalescence time and collision interval time.

Somewhat similar ramified islands have been observed following deposition of size-selected Ag clusters (ranging from 50 to 250 atoms/cluster) on graphite (Goldby *et al* 1996). However, the authors of that study observed ramified clusters only at the edges of the sample where, they argued, the experimental conditions were such that the clusters leaving the source and impinging on the edge of the sample had an enhanced component of momentum parallel to the surface, leading to higher diffusion rates. Towards the centre of the sample, island diameters, regardless of the initial deposited cluster size, were uniformly $\sim$14 nm. This 'universal' cluster size was explained in terms of strain arising from the lattice mismatch between the island/cluster and graphite lattices. The authors argued that island growth

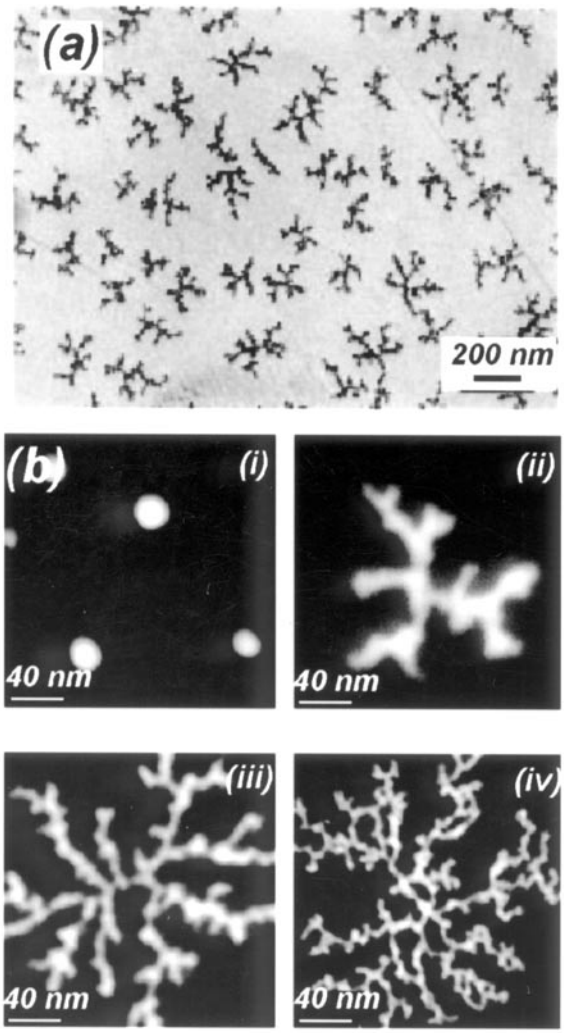


**Figure 2.** (a) Fractal islands formed following the deposition of Sb clusters on graphite (Bardotti *et al* 1995). (b) Scanning transmission electron microscope (STEM) images of the islands formed from Sb clusters of various sizes deposited onto graphite. The average number of atoms per deposited cluster, $\langle n \rangle$, in each case is: (i) 4, (ii) 90, (iii) 150, (iv) 500 (Yoon *et al* 1999).

seemingly halts at a diameter of 14 nm because smaller islands will have larger ratios of edge length to island area and strain energy can be more effectively relieved along the island edges.

The Ag cluster/graphite work was extended to deposition onto stepped graphite surfaces. Carroll *et al* (1998b) found that $Ag_{400}$ clusters preferentially adsorbed at the step edges (see figure 3) where C dangling bonds are expected. Statistical and theoretical analyses of the interparticle separations along the step edges strongly suggested that the cluster–step interaction was not of the 'hit and stick' type but that the clusters had limited mobility along the step edges. Most recently this group has examined the interaction of size-selected, ionized Ag clusters with graphite over a range of impact energies (15–1500 eV) finding that cluster penetration into graphite requires that a large proportion of the incident cluster's kinetic energy must be 'focused' onto a single C atom (Carroll *et al* 1998a).

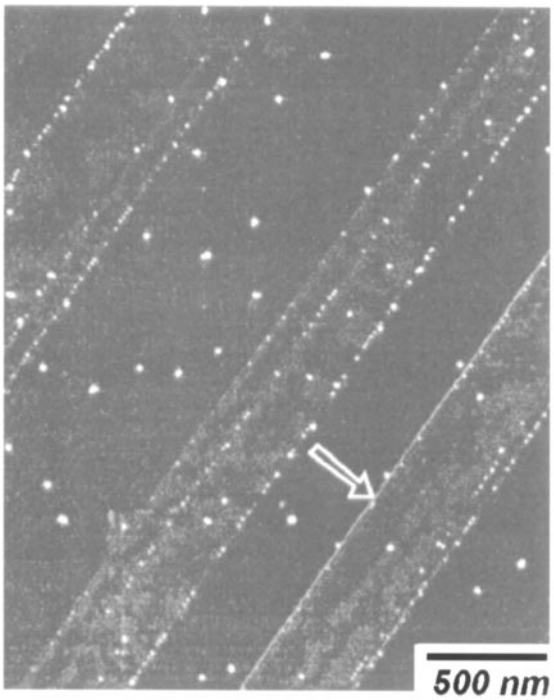


**Figure 3.** An SEM micrograph of $Ag_{400}$ clusters deposited at 500 eV onto graphite and preferentially adsorbed at step edges. The arrow points to a step edge (Carroll *et al* 1998b).

Binns *et al* (1999) have carried out a comprehensive study of the interaction of transition metals with graphite surfaces. Both Fe and Mn (non-size-selected) nanoclusters, formed in a gas aggregation source (Baker *et al* 1997) and having a most probable diameter of ∼2.5 nm, have been deposited not only onto graphite but also onto clean Si(111)(7×7) and $C_{60}$-terminated Si(111) surfaces (Upward *et al* 1997b). Figure 4 illustrates that Mn clusters do not diffuse on either of the latter surfaces. Annealing the Mn cluster/Si(111)(7 × 7) sample up to temperatures

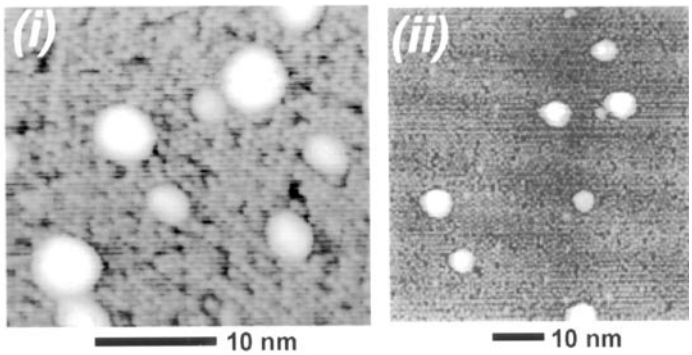


**Figure 4.** STM images of pre-formed Mn clusters (synthesized in a gas aggregation source) adsorbed on a Si(111)(7 × 7) and a 1 ML $C_{60}$/Si(111) surface. No evidence for cluster diffusion is observed in either case (Upward *et al* 1997b).

of 600 °C produced no change in either the positions or size distribution of the clusters (Upward *et al* 1997b), indicating that the cluster–surface interaction was considerably stronger than that observed in the studies discussed in the preceding paragraphs.

Silicon clusters have been the focus of an increasing number of studies since the observation of visible light emission from HF-etched nanoporous Si at the start of the 1990s (Canham 1990). Si cluster studies are being used to address fundamental issues such as the relationship between cluster size, cluster structure and luminescence wavelength/quantum efficiency. (See section 5 for a discussion of the optical properties of clusters.) Laser ablation with post-deposition annealing (Dinh *et al* 1994), $CO_2$ laser-induced decomposition of $SiH_4$ (Huisken *et al* 1999) and magnetron sputtering (Scheier *et al* 2000) are among some of the methods used to produce Si clusters. Littau *et al* (1993) have developed an aerosol apparatus that produces 3–8 nm, surface-oxidized Si crystallites (as described in section 5.3, surface oxidation and passivation play a very important role in determining the optical properties of Si nanoclusters).

Si nanocrystals have been deposited onto a number of substrates including Au(001) (Kuk *et al* 1989), graphite (Scheier *et al* 2000, Dinh *et al* 1994, Marsen and Sattler 1999) and Si(111) (McComb *et al* 1996). The latter substrates, graphite and Si(111), represent two extremes of reactivity with significant differences in Si cluster sticking coefficient being observed for defect-free and defect-rich regions of the graphite surface. Figure 5 is an STM image of (non-mass-selected) Si clusters on Si(111)(7 × 7). Although, as pointed out by the authors, both STM tip convolution effects and the 'mixture' of electronic and topographic information present in an STM image somewhat complicate the analysis of cluster structure, it is clear that the uppermost atoms of the cluster on the left-hand side of the image are resolved. Unlike the case for the graphite surface and similarly to in the studies of transition metal cluster adsorption on Si(111)(7 × 7) discussed above (Upward *et al* 1997b), the Si clusters do not diffuse following deposition onto the room temperature substrate. Annealing at 700 K resulted in the conversion of the clusters to epitaxial 2D islands.

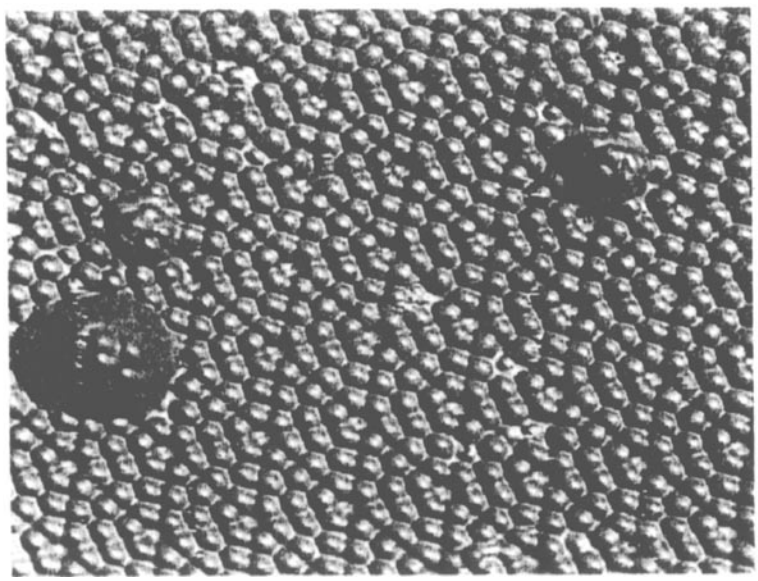

**Figure 5.** Si nanoclusters adsorbed on Si(111)(7 × 7). The atomic structure of the top surface of the cluster on the left-hand side of the image is discernible (McComb *et al* 1996).

The deposition of compound semiconductor (pre-formed) nanoclusters onto substrates has received somewhat less attention. Dinh *et al* (1999) have used laser ablation (with a 400 W, 50 ns pulse length, Cu-vapour laser) in high vacuum and in an inert background gas to produce two-micron-thick films of 14 nm diameter (standard deviation 4 nm) GaAs clusters on a Si(100) wafer. They found that only for ablation in the inert gas were crystalline clusters formed and that these were capped with As-rich oxide shells following exposure to air. Size-selected GaAs particles (30 nm diameter) have also been formed by an aerosol technique and deposited onto GaAs substrates where they have been controllably manipulated using an AFM (Junno *et al* 1995).

### *3.2. Self-assembled clusters on surfaces: Stranski–Krastanov and Vollmer–Weber growth modes*

Throughout the 1970s and 1980s low-dimensional semiconductor structures were generally fabricated using a combination of molecular beam epitaxy, electron beam lithography and etching. The GaAs/$Al_xGa_{1-x}As$ materials system was (and still is) used extensively, since the band gap can be tuned via compositional changes in the tertiary alloy and because of the lattice matching of the two materials (Weisbuch and Vinter 1991). With a sufficiently thin GaAs layer—i.e. the GaAs layer thickness less than the carrier de Broglie wavelength—sandwiched between two layers of AlGaAs, electrons are confined to two dimensions within the potential well formed from the band offsets of the two materials. Lithography and etching may then be used to further confine the electrons to one or, ultimately, zero dimensions forming a quantum wire or a quantum dot respectively. (See section 4 for a discussion of carrier confinement in semiconductor nanostructures.)

Lithography and etching-based fabrication of defect-free quantum dots that have an abrupt confinement potential is technologically challenging. There was therefore considerable excitement generated in the semiconductor and low-dimensional physics communities by the realization that a combination of lattice-*mismatched* materials could be exploited to form nanometre-scale islands (i.e. nanoclusters or quantum dots) with a narrow size distribution. Figure 6 schematically illustrates the Stranski–Krastanov (SK) growth mode exploited in

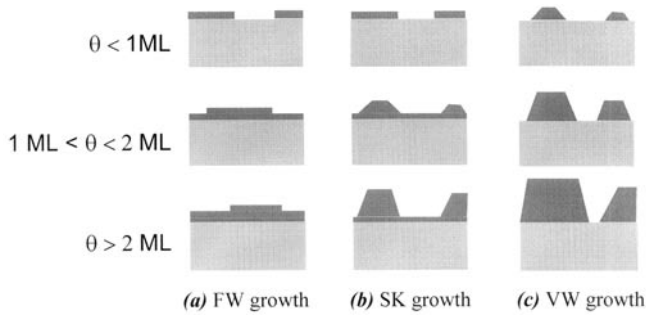


**Figure 6.** A schematic illustration of various thin-film growth modes ($\theta$ represents the total adsorbate coverage). (a) Frank–van der Merwe (FM) growth—strict layer-by-layer epitaxial growth; (b) Stranski–Krastanov (SK) growth—growth occurs in a layer-by-layer (i.e. 2D) fashion up to a certain critical thickness (which is generally related to the lattice mismatch between the adsorbate and substrate materials) and then switches to a 3D, i.e. islanding growth mode; (c) Vollmer–Weber (VW) growth—this occurs when the adsorbate and substrate surface (and interface) free energies are such that it is thermodynamically favourable for the overlayer to form islands from the onset of growth.

the fabrication of the self-assembled nanoclusters shown in figure 7. The lattice mismatch that exists between the substrate and adsorbate lattices (for the InAs/GaAs system—the most studied—the mismatch is ∼7%, for the Si/Ge system, ∼4%, and for InP/GaAs, ∼3.8%) drives, at a certain overlayer critical thickness, a transition from 2D (layer-by-layer) to 3D (island) growth.

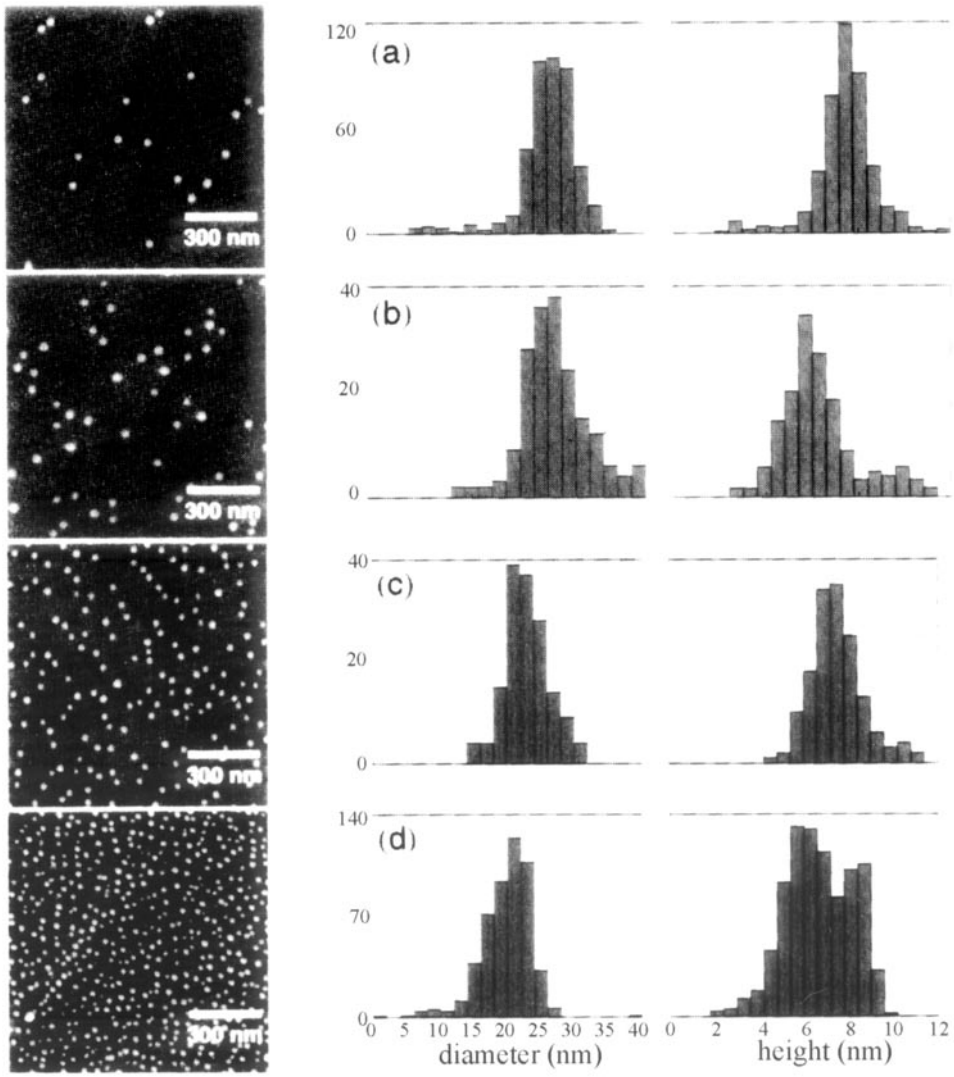


**Figure 7.** AFM images and corresponding histograms of diameter and height for self-assembled (Stranski–Krastanov growth mode) InAs nanocrystals on GaAs. Each AFM image is 1 $\mu$m$^2$ and the InAs coverage is ∼1.6, 1.65, 1.75 and 1.9 ML in (a), (b), (c) and (d) respectively (Leonard *et al* 1994).

Nanocluster diameters for the In(Ga)As/GaAs(100) system are typically of the order of 20 nm with remarkably narrow height and diameter distributions (typical values are ±10% and ±7% respectively (Leonard *et al* 1994)). Limited control over nanocluster size, density and shape is possible through variation of growth parameters or the choice of substrate orientation.

Progress towards controlling the lateral positions of the clusters has been reported by Mui *et al* (1995) who used a corrugated GaAs substrate (patterned using optical lithography and etching) to align InAs clusters into linear 'strings' (figure 8(a)). This work, as discussed by Ngo *et al* (1996), exploits the faster surface diffusion on the facets (of 311 type) shown in figure 8(a), to force an 'accumulation' of InAs in the trench (a narrow strip of GaAs(100)) and thus more quickly reach the critical thickness for a 2D–3D growth transition. Prior to this, Nötzel *et al* (1994a, b) had used high-index ($(n11)$B) GaAs substrates (figure 8(b)) to drive the alignment of AlGaAs nanoclusters, achieving the highest level of ordering on the GaAs(311)B substrate. Deng and Krishnamurthy (1998) have reported the formation of clusters of self-assembled SiGe islands on Si(100) via nucleation at the edges of SiC-induced pits. Very recently, Jin *et al* (2000) have reported the controlled positioning of self-assembled Ge nanocrystals using selectively grown Si mesas (figure 8(c)).

In the InAs/GaAs system, choice of substrate orientation can not only modify cluster distributions as shown by Nötzel, but also strongly modify cluster shapes. Figures 9(a) and 9(b) illustrate the distinct differences in quantum dot shape observed for growth of InAs on GaAs(100) and GaAs(311)A (Henini *et al* 1998). Clear faceting has been observed for InP clusters on GaAs with the quantum dots imaged (using both TEM and AFM) as truncated pyramids (Georgsson *et al* 1995) (figure 9(c)). Similarly, for the Ge/Si system, extremely well-defined {105} facets have been observed for self-assembled Ge nanocrystals (Mo *et al* 1990, Knall and Pethica 1992, Kästner and Voigtländer 1999) (figure 9(d)). Recent STM work (Medeiros-Ribeiro *et al* 1999) has shown that the bimodal size distribution observed for the growth of Ge nanocrystals on Si(100) under particular growth conditions actually arises from the presence of two differently *shaped* islands.

The relative importance of kinetics and thermodynamics in determining the morphology of self-assembled quantum dot samples has been the subject of some debate. Electron diffraction studies provided strong evidence for faceting of InAs clusters on GaAs(001) during growth at 530 °C. Faceting was not present for lower-temperature growth (Grundmann *et al* 1994). Extensive Ostwald ripening (the growth of larger particles at the expense of smaller particles which have higher surface free energies and are thus inherently less stable) has been observed for both II–VI clusters on II–VI substrates (CdSe on ZnSe) (Xin *et al* 1996) and Ge clusters on Si(001) (Ross *et al* 1998).

That factors other than lattice mismatch play a large role in the production of self-assembled nanocrystals in the InAs/GaAs system is perhaps most strikingly illustrated by the lack of quantum dot formation when the substrate orientation is of {111} type (Yamaguchi *et al* 1996). However, Yamaguchi *et al* suggested that kinetic effects were '*at most second order*' and that it was the stage at which strain relaxation occurred that determined the growth mode. Both Xie *et al* (1996) and Shchukin *et al* (1995) have stressed the importance of strain fields in the mechanism underlying size equalization of self-assembled nanoclusters, with Shchukin *et al* presenting a detailed theoretical discussion of the various factors that contribute to the change in energy of the system due to the formation of a single nanocluster. They considered not only the free energies of the cluster facets but both the cluster edge energy and the strain energy due to elastic relaxation. The elastic relaxation energy comprises two parts: one arising from the lattice mismatch and another from the surface stress tensor at the cluster edges. Both of these contribute to the *strain field* associated with a cluster and for a dense cluster system, elastic interaction between clusters cannot be avoided. However, Ross *et al* (1998) have recently argued that a critical dependence of chemical potential on cluster shape is sufficient to drive the cluster size distribution narrowing observed for both III–V and group IV systems.

Xie *et al* (1995) exploited interacting strain fields in the synthesis of *vertically* self-organized InAs nanoclusters on GaAs. Figure 10(a) illustrates the striking correlation between

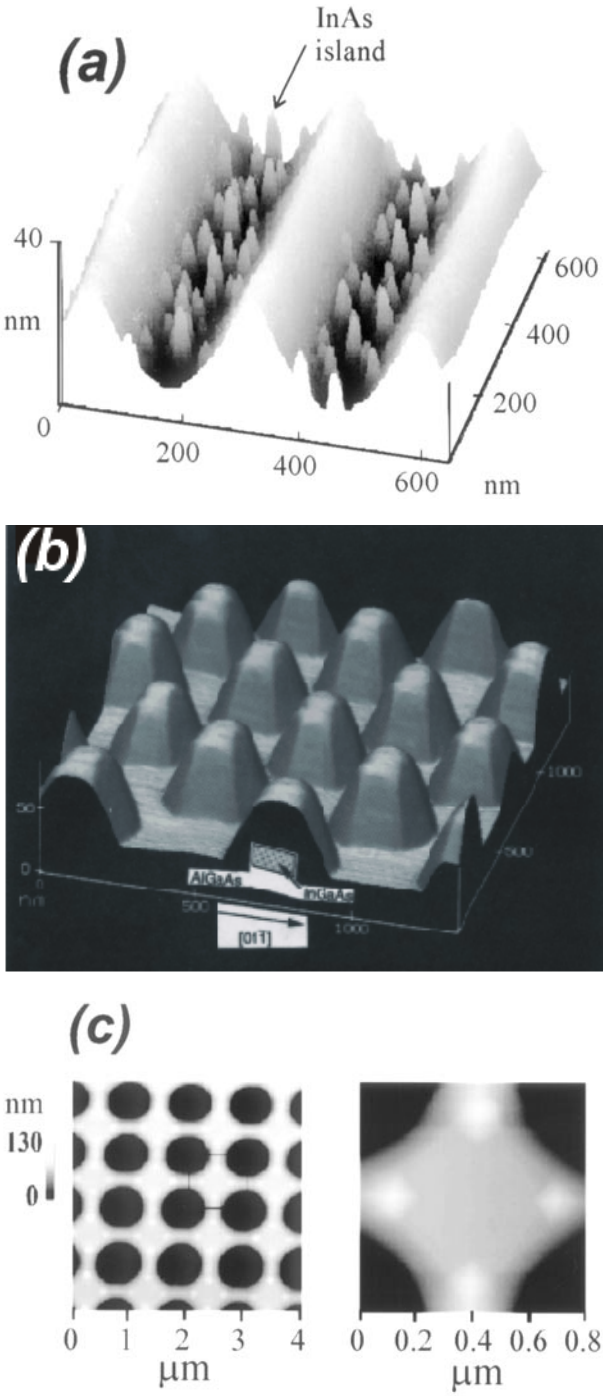


**Figure 8.** Methods used to control lateral positions of SK-grown clusters: (a) a (lithographically) corrugated GaAs substrate constrains InAs islands to a narrow channel (Mui *et al* 1995); (b) growth on a high-index substrate (in this case GaAs(311)B) leads to alignment of InGaAs nanocrystals (Nötzel *et al* 1994a); (c) controlled positioning of Ge islands using selectively grown Si mesas (Jin *et al* 2000).

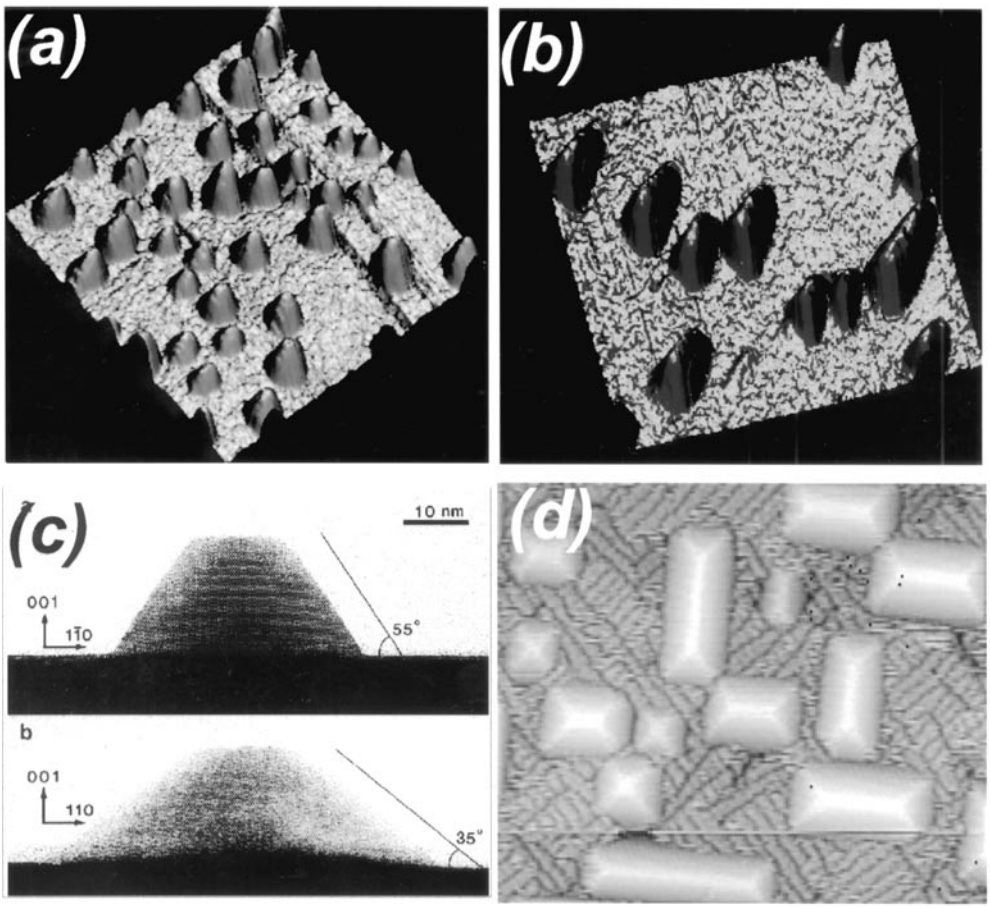


**Figure 9.** Controlling the shape of SK-grown nanocrystals. (a) InAs clusters on GaAs(100) show little evidence for facet formation in STM images. However, on GaAs(311)B, (b), the clusters are clearly faceted, forming arrow features which all point in the [2$\bar{3}$3] direction (Henini *et al* 1998). Similar distinct faceting is observed for (c) InP (Georgsson *et al* 1995) and (d) Ge clusters (Kästner and Voigtländer 1999).

the positions of the islands across five spacer layers of 36 monolayer (ML) thickness. Xie *et al* explained their results in terms of the interplay between diffusing In adatoms and the strain fields in the GaAs substrate arising from the presence of an InAs dot (figure 10(b)). As expected from this model, increasing the spacer layer thickness (above ∼100 ML) leads to a loss of correlation in the cluster positions, i.e. the vertical stacking is removed.

Vollmer–Weber (VW) growth occurs when the free energies of the substrate surface and the adsorbate layer are such that the adsorbate prefers not to wet the substrate but instead forms 3D islands from the onset of growth (figure 6(c)). VW growth has also been widely exploited to fabricate nanoscale clusters. As this growth mode requires a low free energy/chemically inert surface, common substrates include amorphous carbon, graphite, hydrogen-passivated Si and metal oxides. Ganz *et al* (1988, 1989) studied the interaction of a range of metals (Cu, Ag, Au and Al) with graphite, observing the formation of dimers and clusters of three or more metal atoms. As for the pre-formed clusters discussed above, cluster diffusion readily occurs. Other groups have extended the study of cluster–graphite interactions to different metals, e.g. Co,

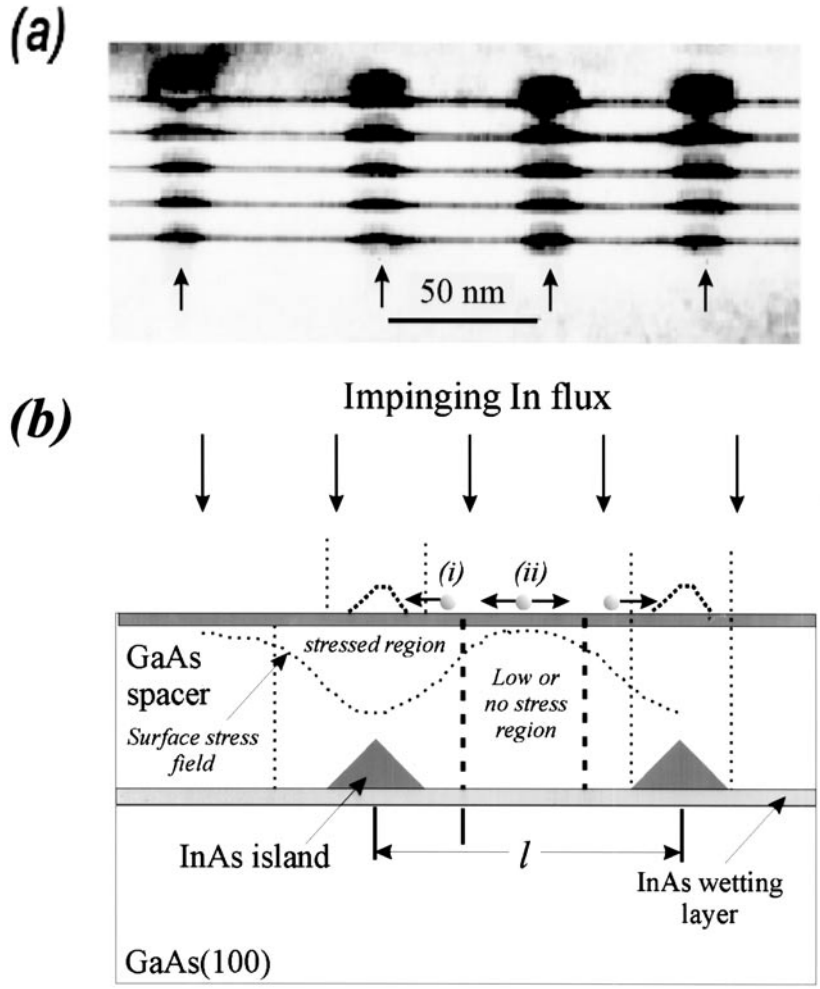


**Figure 10.** (a) Five sets of InAs islands separated by GaAs spacer layers 36 ML thick. Note the clear vertical stacking of the dots. (b) A schematic diagram illustrating the processes responsible for stacking of the islands, namely: (i) diffusion of In under a mechanochemical potential arising from the stress field surrounding an island and (ii) isotropic migration of atoms which contributes to the formation of new islands (Xie *et al* 1995).

Mo (Xu and Ng 1995, 1997), Pd (Piednoir *et al* 1997) and Pt (Clark and Kesmodel 1993), in each case observing cluster formation. A particular focus of metal–graphite interactions has been the perturbation of the electronic structure of the graphite surface that occurs in the vicinity of an adsorbed cluster (Mizes and Foster 1989, Xhie *et al* 1991, Xu and Ng 1997). Cluster-induced electron standing waves whose period matches the graphite Fermi wavevector are observed and it has been suggested that this electronic rearrangement of the surface might be exploited to control cluster positions (Binns *et al* 1999).

Si(100)(2 × 1) (Boland 1992) surfaces terminated with H under UHV conditions exhibit a small number of dangling-bond defects whose density can be tuned via the H-passivation treatment parameters. Alternatively, the large electric fields/current densities possible with the STM can be used to selectively desorb hydrogen to form nanometre-scale—or, under

appropriate conditions—atomic-scale features (Shen *et al* 1995). Importantly, these features (figure 11(a)) comprise 1D or 2D arrays of Si dangling bonds. Atomic and molecular species deposited on the H:Si(100) surface will diffuse across the passivated regions, preferentially adsorbing at either natural or STM-generated dangling-bond defects. Thus, the depassivated regions act as adsorption templates and, as discussed by Hersam *et al* (2000), may be used to create molecular arrays on a Si surface. Figures 11(b) and 11(c) show, respectively, how dangling-bond sites act as nucleation centres for the growth of nanoscale Ag (Butcher *et al* 2000) and norbornadiene (Abeln *et al* 1997) islands). (See also Palasantzas *et al* (1999) for a discussion of Co nanocluster growth on H:Si(100).) Lopinski *et al* (2000) have recently synthesized 1D molecular wires (styrene lines) using STM-patterned rows of dangling bonds on H:Si(100) (figures 11(d) and 11(e)).

Alternative methods of Si surface passivation have been employed to create inert substrates for the VW growth of nanoscale clusters. Adsorption of Sb—a popular surfactant in the growth of Ge on Si (Copel *et al* 1990, Gay and Srivastava 1999)—on Si(111) with the subsequent adsorption of Ag (Park *et al* 1998) produces nanoscale Ag islands. Both Au (Ruan and Chen 1997) and Ag (Dunn *et al* 1997, Wang *et al* 2000, Taylor *et al* 2000b) have been deposited onto a monolayer of $C_{60}$ on Si(111). Photoemission measurements for the latter system (Taylor *et al* 2000b) indicate that the $C_{60}$ monolayer 'decouples' the clusters from the Si substrate to the extent that distinct cluster-charging-related shifts in the energies of the Ag valence band and core-level photoemission features are observed. Researchers in Weaver's group in the University of Minnesota have recently reported a novel method of forming nanocrystals on Si(111)$(7 \times 7)$ which involves the use of buffer layers of Xe (Huang *et al* 1998, Chey *et al* 1999). Exposure of the Xe buffer layer to a flux of Ag atoms leads to the formation of silver nanocrystals that are 'delivered' to the $(7 \times 7)$ surface on desorption of the Xe buffer layer (figure 12). As highlighted by the authors, this procedure not only circumvents the thermodynamic criteria usually required for VW growth but, through variation of the buffer layer thickness and the concomitant cluster coalescence that occurs during Xe desorption, allows control of the cluster size distribution.

A novel method of controlling the lateral positions of nanoparticles has recently been used to form ordered arrays of 5 nm metal (Ti) nanoclusters (Winningham *et al* 1998). A protein crystal etch mask combined with low-energy electron-enhanced etching led to the transfer of a hexagonal array of 18 nm diameter holes. Preferential nucleation and growth of Ti islands in the holes produced a lattice of nanoclusters.

The principal motivation for the study of metal particles on metal oxide substrates relates to their use in heterogeneous catalysis. Bäumer and Freund (1999) have recently reviewed work in this field, concentrating on growth of a range of metals (Ag, Rh, V, Pd, Co, Pt) on metal-supported thin alumina films. As for cluster nucleation on H:Si(100), the metal particles nucleate at defects in the substrate. Plots of Rh cluster density, island diameter, atoms per particle and cluster aspect ratio each as a function of nominal Rh film thickness are shown in figure 13(a), with a representative STM image shown in figure 13(b). Bäumer and Freund discuss in some detail the electronic properties of these (and other metallic) clusters on $Al_2O_3$, as determined by photoelectron spectroscopy and Auger measurements (Freund 1997). They focus on the role of electron tunnelling from the metal substrate through the oxide film and, in particular, the timescale over which this occurs. The question of charge transfer between nanoclusters and substrates/electrodes will be returned to in section 4 below.

The final example of Vollmer–Weber growth we shall discuss is a fascinating example of the application of the growth mode to the synthesis of nanoscale magnetic particles (see section 6). The Au(111) surface forms a strain-relief-driven $(22 \times \sqrt{3})$ reconstruction which takes the form of a 'herring-bone' pattern. Deposition of submonolayer coverages of Co

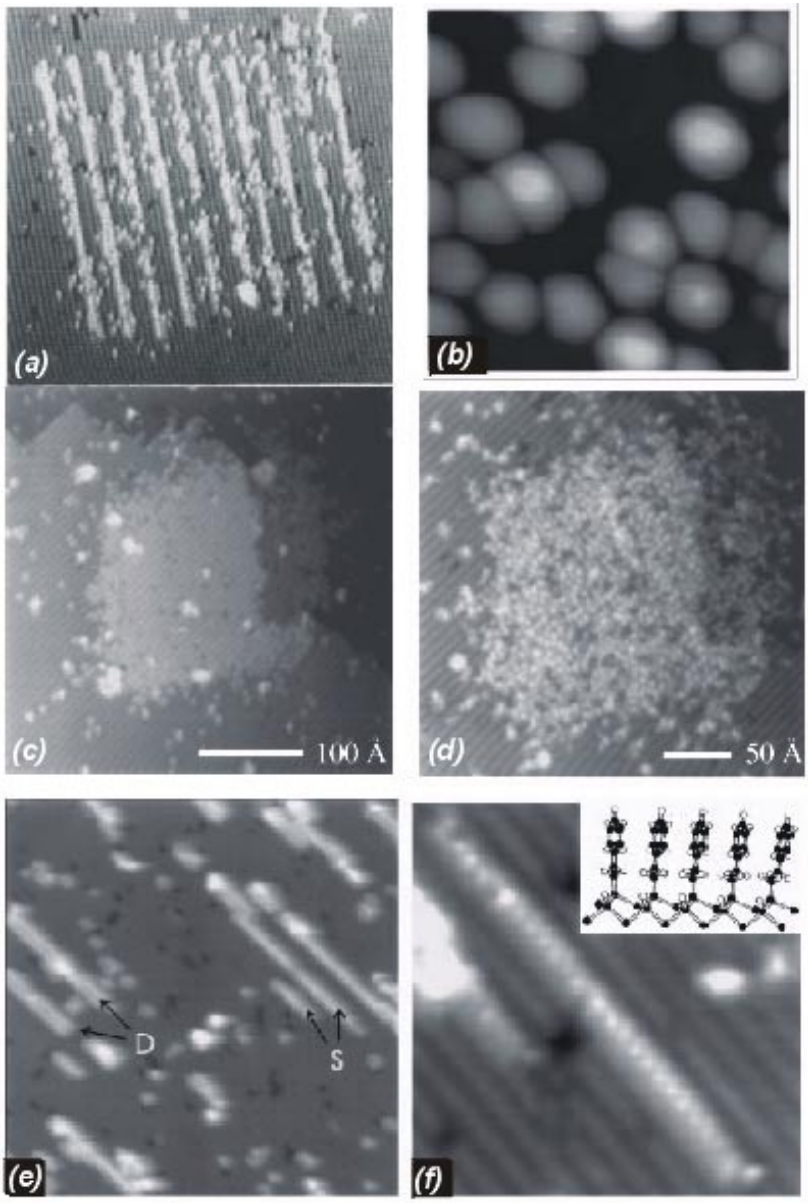


**Figure 11.** Hydrogen-passivated Si(100) as a template for cluster growth and molecular adsorption. (a) Using an STM tip it is possible to selectively desorb hydrogen and thus fabricate atomic-scale features consisting of 'chains' of Si dangling bonds (Shen *et al* 1995). (b) Ag clusters grown on H:Si(100) where naturally occurring defects in the passivation layer act as nucleation sites (Butcher *et al* 2000). (c), (d) Templating 2D molecular adsorption: following the STM-induced depassivation of a ∼10 nm × 10 nm region of H:Si(100), norbornadiene molecules preferentially adsorb in the depassivated area (Abeln *et al* 1997). (e), (f ) Templating 1D molecular adsorption: preferential adsorption of styrene molecules on lines of (STM-generated) single dangling-bond defects; in (e), S and D indicate single and double lines of styrene molecules. (f ) A high-resolution image of a single styrene line with the inset showing a possible conformation associated with the styrene chain—the parallel alignment of the phenyl groups is expected to lead to electronic orbital overlap (Lopinski *et al* 2000).

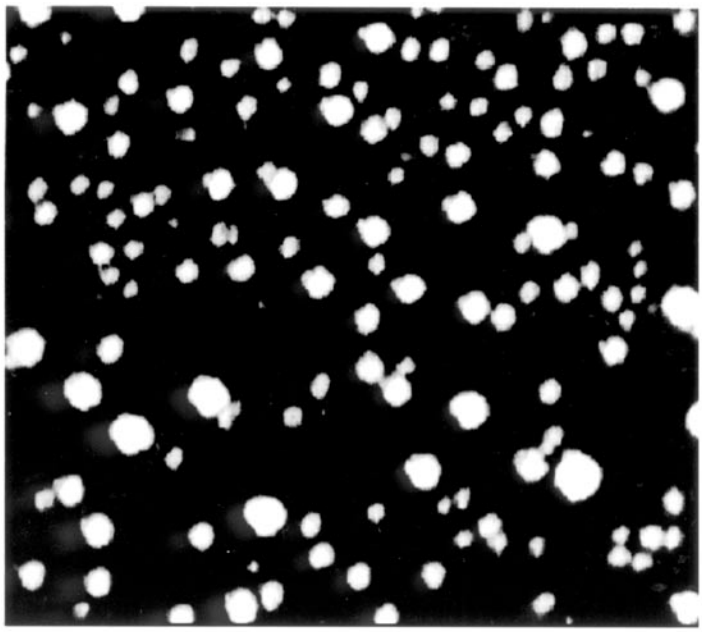

**Figure 12.** Ag clusters formed on Si(111)(7 × 7) via deposition of 0.2 Ag on a Xe buffer layer at 50 K followed by desorption of the Xe. STM image size: 100 × 100 nm$^2$.

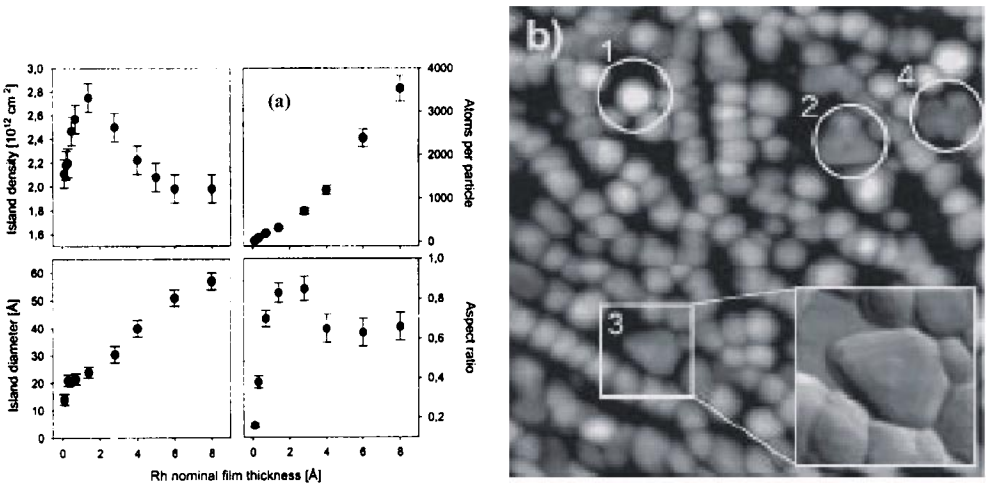


**Figure 13.** (a) Cluster density, average diameter, aspect ratio and atoms per cluster versus Rh deposition on an $Al_2O_3$/NiAl(110) substrate. (b) An STM image of a surface following 0.6 nm Rh deposition. The numbers in the image represent the following: (1) disordered aggregate, (2), (3) Rh(111) crystallites and (4) a particle formed by coalescence (Bäumer and Freund 1999).

on Au(111)(22 × $\sqrt{3}$) produces an array of two-layer-high Co islands each consisting of approximately 1700 atoms (Voigtländer *et al* 1991, Tölkes *et al* 1997). The islands are nucleated at the 'elbows' of the herring-bone reconstruction. Thus, the Au(111) substrate not only promotes Co island formation, but also acts as a template for the lateral positions of the islands.

### *3.3. Colloidal synthesis of nanoclusters*

The colloidal synthesis of monodisperse particles has its origins in Faraday's nineteenth century research on Au colloids (Faraday 1857) and involves the controlled nucleation and growth of clusters in a precursor-containing solution. Metal and semiconductor colloid syntheses follow rather different routes and are thus described separately in the following sections.

*3.3.1. Au and Ag colloids.* Au colloids have, to date, been the focus of the majority of research on metal colloid-based nanostructures and nanostructured materials. Although macromolecular Au complexes surrounded by shells of stabilizing organic ligands have been produced, notably the $Au_{55}(P(C_6H_5)_3)_{12}Cl_6$ system synthesized by Schmid *et al* (1981), a more widely used method of Au colloid synthesis involves the reduction of a metal salt in a ligand-containing aqueous solution. A typical combination of reagents is hydrogen tetrachloroaurate and sodium citrate (Frens 1973, Grabar *et al* 1995, Mirkin 2000). By adjusting the stoichiometric ratio of these compounds, the size of the Au nanoparticles can be controlled. As discussed by Mirkin (2000), the charge state of the Au particles is thought to be $Au^0$ at the core with a chloride- and citrate-coordinated $Au^I$ shell, resulting in net anionically charged colloids.

However, as pointed out by Andres *et al* (1996b), it is somewhat difficult to fabricate close-packed, ordered structures or materials from charge-stabilized nanoparticles. Brust *et al* (1994) developed a two-phase approach to the synthesis of *thiol-derivatized* Au nanoparticles. They combined techniques based on the self-assembly of monolayers of alkane thiols on Au surfaces (see section 3.3.1) with the reduction of $AuCl_4^-$ by sodium borohydride to produce solutions of 1–3 nm Au particles bearing a stabilizing surface thiol coating. On the basis of XPS results—in particular, the absence of a Au 4f chemically shifted component at a binding energy of 84.9 eV—Brust *et al* (1994) argued that the majority of the atoms in the thiol-stabilized Au clusters were present as $Au^0$.

Whetten *et al* (1996) have shown that the clusters synthesized by the method of Brust *et al* are equivalent to Au clusters produced in the gas phase and subsequently passivated by contact with a mist of organic solvent containing 1-dodecanethiol. Size-selected stabilized Au particles were subsequently crystallized into both 2D and 3D superlattices. As Andres *et al* (1996b) argue, while the Brust *et al* technique has the significant advantage of simplicity, growth of clusters in the gas phase with *subsequent* passivation permits greater control of cluster size and composition and, importantly, enables the clusters to be thermally annealed. Figure 14(a) is a bright-field transmission electron microscope (TEM) image of a well-ordered monolayer of 3.7 nm thiol-stabilized Au clusters on $MoS_2$. The average centre-to-centre distance of the clusters is 5.0 nm. The 1.3 nm difference between the cluster size and the intercluster distance is shorter than twice the thickness of a monomolecular film of dodecanethiol ($2 \times 1.2$ nm), strongly suggesting interpenetration of the thiol chains.

Kiely *et al* (1998) have shown that thiol-stabilized Au particles with a *polydisperse* size distribution (prepared using the Brust *et al* method) also show a remarkable tendency to spontaneously crystallize into ordered structures. Figure 14(b) illustrates one type of ordering that is observed: different-sized Au particles forming a bimodal array. In this case the particles have sizes of $4.5 \pm 0.8$ nm and $7.8 \pm 0.9$ nm and form 'rafts' of bimodal ordering that extend up to 1 $\mu m^2$ in area. As the authors note, in previous studies of 2D ordering of polydisperse nanoclusters only a radial distribution of particle sizes was observed (Ohara *et al* 1995). In addition to bimodal ordering of clusters, Kiely *et al* report both the formation of ordered size-segregated particle superlattices and the observation of random alloys. They explain the observation of variously ordered particle superlattices in terms of entropy-driven

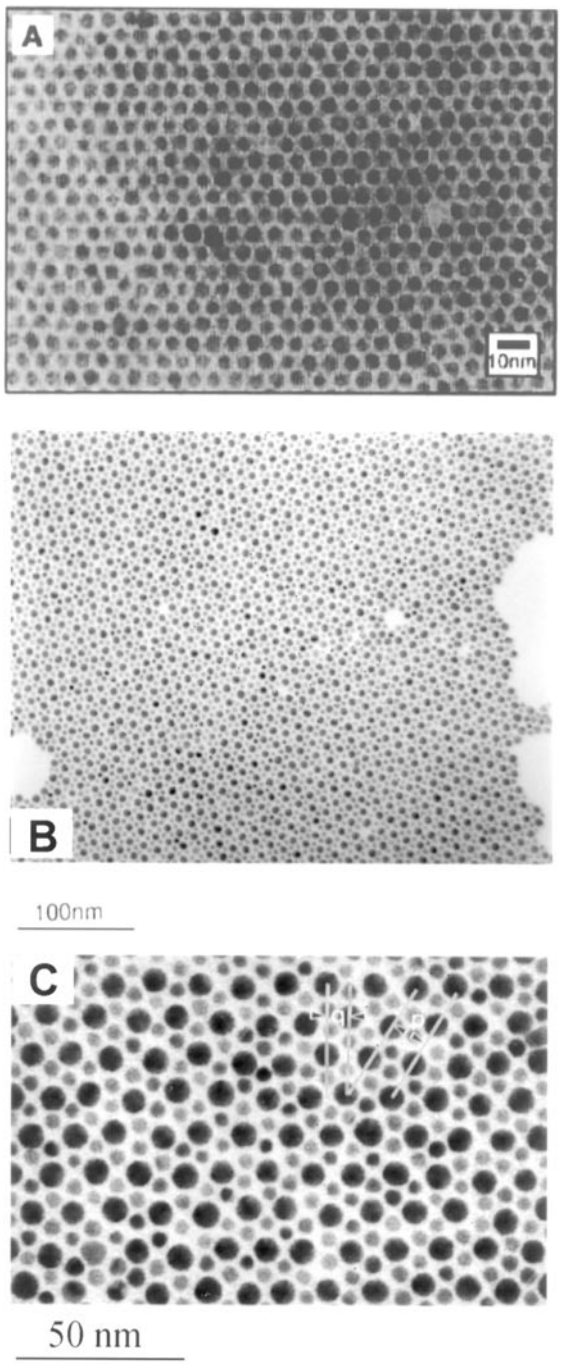


**Figure 14.** (a) A superlattice of size-selected thiol-passivated 3.7 nm Au clusters on a $MoS_2$ substrate (imaged by TEM) (Andres *et al* 1996b). (b) Crystallization of *polydisperse* thiol-capped Au clusters into bimodal arrays on amorphous carbon-coated TEM grids. The higher-magnification TEM image shown in (c) shows in more detail the packing associated with the bimodal size distribution (∼4.5 and 7.8 nm diameter) of the clusters (Kiely *et al* 1998).

crystallization, previously described by Eldridge *et al* (1993). Prior to the work of Kiely *et al*, a comprehensive study of the roles that particle size, size distribution, temperature and ligand type play in the self-organization of passivated Au and Ag nanocrystals in Langmuir–Blodgett films identified the interpenetration of ligand shells as a key factor in determining the morphology of 2D films (Heath *et al* 1997).

Very recently, Kiely *et al* (2000) have extended the study of colloidal alloys to systems where the alloy arises not from the mixture of differently sized particles but from the mixture of particles of different chemical elements. Figure 15 is a bright-field TEM image of an ordered Au/Ag colloidal nanoalloy prepared, via slow evaporation onto a carbon-coated TEM grid, from a 10:1 mixture of thiol-capped Au and Ag particles. Energy-dispersive x-ray (EDX) analysis using a 0.7 nm diameter electron probe was used to spatially probe the chemical composition of the lattice. The results are also shown in figure 16 where it is clear that the particles with less contrast in the TEM image arise from the Ag particles. As expected, the S EDX signal across the lattice is roughly constant (the two particles are capped with thiol molecules with identical chain lengths).

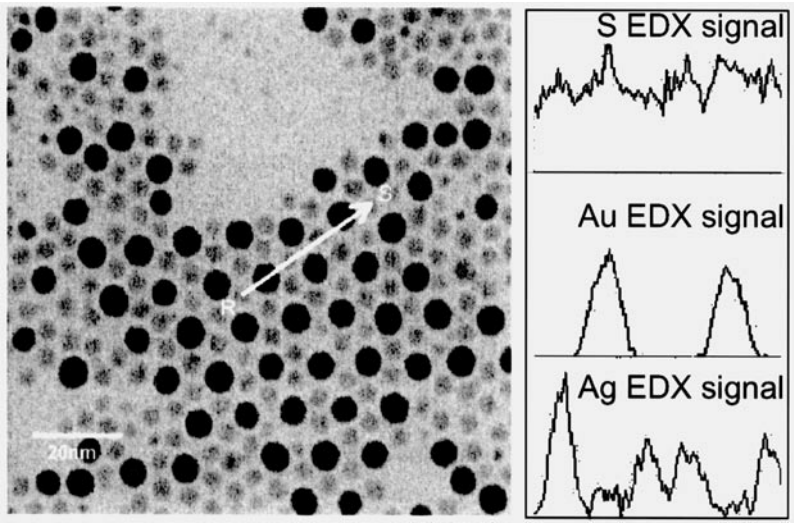


**Figure 15.** A bright-field TEM image of a nanoalloy consisting of a mixture of thiol passivated Au and Ag nanocrystals. From the energy-dispersed x-ray spectra shown to the left (which were acquired along the line RS in the TEM image) it is clear that the darker features in the TEM image arise from the Au clusters (Kiely *et al* 2000).

Andres *et al* note that thiol-stabilized Au colloidal particles that have been transferred to chemically inert substrates via slow evaporation from a solvent are destroyed by scanning electron microscopy (SEM) imaging and may also be readily removed by immersion in solvents. This very weak cluster–surface interaction makes scanning probe microscopy (SPM) studies of passivated colloids adsorbed on inert surfaces problematic as the tip readily moves clusters across the surface. Passivated clusters, despite their mass (which may be as large as some tens of thousands of atomic mass units) exhibit very high surface mobilities (Bigioni *et al* 1999, Luedtke and Landman 1996). For example, room temperature studies of passivated Au nanoclusters on graphite have demonstrated that *individual* clusters may be imaged only at step edges (and then only at very low tunnelling currents) (Terrill *et al* 1995). Although imaging in liquids (Klein *et al* 1996a) or non-contact-mode atomic force microscopy (Taylor

*et al* 2000a) can be used to reduce tip–cluster interactions, in recent work on passivated Au and semiconductor (CdSe, GaAs) colloids on $SiO_2$, H-passivated (Higashi *et al* 1991, Burrows *et al* 1988) Si(111) and Si treated with (3-mercaptopropyl) trimethoxysilane (MPS) (Katari *et al* 1994), we have found that even the weak interactions involved in NC-AFM are sufficient to displace clusters (Taylor *et al* 2000a).

*3.3.2. Controlling cluster–surface and cluster–cluster interactions.* A number of groups have explored methods of tethering clusters to surfaces. Andres *et al* (1996a) and Dorogi *et al* (1995) have used dithiol molecules (specifically xylyldithiol and biphenyldithiol) which have a sulphur-containing group on each end of the organic chain: one end bonds to a Au(111) substrate whereas the other is chemically bound to a bare Au cluster. The xylyldithiol in particular enabled both stable STM and scanning tunnelling spectroscopy measurements to be carried out. As demonstrated by Harrell *et al* (1999) it is possible to substitute dithiol molecules into the organic shell of *passivated* Au clusters enabling strong bonding to a bare Au(111) surface. Isolated clusters were imaged (albeit only at very low ($\ll$1 nA) tunnel currents) (see figure 16(a)) and spectroscopically probed although there was some evidence for tip-induced cluster movement. Gurevich *et al* (2000) used a cysteamine ($C_2H_7NS$) self-assembled monolayer on a Pt film to bind 20 nm Au clusters to a $Si/SiO_2$ substrate.

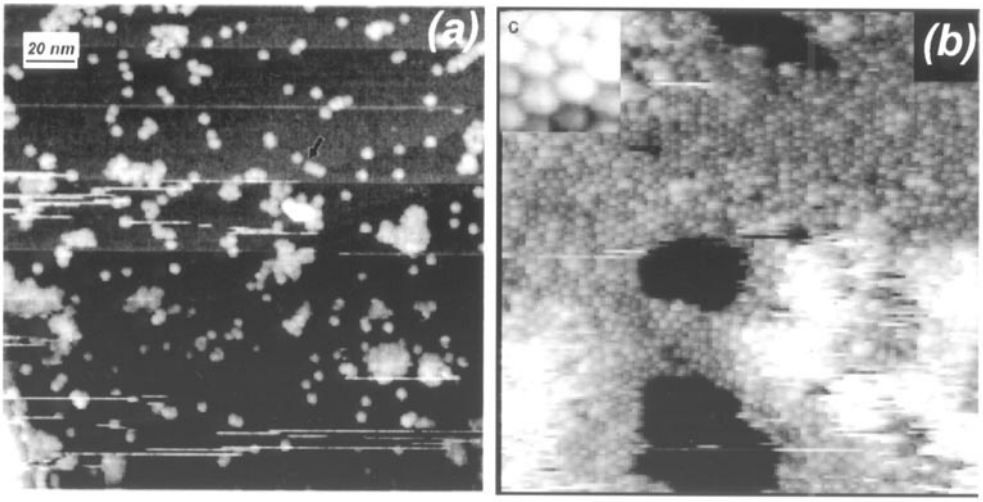


**Figure 16.** STM images of thiol-capped Au clusters on (a) Au(111) (Harrell *et al* 1999) and (b) graphite (Durston *et al* 1997). Note that the clusters imaged in (a) are bound to the bare Au surface via dithiol molecules (thiol molecules with S atoms at both ends of the chain). These provide a relatively strong interaction between cluster and substrate and permit the imaging of isolated clusters (at low tunnelling currents). The clusters shown in (b) (and in the high-resolution image shown in the inset (c)) are relatively weakly bound to the graphite substrate and the layer is easily disrupted by high-tunnel-current STM scans.

However, stable STM imaging and spectroscopy of passivated Au and Ag colloidal nanoclusters on graphite and Au(111) surfaces *without* the use of an intermediate 'tethering' molecular layer has also been reported (Durston *et al* 1997, Harrell *et al* 1999, Petit *et al* 1998, Silly *et al* 2000). Figure 16(b) is an STM image of $\sim$1 ML of thiol-passivated Au clusters on graphite where a well-ordered superlattice is observed at a tip–sample bias voltage of $\sim$1.5 V with a tunnel current of 80 pA (Durston *et al* 1997). At smaller bias voltages the authors argue that due to single-electron effects (see section 4) the clusters are not imaged;

however, no scanning tunnelling spectroscopy data were reported. Pileni's group at CNRS, Paris, have reported that a critical parameter in preparing self-assembled superlattices of Au and Ag clusters is the particle concentration in the solvent (Taleb *et al* 1997, 2000). At low particle concentration, 2D superlattices (involving hexagonal packing of the clusters) are observed, whereas at higher concentrations, 3D fcc lattices are observed. This group have also reported the acquisition of stable tunnelling spectra from isolated passivated Ag and Co nanoclusters on clean and thiol-terminated Au(111) respectively (Taleb *et al* 2000, Petit *et al* 1999a) and have recently succeeded in acquiring photon emission STM maps from ordered layers of passivated Ag clusters on Au(111) (Silly *et al* 2000)—see section 5.4: *Single-cluster luminescence* below.

An alternative method of forming robust cluster layers is to covalently link the clusters to each other. Cluster–cluster linkage not only improves the stability of the cluster layer but also enables controlled electronic coupling of the clusters. Andres *et al* (1996b) used aryl dithiols as the linker molecules in what they have termed a *linked cluster network* (LCN). Brust *et al* (1995) similarly used dithiols to link Au clusters into a *3D* network where interparticle separation was controllable to ångström precision via the use of different dithiol linker molecules. The electronic properties of these systems—and related cluster networks—will be discussed in section 4.

*3.3.3. Biomolecule–cluster hybrids.* A recent innovative advance in nanocluster science that has generated considerable excitement—to the extent where it has been vaunted as constituting 'a new frontier in science' (Mirkin 2000)—is the exploitation of DNA as a *selective* linkage unit for linkage between clusters. The basis of this technique, which was originally reported in 1996 by Mirkin *et al* (1996) and Alivisatos *et al* (1996), involves applying the biochemical molecular recognition processes that underlie base pairing in DNA strands to the control of cluster aggregation.

Figure 17(a) is taken from Mirkin's recent review (Mirkin 2000) and illustrates the original strategy that was reported (Mirkin *et al* 1996). Two batches of Au nanoparticles (an important point to note is that these are *charge*-stabilized and not thiol-stabilized particles) were functionalized with non-complementary eight-base-pair DNA strands (via alkanethiol groups on the ends of the DNA strands). When the two batches of Au particles were mixed there was no DNA recognition and hence no particle aggregation. However, the addition of linker DNA strands containing eight-base-pair sticky ends that were complementary to the base pairs attached to the Au particles promoted particle aggregation. Mirkin *et al* (1996) successfully synthesized both 2D and 3D hybrid Au particle–DNA aggregates as shown in figures 17(b) and 17(c).

In the space of only a few years the burgeoning research area of biomolecule–inorganic cluster hybrid systems has rapidly expanded, to now include nanocrystal assembly based on protein binding (Connolly and Fitzmaurice 1999), semiconductor nanocluster–DNA hybrids (specifically CdSe/ZnS particles, Mitchell *et al* 1999) and the use of semiconductor nanocrystals as fluorescent biological labels (i.e. as replacements for organic dyes—Bruchez *et al* 1998, Chan and Nie 1998). The optical properties of these latter systems will be discussed in section 4.2 below.

*3.3.4. Transition metal colloids.* VW-synthesized and pre-formed transition metal cluster films were discussed in section 3.2 and a brief outline of the current key issues in nanoscale magnetism is presented in section 6 below. Two groups have recently made significant advances in the synthesis of monodisperse transition metal colloids: Pileni's group in CNRS, Paris, and a

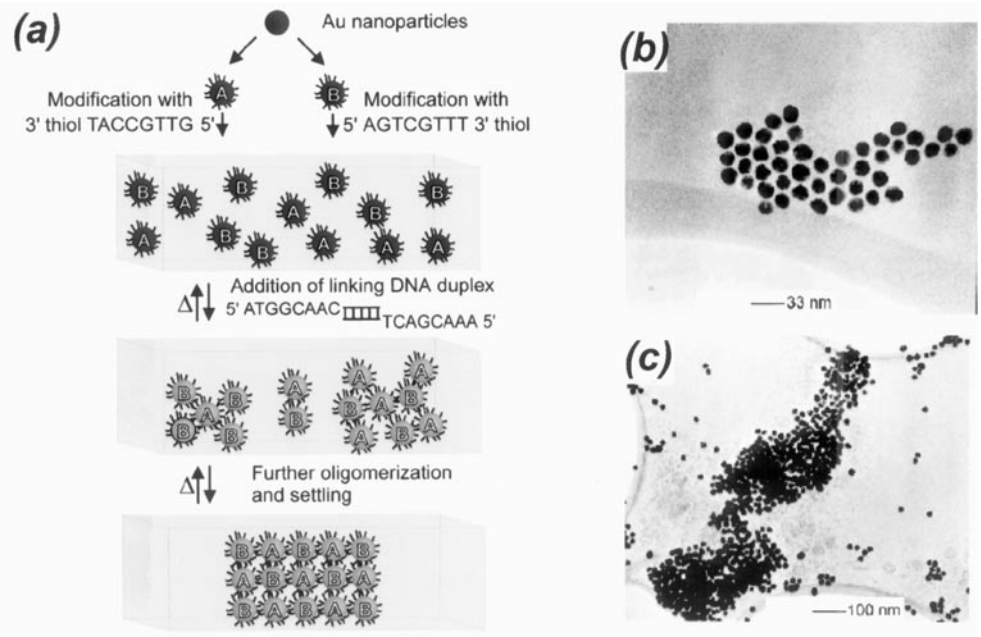


**Figure 17.** A DNA-based method for assembling nanocrystal aggregates. (a) A schematic diagram describing the steps used to form and organize DNA–Au cluster hybrids; (b), (c) TEM images of DNA–Au colloid hybrid material (Mirkin 2000, Mirkin *et al* 1996).

collaboration of IBM Almaden and IBM Yorktown Heights researchers. Petit *et al* (1998) used a reverse micelle approach to synthesize ∼6 nm diameter Co nanoparticles. (Reverse micelles are water droplets suspended in oil where the droplets are stabilized by a monomolecular surfactant layer.) The Co nanoparticles were subsequently coated with trioctylphosphine, dispersed in pyridine and then evaporated onto a TEM grid to produce the superlattices shown in figure 18. Petit *et al* (1999a) have also carried out STM and tunnelling spectroscopy measurements on Co nanoparticles adsorbed on dodecanethiol-terminated Au(111). Although no STM images of Co nanoparticle superlattices were reported, individual clusters were imaged at low tunnelling currents (80 pA) and single-cluster-derived tunnelling spectra exhibited distinct Coulomb-blockade-related (see section 4) features. Sun and Murray (1999) have synthesized both Co nanoparticle assemblies and size-tunable and highly monodisperse FePt nanoparticles which self-assemble into 3D superlattices (Sun *et al* 2000).

*3.3.5. Colloidally synthesized semiconductor clusters.* The commonest approach to the synthesis of both III–V and II–VI colloids involves the injection of reagents containing the cluster constituents (e.g. Cd and Se or Ga and As) into a hot solvent whose molecules cap and thereby stabilize the nucleated clusters. A wealth of recent work on CdSe nanocrystals has involved nanoclusters synthesized via a powerful synthesis technique pioneered by Murray *et al* (1993)[3]. This technique uses tri-*n*-octylphosphine oxide (TOPO) as the solvent, $Me_2Cd$ as the Cd-containing reagent and TOPSe as the Se-containing reagent. Injection of the reagents into a hot solution of TOPO results in the nucleation of clusters. The capping TOPO ligands

[3] Note that a number of groups (e.g. that of Alivisatos *et al* (Katari *et al* 1994) and that of O'Brien (Trindade *et al* 1997)) have used different precursors in II–VI nanocrystal synthesis. Due to constraints of space those precursors will not be discussed here.

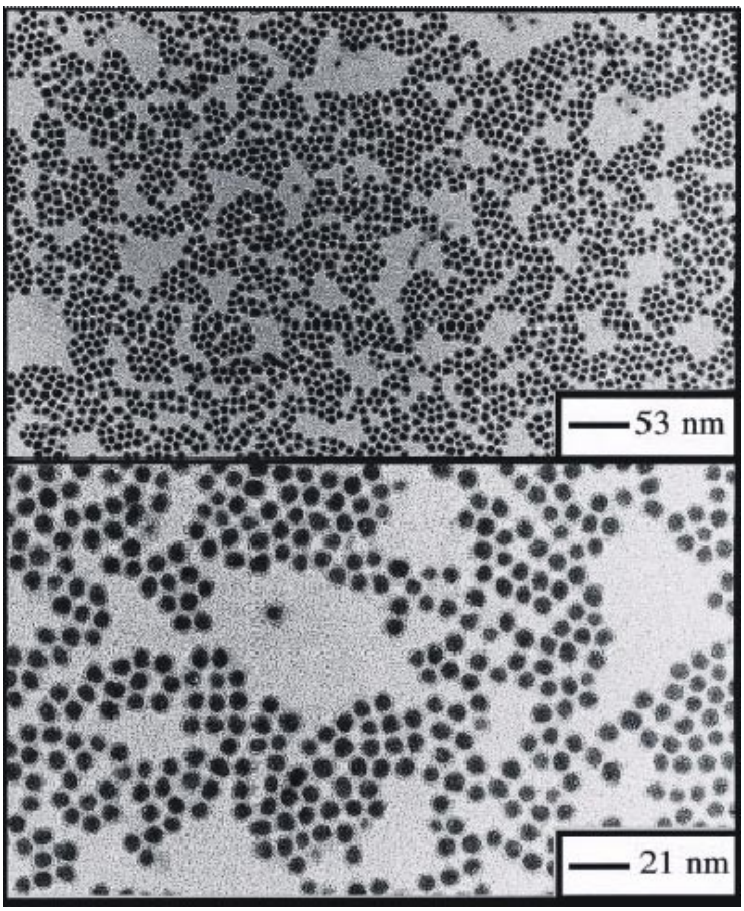


**Figure 18.** TEM images of Co nanocrystal superlattices (Petit *et al* 1999a).

significantly slow cluster growth, limiting the ability of Ostwald ripening to produce very large particles.

Careful control of solution temperature enables both the mean nanocrystal size and the nanocrystal size distribution to be tuned. Further improvement of the size distribution is achieved using size-selective precipitation (Murray *et al* 1993). This process exploits the size-dependent flocculation of the nanocrystals on addition of a non-solvent and can be used to narrow the size distribution of both metal and semiconductor nanocrystals to within a few per cent of the average diameter. Figure 19(a) is an optical micrograph of faceted crystals of 2 nm diameter CdSe nanoclusters whereas figure 19(b) is a TEM image of a 3D array of 4.8 nm diameter nanoclusters. Further to the discussion above of the importance of surface reconstruction for bulk semiconductors, recent x-ray absorption near-edge-structure (XANES) measurements of InAs and CdSe nanocrystals by Hamad *et al* (1999) suggest that a displacement of surface atoms, somewhat similar to that occurring at III–V(110) surfaces (see Duke (1996) and Srivastava (1997) for reviews of surface reconstruction/relaxation) occurs at III–V and II–VI nanocrystal surfaces.

As for the ordered metal nanoparticle systems described in the previous sections, the self-organized CdSe nanocrystal superlattice shown in figure 19(a) (Murray *et al* 1995) represents,

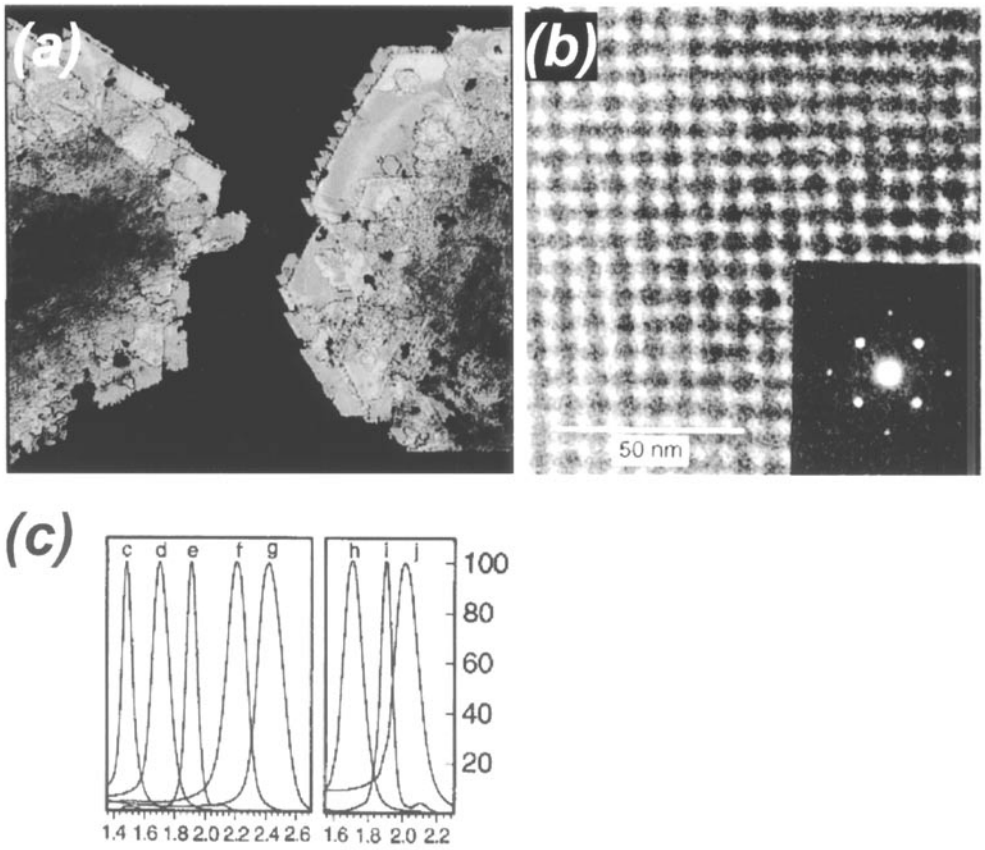


**Figure 19.** (a) A dark-field optical micrograph of a faceted colloidal superlattice comprising 2 nm diameter CdSe nanocrystals. (b) A high-resolution TEM image of a (101) projection of a colloidal fcc superlattice consisting of 4.8 nm nanocrystals. (c) X-ray diffraction data from CdSe superlattices. Each of peaks (c)–(g) is a (111) superlattice reflection for TOPO-capped dots of, respectively, 6.3, 5.4, 4.7, 3.9 and 3.5 nm diameter. Peaks (h)–( j) are the (111) superlattice reflections for 4.8 nm diameter nanocrystals capped with (h) hexadecyl phosphine, (i) trioctylphosphine oxide and ( j) tributyl phosphine oxide which yield intercrystal separations of 1.7, 1.1 and 0.7 nm respectively (Murray *et al* 1995).

on a number of levels, a model functional nanostructured material. The nanocrystals have sub-10 nm radii, are size-tunable (and, as most recently shown by Peng *et al* (2000), shape-tunable!), form ordered crystals and are passivated to ensure chemical inertness. The passivating ligands may also be used to control cluster–cluster spacings and thus modify intercluster electronic coupling. Figure 19(c) is again taken from the Murray *et al* (1995) pioneering work on CdSe superlattices and illustrates how different capping groups can be used to control intercluster spacing. Murray *et al* have also explored novel alternative methods to CdSe colloid deposition (other than condensation from a solvent) including the use of electrospray techniques (Danek *et al* 1994).

It should be stressed that prior to the Murray *et al* synthesis of II–VI nanoparticle superlattices, a number of groups had reported significant advances in the fabrication of semiconducting nanoparticles via colloidal chemistry although there remained problems with surface derivitization and size polydispersity (see Brus (1991) for a review). Mews *et al*

(1994) presented a notable example of II–VI nanoparticle 'engineering' in the preparation of a 'quantum dot–quantum well' system: a three-layered structure consisting of a CdS core coated by a layer of HgS which was in turn covered by an outer shell of CdS.

Colloidal synthesis of III–V nanocrystals has received somewhat less attention even though III–V semiconductors have larger excitonic diameters and should therefore exhibit more pronounced quantum size effects (see the following section). The smaller body of work related to III–V colloid synthesis is largely a consequence of the difficulties associated with their chemical preparation. Olshavsky *et al* (1990) reported the first synthesis of relatively monodisperse (although the size distribution was considerably larger than that observed for II–VI nanocrystals) GaAs nanocrystals. It was suggested, on the basis of XPS data, that carbon and nitrogen (possibly arising from the quinoline solvent in which the nanocrystals were dispersed) might act as capping moieties. Uchida *et al* (1991) proposed that quinoline-related molecular species (oligomers) present both in solution and at the surfaces of GaAs nanocrystals masked the optical absorption properties of the III–V colloids. They went on to propose (Uchida *et al* 1992) a modification of the synthesis procedure that eliminated the quinoline-related species.

TOPO-capped III–V—specifically InP—nanocrystals were originally synthesized by Micic *et al* (1994, 1996). Guzelian *et al* (1996) extended the TOPO-based techniques used in II–VI nanocrystal synthesis to the production of InAs quantum dots. As the authors noted, colloidal synthesis of InAs nanoclusters was of particular interest, given the large amount of work on MBE-grown self-assembled InAs dots. InAs nanocrystals with sizes which were tunable from 2.6 to 6.0 nm (with a $\pm 10\%$ to $\pm 15\%$ distribution) were synthesized and characterized by x-ray powder diffraction (among other techniques), demonstrating that the nanocrystals adopted the cubic zinc-blende structure of the bulk InAs lattice. Nozik and co-workers have recently synthesized (Micic *et al* 1998) close-packed arrays of InP nanocrystals. In addition, a novel route for more rapid synthesis of monodisperse InP nanocrystals has been proposed by Green and O'Brien (1998).

SPM imaging of assemblies of semiconductor colloids has, as for similar studies of adsorbed metal colloids, proved problematic. Ogawa *et al* (1995) found that continuous scanning of a particular area rapidly removed CdS nanoparticles due to very strong tip–colloid interactions. However, for CdS nanoparticles deposited on the same substrates as used in the work of Ogawa *et al* (namely, bare and thiol-terminated Au surfaces), Bakkers *et al* (1999) have found that, at least for tunnel currents $<1$ nA, the CdS nanoparticle layer is not affected by continuous scanning. Conversely, Klein *et al* (1996a) found that only by scanning in isopropanol (and thereby eliminating capillary forces related to the presence of a water film during measurements under ambient conditions) was it possible to acquire AFM images of CdSe nanocrystals. Scanning tunnelling spectroscopy measurements of individual InAs nanoclusters on Au required the presence of hexane dithiol tether molecules (Banin *et al* 1999, Millo *et al* 2000).

## 4. Electronic properties of nanoclusters: quantum confinement and single-electron effects

In a crystalline solid, electrons occupy effectively continuous energy bands with the occupation, width and separation of these bands determining the fundamental electrical, optical and magnetic properties of the solid. At the other end of the length scale, for individual atoms and molecules the electronic state density is discrete, resulting in, for example, intrinsically sharp spectral linewidths. Although in some respects the electronic structure of a nanocluster or nanocrystal might be said to fall somewhere between these two extremes, the situation is

complicated by the extremely small capacitance of isolated nanoclusters and crystals. This can give rise to an appreciable charging energy when a *single electron* is transferred to the cluster.

The idea of a semiconductor nanocrystal as an 'artificial atom' was briefly introduced in section 3. This important analogy stems both from the early work of Brus (1984) on carrier interactions in small semiconductor crystallites, which predicted that the electronic wavefunctions would exhibit atomic-like spatial symmetries, and from recent ultralow-temperature (i.e. sub-kelvin) electrical transport measurements on lithographically patterned quantum III–V dots (see, for example, Kouwenhoven and Marcus 1998, McEuen 1997). Although the *artificial atom* concept is referred to throughout the following sections, it is important to remember (see Zrenner's review of interband optical spectroscopy in quantum dots (Zrenner 2000)) that a nanocrystal, being a fragment of a crystalline lattice, will exhibit the excitations associated with a solid. In particular, phonon interactions will be present: the signature of longitudinal optical phonon resonances is clearly visible in the optical spectra of individual nanocrystals (see section 5.4). Similarly, only for precisely defined nanometre-scale objects (such as the fullerene family of molecules discussed in section 7) will the energy levels of one isolated nanocrystal be identical to those of another. Colloidally synthesized (or MBE-grown) nanocrystals have a range of sizes and shapes which will shift energy level positions, spacing and degeneracies from cluster to cluster.

The effects of quantization on the electronic density of states may be summarized using the simple schematic illustrations shown in figure 20. For 0D structures (variously termed nanoclusters, nanocrystals or quantum dots), the discrete, atomic-like states can be considered as arising from the superposition of bulk $k$-states with a concomitant dramatic increase in oscillator strength. (The oscillator strength, $f$, provides a measure of the strength of an optical transition and is given by

$$f = \frac{2m\omega}{\hbar}|\langle f|\boldsymbol{\eta}\cdot\boldsymbol{r}|i\rangle|^2 \tag{1}$$

where $m$ is the free-electron mass, $\omega$ is the angular frequency of the light, $f$ and $i$ are the final and initial states of the transition and $\boldsymbol{\eta}$ is the polarization vector of the light.) Furthermore, the bandwidth narrowing that occurs as the cluster size approaches the atomic limit results in dramatic size-tunable changes in the semiconductor band gap.

That band-gap widening is a natural consequence of cluster size reduction is readily seen from a consideration of an elementary expression for the energy of the lowest excited electronic state of a model spherical semiconductor cluster (Brus 1986):

$$E^* \approx E_g + \frac{\hbar^2\pi^2}{2R^2}\left[\frac{1}{m_e}+\frac{1}{m_h}\right] - \frac{1.8e^2}{\varepsilon_2 R} + \overline{\frac{e^2}{R}\sum_{n=1}^{\infty}\alpha_n\left(\frac{r}{R}\right)^{2n}}. \tag{2}$$

Here, $m_e$ and $m_h$ are the electron and hole effective masses respectively, $\varepsilon_2$ is the dielectric constant of the semiconductor, $E_g$ the band-gap energy for the bulk semiconductor lattice, $R$ is the radius of the cluster,

$$\alpha_n = (\varepsilon - 1)(n+1)/[\varepsilon_2(\varepsilon n + n + 1)]$$

and $\varepsilon = \varepsilon_2/\varepsilon_1$ ($\varepsilon_1$ is the dielectric constant of the medium surrounding the crystal).

The second term is simply the quantum confinement energy for a particle in a box whereas the third term arises from the Coulombic electron–hole interaction. The final term, the position-dependent ($r$-dependent) solvation energy, arises from dielectric screening. For small enough $R$ the second term produces an increase in band-gap energy for decreasing $R$. That the quantum confinement and Coulomb energy terms are simple additive 'corrections' to the band gap of the infinitely extended crystalline solid is largely due, as discussed by Brus (1986) and noted above, to the feature that one can represent the cluster states as a superposition of bulk $k$-states.

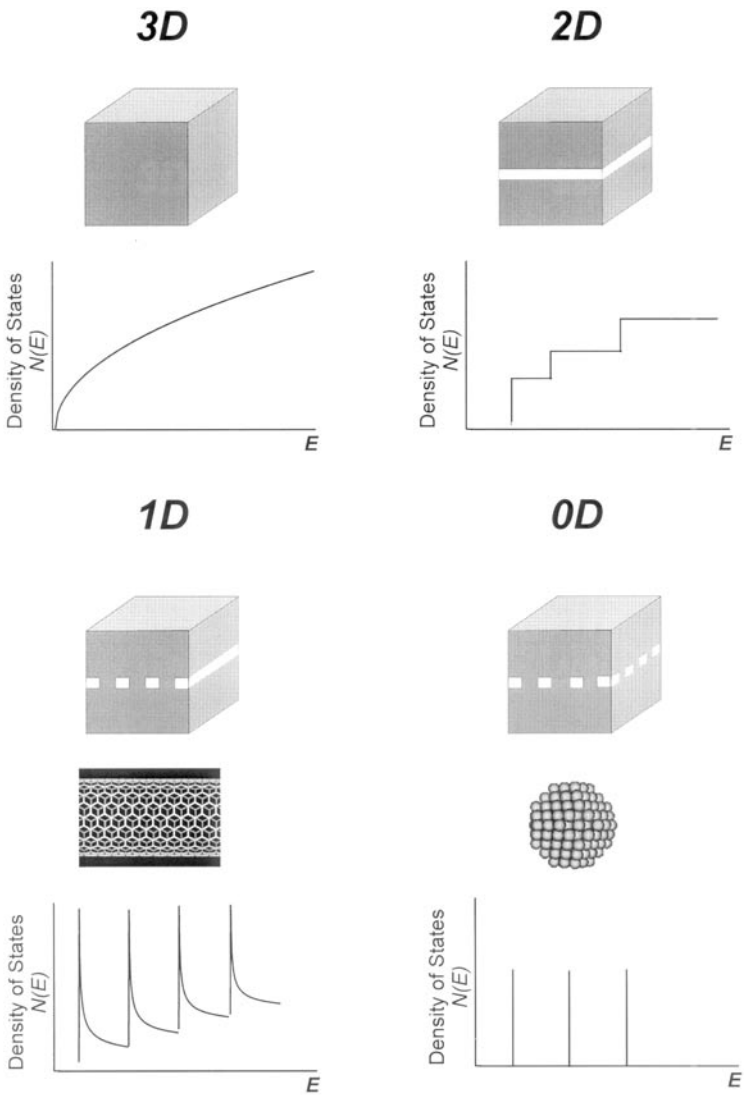


**Figure 20.** A schematic diagram illustrating the changes in electronic density of states that occur as dimensionality is varied from 3D to 0D, assuming free electrons. For a 3D solid, as described in solid-state textbooks (see, for example, Ashcroft and Mermin 1976), the density of states has a $\sqrt{E}$ dependence. In 2D, as depicted by the schematic illustration of a quantum well structure shown in the figure, the density of states is a step function. (Note that the density-of-states plot shown here is representative of a realistic 2D system where the length scale in the $z$-direction, although small, is finite. In an ideal 2D system, i.e. where the length in the $z$-direction $\rightarrow$ 0, the density of states is a constant.) 1D systems, i.e. quantum wires, are represented by the schematic drawings of an MBE-grown wire and a carbon nanotube (although, as discussed in section 7.2, nanotubes may also exhibit electron confinement along their length). The density of states for a 1D system has a $1/\sqrt{E}$ dependence and, thus, exhibits singularities near the band edges. Finally, a 0D system, as represented by the illustration of an MBE-grown quantum dot and a nanocrystal, will have discrete, $\delta$-function-like electronic states.

In addition to the size-dependent modification of the band structure, the very small capacitance associated with a nanoscale object strongly affects its electronic structure, giving

rise to single-electron charging effects that are characterized by the presence of Coulomb-blockade and Coulomb-staircase features in current–voltage plots. The Coulomb-blockade mechanism was observed experimentally as early as 1951 (Gorter 1951) and there have been a number of comprehensive recent reviews of single-electron effects (Devoret and Grabert 1992, Altshuler *et al* 1991, Meirav and Foxman 1995). In the following, only single-electron effects in colloidal nanoclusters—a topic that currently attracts considerable research interest—will be discussed. The reader is referred to the reviews cited above for details of single-electron effects in more conventional, lithographically defined tunnel junctions and nanostructures.

Figure 21 schematically illustrates the origin of single-electron charging in a nanocluster coupled to a source and drain. Note that the nanocluster must be weakly coupled via tunnel barriers to the source and drain electrodes. By weakly coupled we mean that the electronic wavefunction must decay rapidly away from the nanocluster, leading to an effective localization of electronic charge on the cluster. It can be shown that to fulfil this criterion, the resistance of the tunnel junction must exceed the resistance quantum, $h/e^2 = 25.8\,\mathrm{k}\Omega$ (Devoret and Grabert 1992). The source and drain may be either lithographically patterned electrodes (Klein *et al* 1997) or be formed by an STM tip and the substrate on which the nanocluster is adsorbed. The energy needed to add an electron to the nanocluster is given by

$$E_{add} = e^2/C + \Delta E \tag{3}$$

where $C$ is the capacitance of the cluster and $\Delta E$ is the energy difference between the single-particle eigenstates (i.e. the energy required to move to the next unoccupied electronic level in the cluster). This *constant interaction* model assumes that the Coulomb interaction between electrons on the cluster is independent of the total number of electrons and is simply given by the charging energy term $e^2/C$.

Referring to the energy level diagram shown in figure 21(b)(i), in order to add or remove an electron to/from the cluster, the Fermi level of the electrode on the left (the source) must be either raised above the electrochemical potential associated with having $N + 1$ electrons on the cluster, $\mu_{N+1}$ (as shown in figure 21(b)(ii)), *or* lowered below $\mu_N$, the electrochemical potential arising from $N$ electrons. There will thus be a range of bias voltage over which the source Fermi level satisfies neither of these criteria, giving rise to a region of zero conductance. This is clearly seen in figure 21(c), an STM $I$–$V$ spectrum (measured at room temperature) for a single 1.8 nm Au cluster tethered to a Au substrate via a dithiol molecule (Andres *et al* 1996a) clearly illustrating that the dithiol molecule is of sufficiently high resistance to act as a tunnel barrier. In addition, the signature of Coulomb-*staircase* behaviour, arising from the addition of single electrons, is visible as the plateaus in the data. The asymmetry in the $I(V)$ curve is not expected on the basis of the simple model outlined above and arises from the presence of a fractional charge (in this case, $\sim 0.2e$) on the cluster. Similar single-electron charging effects have been observed in a large number of STS measurements on individual, isolated nanoclusters including Pt (van Kempen *et al* 1995, Dubois *et al* 1996) Au (van Kempen *et al* 1995, Dorogi *et al* 1995, Feldheim *et al* 1996, Dubois *et al* 1996, Simon *et al* 1998, Ohgi *et al* 1998, Chi *et al* 1998, Harrell *et al* 1999), Si (Klyachko and Chen 1997) and CdS (Ogawa *et al* 1995)

Klein *et al* (1996a) developed an important alternative to STM-based electrical measurements of colloidally synthesized nanoclusters as illustrated in figure 22(a) (figure 1 from Klein *et al* 1996a). Optical lithography-defined Au bonding pads were functionalized with hexanedithiol molecules which bound either Au or thiol-capped CdSe nanocrystals (as shown in figure 22(b)). $I$ versus $V$ and $\mathrm{d}I/\mathrm{d}V$ characteristics measured at 4.2 K for a 5.8 nm diameter CdSe nanocrystal are shown in figure 22(c). In addition to a clear Coulomb gap and a Coulomb staircase with $\sim$110 meV period, additional structure which the authors tentatively assigned to

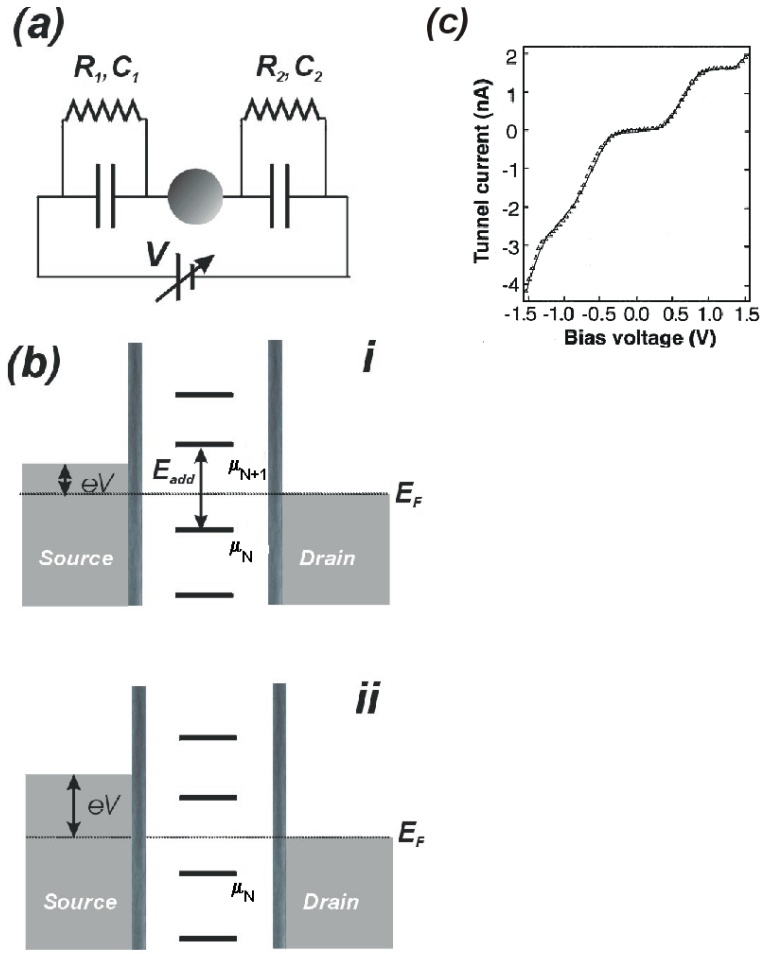


**Figure 21.** (a) The equivalent circuit for a double-tunnel-barrier junction formed between an STM tip, a nanocrystal and a substrate. (b) Schematic energy level diagrams illustrating the origin of Coulomb blockade in nanocrystal systems. In (i) the electrochemical potential associated with the addition of the $(N + 1)$th electron lies well above the Fermi level of the source (which due to the bias voltage, $V$, between the tip and sample is at an energy $eV$ above that of the drain). Conduction through the dot will not occur until the bias voltage is large enough that the Fermi level of the source is coincident with (or above) the energy level associated with having $N + 1$ electrons on the cluster, as shown in (ii). Note that it is also common for the drain–source voltage to be kept constant and a gate voltage used to vary the positions of the nanocrystal energy levels with respect to the drain/source Fermi levels. (c) STM $I(V)$ data for a passivated 1.8 nm Au cluster. In addition to the presence of a Coulomb gap around 0 V (the asymmetry about the 0 V position arises from a partial charge on the cluster), Coulomb-staircase behaviour is observed (Andres *et al* 1996a).

either longitudinal optical (LO) phonon interactions or as arising from the quantized electronic energy levels of the cluster is also observed in the $\mathrm{d}I/\mathrm{d}V$ spectrum. In a later publication, Klein *et al* extended this work to measure directly the addition energies for successive carriers on a CdSe nanocrystal finding that for the second, third and fourth holes these were: $14 \pm 2$ meV, $29 \pm 3$ meV and $22 \pm 2$ meV respectively. The authors note that, from the simple Coulomb-blockade model outlined above, one would expect that the energy required to add the second and fourth holes would be appreciably smaller than that needed to add the third because the

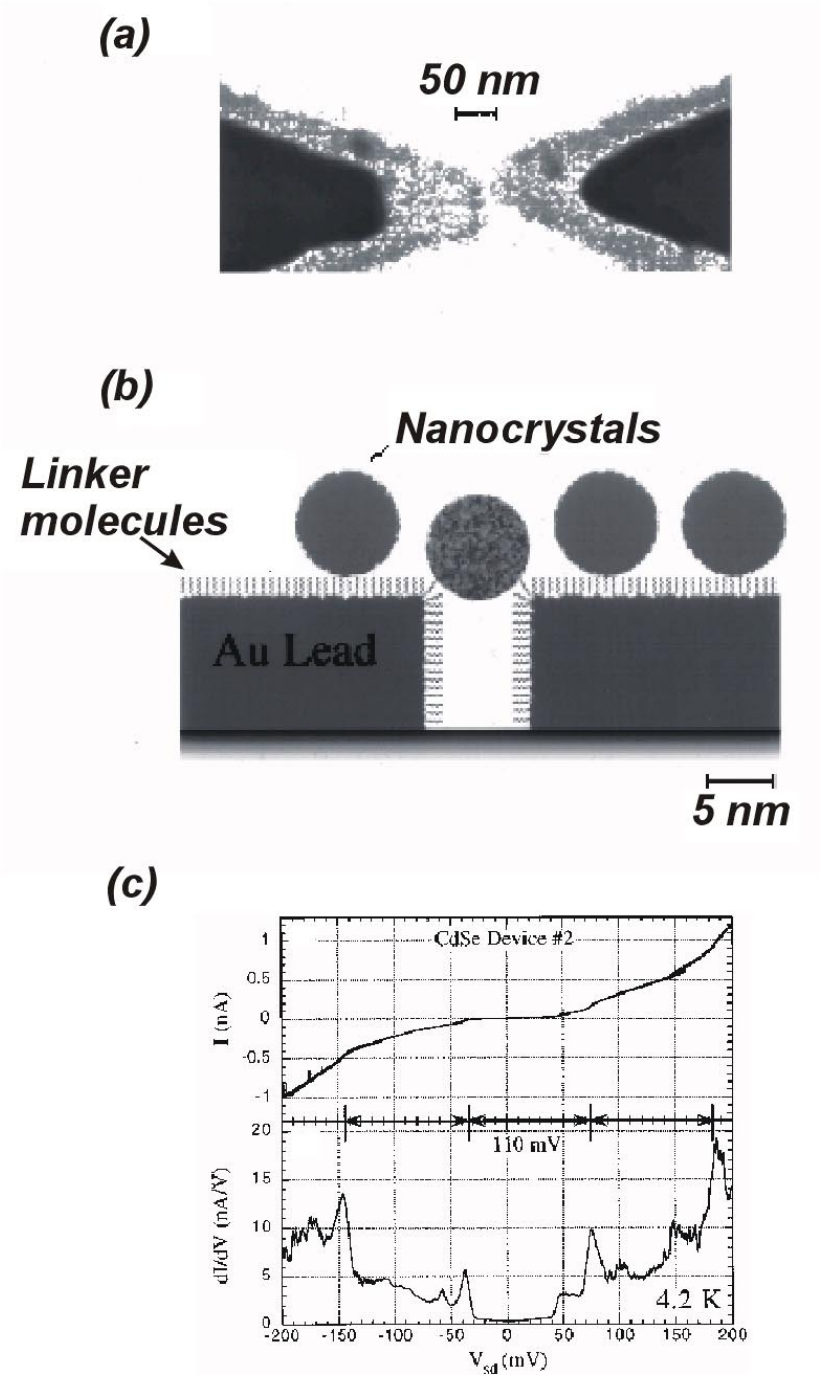


**Figure 22.** An alternative to STM-based probing of the electrical characteristics of nanocrystals developed by Klein *et al* (1996a). (a) A schematic diagram, (b) an SEM image of functionalized Au bonding pads and (c) $I(V)$ and $\mathrm{d}I/\mathrm{d}V$ characteristics measured at 4.2 K for a 5.8 nm diameter CdSe nanocrystal bound between the electrodes.

second and fourth holes will occupy doubly degenerate levels. That is, the energy needed to add the second and fourth holes is simply the charging energy, $U$, whereas addition of the third hole requires $U + \Delta E$.

In the work described above, a trial-and-error approach was used to deposit colloidal particles in the gap between the electrodes. That is, following condensation of nanocrystals from a solvent onto the surface there was rather a low probability that an individual crystal would bridge the gap between two electrodes. Dekker's group at the University of Delft have developed a novel method of reproducibly coercing nanoclusters to move between two electrodes (Bezryadin *et al* 1997). This involves exploiting the strong electric field that exists between the two appropriately biased electrodes to electrostatically trap a particle (figures 23(a), (b)). The $I$–$V$ curves shown in figure 23(c) clearly illustrate the presence of a small Coulomb gap (55 meV) at 4.2 K.

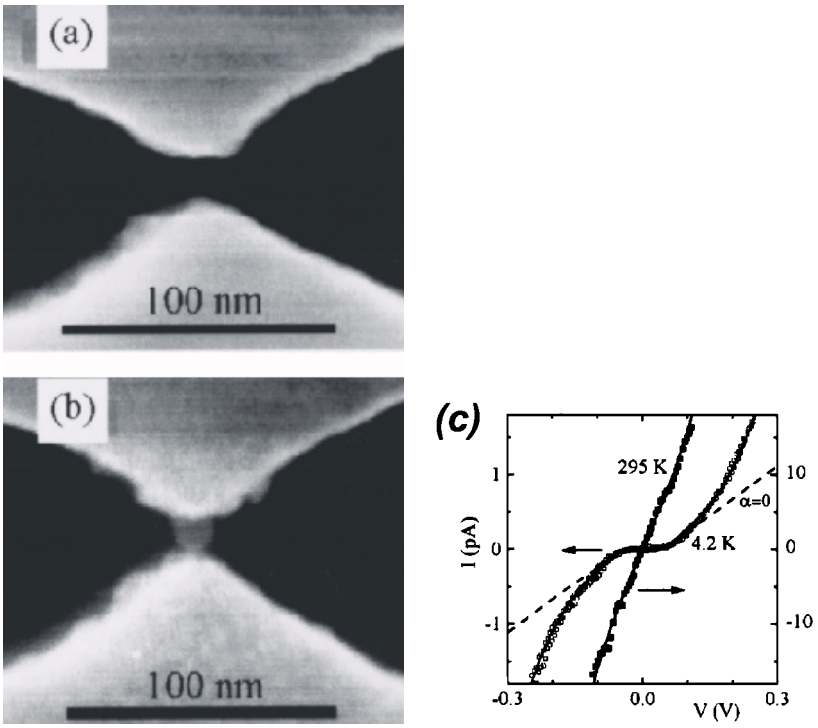


**Figure 23.** (a), (b) Electrostatic trapping of a Pd colloidal nanoparticle between two electrodes. (c) $I$–$V$ characteristics measured at 4.2 K.

Banin *et al* (1999) and Millo *et al* (2000) have extended electrical transport measurements of quantized states in nanocrystals to ∼6 nm diameter InAs colloids. Cryogenic (4.2 K) scanning tunnelling spectroscopy was used to identify atomic-like electronic states which exhibited s and p character. This symmetry was inferred from the observation of single-electron charging multiplets in the tunnelling conductance spectrum, as shown in figure 24. Focusing on the peaks at positive bias shown in the figure (where electrons are tunnelling from the tip into empty conduction band states of the cluster), a doublet whose first peak is located at ∼0.5 eV is followed by six closely spaced peaks (first peak at ∼1.0 eV). Following similar arguments to those outlined above for the work of Klein *et al* on CdSe colloids, the spacing of the peaks in the doublet is simply the charging energy for the cluster (0.11 eV), as

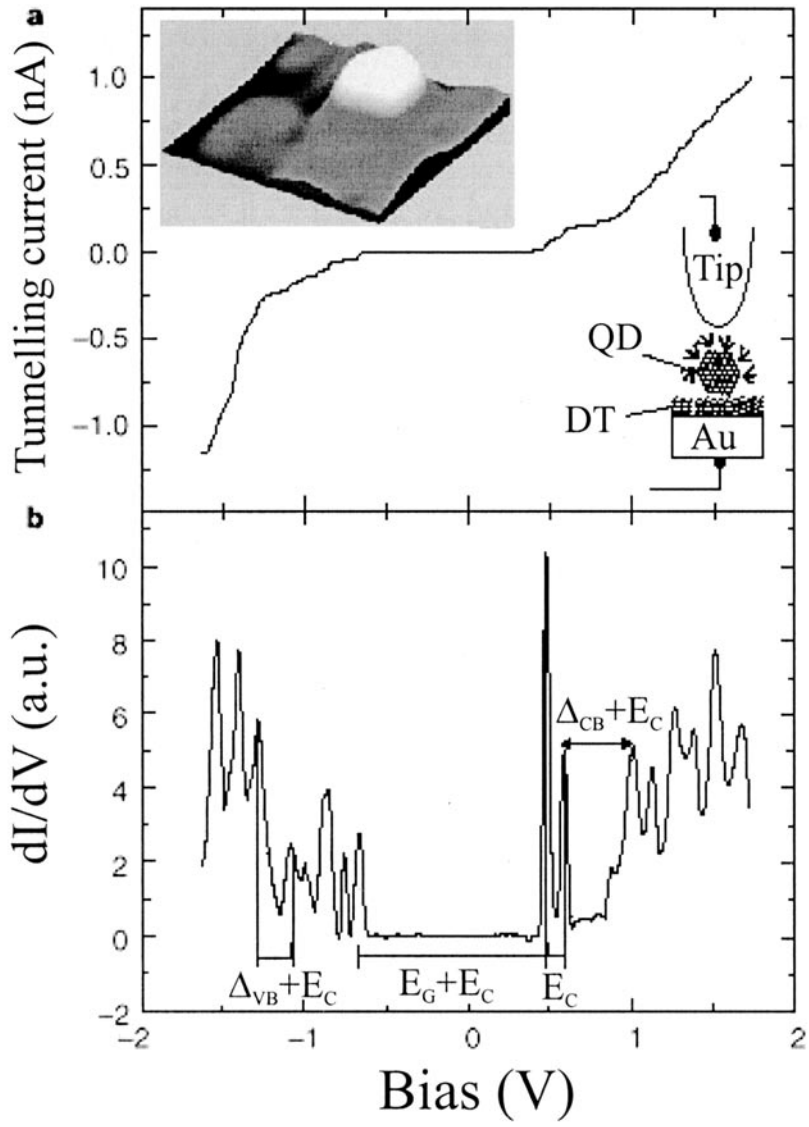


**Figure 24.** Scanning tunnelling spectroscopy of an individual InAs nanocrystal at 4.2 K. As discussed in the text, the multiplets observed in the differential conductance spectrum arise from tunnelling into discrete, atomic-like electronic states of the nanocrystal (Banin *et al* 1999).

the lowest unoccupied state of the cluster will have s character and thus be doubly degenerate. The separation of the doublet and the sixfold multiplet of peaks represents the energy level spacing between the s state and the next highest energy level which will be of p character and may thus be occupied by six electrons. The gap of zero conductance observed around zero volts arises from the sum of the cluster band gap (estimated to be $\sim$1 eV) and the Coulomb gap. The size of the zero-conductance gap, the spacing of the two groups of peaks and the spacing of peaks within the s- and p-derived multiplets all increase with decreasing cluster size, as expected from simple quantum confinement arguments.

Magnetotunnelling spectroscopy (not STM-based spectroscopy) has very recently been applied by the Nottingham Semiconductors group (Vdovin *et al* 2001) to, for the first time, map the spatial distribution of ground and excited electronic states in MBE-grown InAs nanoclusters (figure 25). This research builds on previous work on mapping wavefunctions in lithographically patterned quantum dots (Beton *et al* 1995b) and represents a powerful complement to the electronic state-sensitive tunnelling spectroscopy measurements on InAs nanocrystals discussed above. In addition, the technique—unlike scanning probe methods—is not restricted to nanocrystals exposed at or adsorbed on a surface (i.e. it is capable of probing buried nanocrystals).

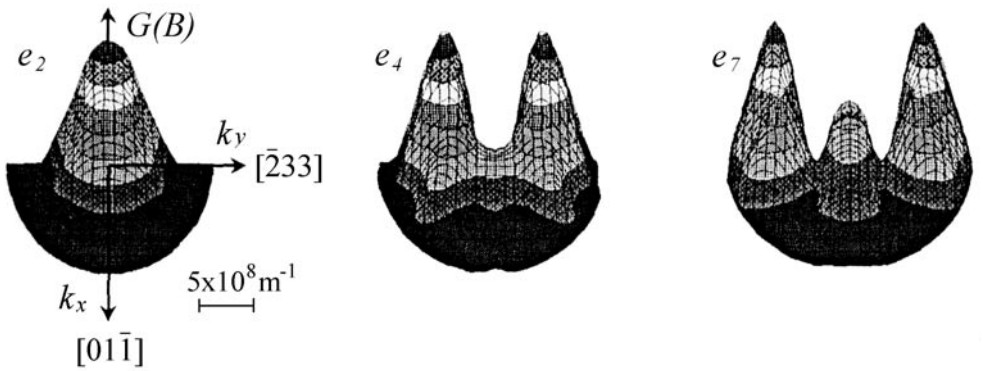


**Figure 25.** The magnetic field dependence of the differential conductance of MBE-grown InAs nanocrystals has been used to image electronic wavefunctions within the crystals. By rotating the magnetic field in the $(x, y)$ (i.e. growth) plane and measuring the differential conductance at fixed angular increments of $B$ it is possible to produce a map of $|\Psi(k_x, k_y)|^2$—the projection in $k$-space of the probability density of a given electronic state in the nanocrystal. The labels $e_2$, $e_4$ and $e_7$ refer to particular resonances in the differential conductance. $e_2$ represents a ground-state orbital. The probability density for the $e_4$ and $e_7$ resonances exhibits the nodal structure expected for excited states of the nanocrystal (Vdovin *et al* 2001).

We now turn to electrical measurements of cluster aggregates and networks, discussing measurements of 1D chains, 2D systems (monolayers) and 3D (bulk) material in turn. Braun *et al* (1998) found that the $I(V)$ characteristics of a 1D chain of (rather large, 30–50 nm) Ag particles attached via DNA exhibited strong non-linearities which were proposed to arise from both Coulomb charging and, significantly, the presence of a high degree of both size- and packing-related disorder. Using a device geometry and processing very similar to that employed by Klein *et al* discussed above, chains of hexanedithiol particles have been positioned between (functionalized) Au electrodes (Sato *et al* 1997). The transport characteristics of a three-cluster chain were found to be in very good agreement with a Monte Carlo simulation of sequential single-electron tunnelling through the coupled clusters.

Andres *et al* (1996b) have synthesized *linked cluster networks* consisting of Au nanoclusters covalently linked via aryl di-isonitrile molecules. They found that the conductance of the network (see figure 26(a)) exhibited Coulomb charging behaviour and could be described via the following simple Arrhenius relation (Neugebauer and Web 1962):

$$G = G_\infty \mathrm{e}^{-E_A/kT} \tag{4}$$

where $G_\infty$ is the conductance as $T \to \infty$ and $E_A$ is the electrostatic activation energy for electron hopping (i.e. the Coulomb charging energy for the network), calculated, from the data in figure 26(a), as 97 meV (i.e. $>kT$ at 300 K). From this relation, the intercluster

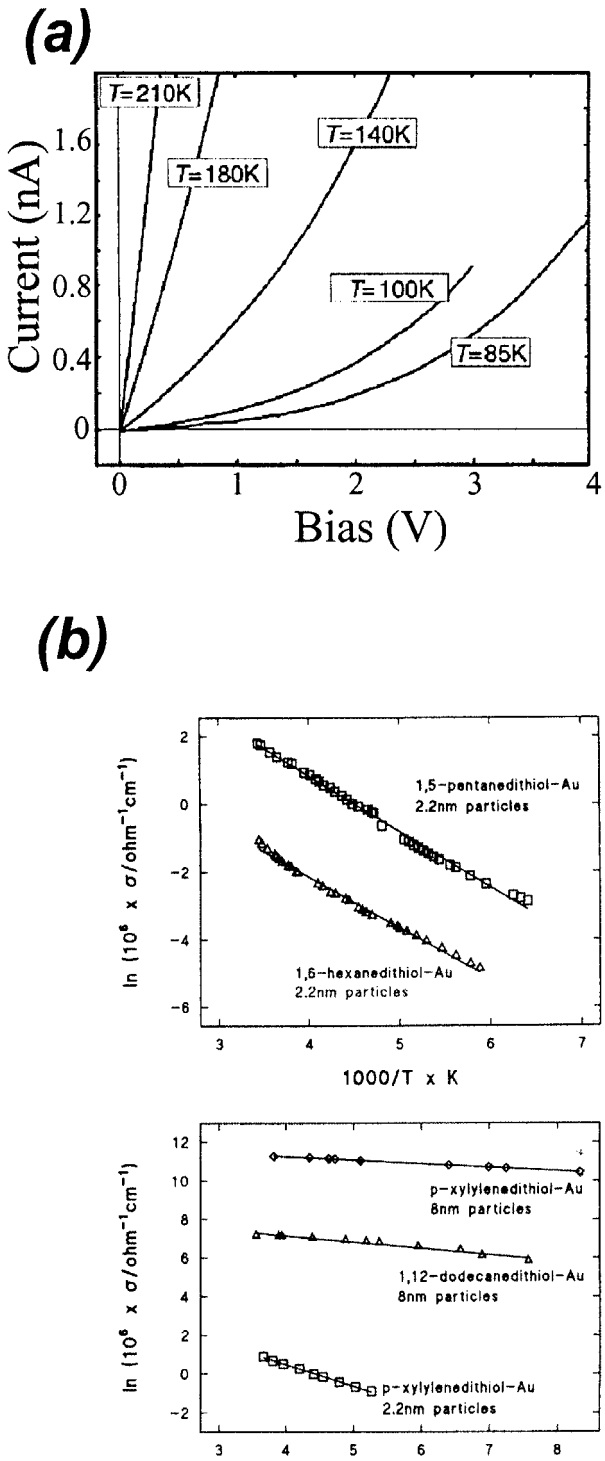


**Figure 26.** Conductance measurements for cluster networks. (a) $I(V)$ data for a linked cluster network consisting of Au nanocrystals covalently linked with aryl di-isonitrile molecules. (b) Conductance data for 2.2 nm and 8.0 nm Au clusters cross-linked with thiol molecules (Brust *et al* 1995).

resistance was calculated as ∼0.9 MΩ. Somewhat similar results were reported by Chi *et al* (1998) for STS measurements on a monolayer of $((Ph_2C_6H_4SO_3H)_{12}Cl_6)Au_{55}$ clusters. Using complex impedance spectroscopy (see Schmid and Chi (1998) for a discussion of this powerful technique) and a novel method for compressing a nanocluster monolayer, Markovich *et al* (1998) reported a reversible metal–insulator transition in an ordered monolayer of 3.5 nm diameter propanethiol-stabilized Ag clusters. On compressing the monolayer so that the intercluster spacing was less than 0.6 nm, the electrical response was of inductive, metallic character. Above this spacing the monolayer exhibited an RC-like response, consistent with localized states and, thus, activated hopping-derived conduction. These results were explained in terms of both an increased tunnelling rate on compression and the contribution of *delocalized* electronic states in well-ordered cluster regions.

Brom *et al* (1991) found that for pressed pellets (i.e. bulk polycrystalline material) of ligand-stabilized Au clusters, $\ln(G)$ was dependent not on $T^{-1}$ but on $T^{-1/2}$. However, Brust *et al* (1995) in a study of the conductance of pellets of both 2.2 nm and 8.0 nm Au particles cross-linked with thiol molecules (figure 26(b)) found that their data followed the $T^{-1}$-dependence given above. Furthermore, a range of thiols of different lengths were used as linkers and a strong dependence of conductivity on thiol length and, hence, intercluster separation observed. In related work, Schmid and Chi (1998) and Simon *et al* (1998) have discussed the correlation between the separation of $Au_{55}$ and $Pd_{561}$ clusters (controlled via various molecular spacers) respectively, finding that for Au the Coulomb gap scales with the intercluster separation and may be varied from 0.15 eV to ∼0.23 eV. For densely packed $Pd_{561}$ clusters the activation energy for conduction was 20 meV. Inserting 4, 4′-diamino-1, 2-diphenyl-ethane spacer molecules increased the activation energy to 50 meV.

Finally with regard to the electrical transport properties of nanoclusters, a transition from Coulomb blockade to ohmic behaviour for scanning tunnelling spectra measured on individual Ag clusters, 2D superlattices and 3D fcc cluster superlattices has been observed by Taleb *et al* (2000). They interpret their results in terms of the contribution of intercluster electron tunnelling for 2D and 3D lattices.

## 5. Optical properties of nanoclusters

### *5.1. Plasmon resonances in metal clusters*

A striking property of a colloidal solution of noble-metal nanoclusters is its intense colour. It was the dependence of solution colour on Au colloid size that prompted Mie (1908) to apply Maxwell's equations, with the appropriate boundary conditions for spherical particles, to the calculation of the absorption spectra of small Au clusters. A key feature of the absorption spectra of noble-metal nanocrystals is the presence of a strong band in the visible region, arising from the collective oscillation of conduction electrons (i.e. surface plasmons) in response to the external electromagnetic field (Bohren and Huffman 1983) As discussed by, for example, Link and El-Sayed (1999), although the total extinction cross-section for the particles, $\sigma_{ext}$ (due to both absorption and scattering), arises from a summation over all electromagnetic multipole oscillations, for nanocrystals which are small compared to the wavelength of the exciting radiation ($\lesssim 0.1\lambda$) the dipole approximation may be used and Mie theory leads to the following expression for $\sigma_{ext}$ (Papavassiliou 1980):

$$\sigma_{ext} = \frac{9V\varepsilon_m^{3/2}\omega}{c}\frac{\varepsilon_i(\omega)}{[\varepsilon_r(\omega)+2\varepsilon_m]^2+\varepsilon_i(\omega)^2} \tag{5}$$

where $V$ is the (spherical) particle volume, $\omega$ the angular frequency of the exciting radiation, $\varepsilon_m$ the dielectric constant of the medium surrounding the particle and $\varepsilon_r$ and $\varepsilon_i$ the real and imaginary parts of the dielectric function of the particle material respectively.

From equation (5), Mie theory predicts that the bandwidth and peak height of the plasmon resonance (which occurs when $\varepsilon_r(\omega) \approx -2\varepsilon_m$, if $\varepsilon_i$ is small or weakly dependent on $\omega$) are determined solely by $\varepsilon_i$. Thus, on the basis of (5), there should be no dependence of resonance position or width on particle size, only a volume-dependent variation in resonance *intensity*. However, a large number of experimental studies (see, for example: Hellier *et al* 1951, Wilcoxon *et al* 1993, 1998, Huffman 1990) have clearly demonstrated that as nanocluster size decreases there is a dramatic increase in the plasmon resonance bandwidth which may be accompanied by shifts in the resonance position (Kreibig and Genzel 1985). To account for these findings, the basic Mie theory has been extended (Kreibig and Vollmer 1995) to include the fundamental assumption that the dielectric function of metal nanoparticles is size dependent, thus explaining the dependence of resonance bandwidth on particle radius.

The breakdown of classical Mie theory and the concomitant need to introduce a size-dependent dielectric constant have been proposed to occur, at least for free-electron metals, when the cluster diameter ($2R$) becomes smaller than the electron mean free path ($l$) in the bulk metal (Fragstein and Kreibig 1969, Doremus 1965), ∼50 nm for Au assuming a Drude–Sommerfeld model (Alvarez *et al* 1997). With $2R < l$, in a classical picture the electrons are scattered by the surface, strongly affecting their response to the incident electromagnetic field. As first discussed by Fragstein and Kreibig (1969), this results in a $1/R$ dependence of the plasmon bandwidth. More rigorous quantum mechanical calculations by both Kawabata and Kubo (1966) and, more recently, Persson (1993) also produce a $1/R$ dependence of the plasmon bandwidth.

Figure 27 shows UV–visible absorption spectra for 9, 22, 48 and 99 nm (size distribution ∼10% in each case) charge-stabilized Au nanoparticles, normalized at their respective absorption maxima (517, 521, 533 and 575 nm). The increase in plasmon bandwidth with

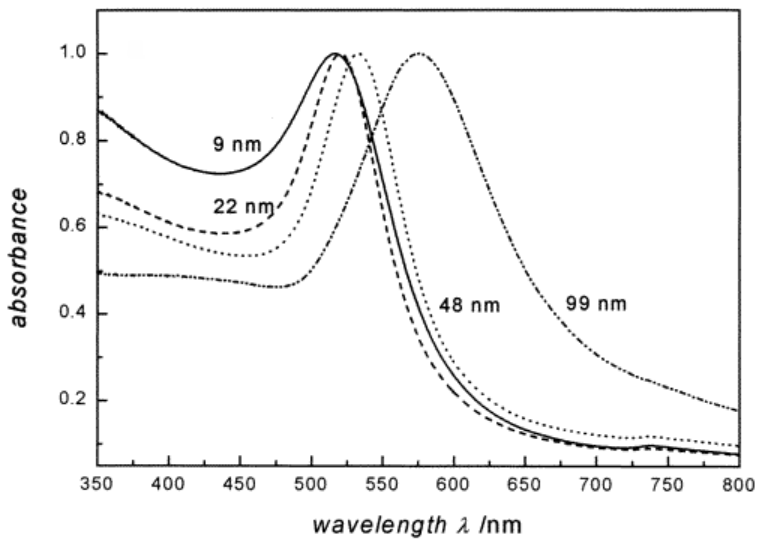


**Figure 27.** UV–visible absorption spectra for 9, 22, 48 and 99 nm diameter Au nanoparticles (Link and El-Sayed 1999).

decreasing size observed for nanoparticles of less than ∼30 nm diameter arises, in a simple classical picture, from the dominant contribution of surface scattering to the phenomenological damping constant, $\gamma$ (used in Drude–Sommerfeld free-electron-gas theory to account for scattering processes). The surface scattering rate, $\omega_s$, may be expressed in terms of the Fermi velocity of the electrons, $v_F$, the radius of the particle and a proportionality factor, $A$, whose precise value has been the subject of some debate (see Hovel *et al* 1993):

$$\omega_s = Av_F/R.$$

Above ∼30 nm, the bandwidth increases because the dipole approximation is no longer valid in Mie theory and higher-order (quadrupole and octopole) modes contribute to the extinction cross-section.

To obtain a more detailed microscopic understanding of the dependence of plasmon bandwidth on size, a number of groups, building on earlier work by Heilweil and Hochstrasser (1985), have considered their results in terms of a molecular spectroscopy-derived two-level model, where the total resonance damping constant (dephasing time) is dependent on both the population relaxation time and a 'pure' dephasing time which originates from scattering that changes the plasmon wavevector but not its energy. For particles of 2 to 20 nm diameter, as the particle size decreases the relaxation time decreases (Stella *et al* 1996) (due to surface scattering) and there is considerably weaker electron–phonon coupling (Roberti *et al* 1995, Link and El-Sayed 1999), consistent with theoretical predictions (Belotskii and Tomchuck 1992).

Photoluminescence (PL) studies of both charge-stabilized and surfactant-stabilized Au clusters (Wilcoxon *et al* 1998) illustrated that relatively intense photoluminescence occurred only when the nanoclusters were sufficiently small (<5 nm). The PL spectra provided strong evidence that the chemical state and structure of the nanocluster surface strongly affected the strength of the coupling between the incident radiation and the surface plasmon.

In a series of recent experiments, Whetten and co-workers (Schaaf *et al* 1997, Logunov *et al* 1997, Alvarez *et al* 1997) have studied the optical absorption spectra of very small (1.4 nm to 3.2 nm diameter) thiol-passivated Au nanocrystals, motivated, in part, by the quantum size effects (QSEs) associated with Au clusters of diameter <2.5 nm. In addition to the Coulomb charging phenomena discussed above, sufficiently small metal clusters will exhibit quantized electronic structure (see de Heer (1993) for a detailed discussion of the shell structure associated with electronic quantization in metal clusters). The level spacing in the proximity of the Fermi energy, derived from the bulk density of states, is given by (see, for example, Kubo *et al* 1984)

$$\delta(E_F) \approx \frac{3}{2}\frac{E_F}{N_A z} \tag{6}$$

where $N_A$ is the number of metal atoms and $z$ their valence. For Au, $N_A$ needs to be less than 400 atoms and, correspondingly, the cluster diameter <2.5 nm for the mean energy level spacing to be greater than $kT$ at room temperature.

The step-like structure observed in the absorption spectra for the smallest Au particles shown in figure 28 has been tentatively assigned to transitions from filled d orbitals to quantized states in the nanocluster conduction band. Furthermore, Alvarez *et al* found that the absorption spectra of the passivated (1.4 to 3.2 nm) clusters could not be explained using a mean-free-path-derived correction to the bulk dielectric constant as outlined above. Only by taking into account the effect of the ligands (thiols) on the surface charge density could reasonable agreement with Mie theory be established, although this agreement again broke down for 1.4 nm clusters due to the quantum size effects manifest in the spectrum shown in figure 28.

Scanning probe-based measurements of the optical properties of individual metal clusters are covered in section 5.4 below.

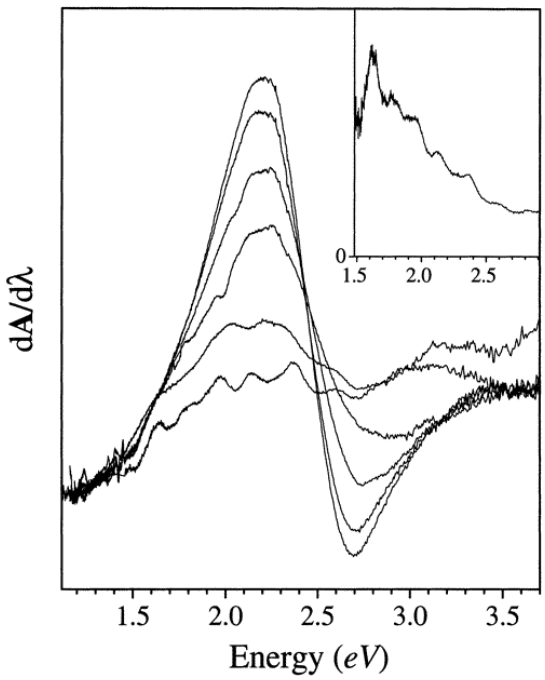


**Figure 28.** The derivative with respect to wavelength of the absorption spectra of a range of Au nanocrystal sizes (from top to bottom: 2.6, 2.4, 2.2, 2.0, 1.7 and 1.4 nm). The inset shows the logarithm of the derivative absorption spectrum for the smallest particles where, as discussed in the text, the fine structure is attributed to quantum size effects (Alvarez *et al* 1997).

### *5.2. Optical properties of compound semiconductor nanocrystals*

Figure 29 shows UV–visible absorption spectra for TOPO-capped CdSe nanocrystals with sizes ranging from 1.2 to 11.5 nm (and dispersed in hexane) (Murray *et al* 1993). The effects of quantum confinement are clearly visible: the absorption related to the band edge (or highest occupied molecular orbital–lowest unoccupied molecular orbital (HOMO–LUMO), i.e. first electronic, transition) shifts to higher energy as the cluster size is reduced. Figures 30(a) and 30(b) show the relationship between the energy of the first electronic transition and the normalized oscillator strength for this transition as a function of CdS cluster size.

The very broad absorption features observed in figure 29 are typical of both II–VI and III–V nanocrystal samples and arise from inhomogeneities in nanocrystal size, shape, environment, surface condition etc. Detailed studies of the low-temperature luminescence of CdSe nanoclusters have used fluorescence-line narrowing to selectively excite a particular subset of nanocrystals (Nirmal *et al* 1994) (see figure 31). Large exciton–LO phonon couplings were observed at low temperatures, accompanied by microsecond radiative lifetimes. Both of these effects diminished rapidly with increasing nanocrystal size and were attributed to photo-generated hole localization on the nanocrystal surface

The central role that surface states play in the optical properties of nanocrystals has also been highlighted by Nozik and Micic (1998). 'As-prepared' (3.2 nm diameter) TOPO-capped InP nanocrystals exhibit two emission bands in PL spectra: a weak near-band-edge peak at 650 nm and a much stronger band at 850 nm (Micic *et al* 1996). The latter band is attributed to radiative surface states and may be completely removed by treatment of the nanocrystals

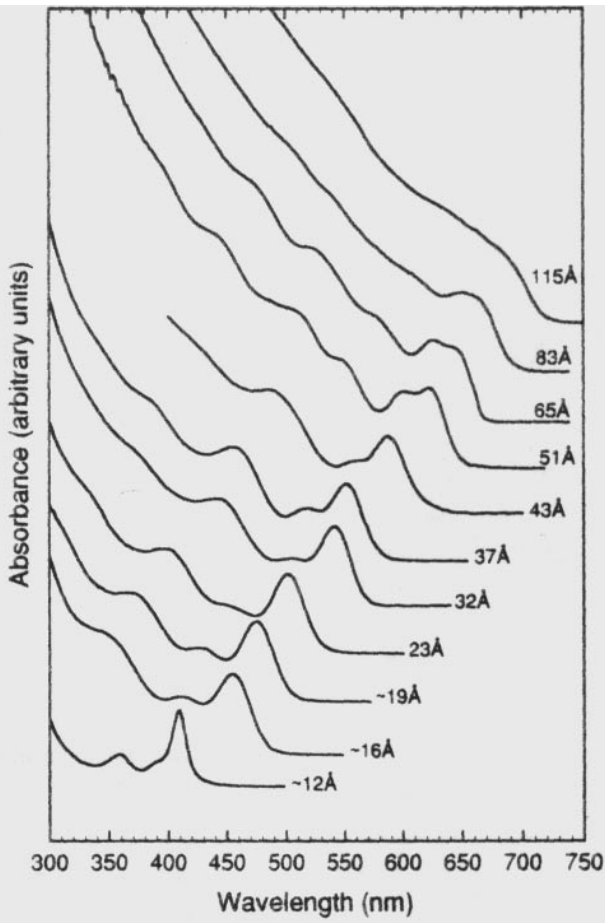


**Figure 29.** UV–visible absorption spectra for TOPO-capped CdSe nanocrystals of various sizes. (Figure 3 in Murray *et al* (1993).)

in a dilute HF solution which, it is believed, leads to the filling of phosphorus vacancies with fluoride ions. An order-of-magnitude increase in the near-band-edge PL intensity is observed following HF treatment.

A comparison of the electronic structure and transition linewidths of InP and CdSe nanocrystals (Banin *et al* 1997) revealed significant variations arising from the differences in physical parameters, including bond ionicity, carrier effective mass and spin–orbit splitting, for the two systems. LO phonon coupling is significantly smaller for the InP system since the Fröhlich mechanism—which posits that lattice distortion results from the charge redistribution induced by electronic excitation—is primarily polar in nature. Hence, for the more covalently bound InP nanocrystal, weaker LO phonon coupling is expected. Unlike in the II–VI system, coupling to the transverse optical (TO) phonon mode is also observed for InP nanocrystals. Clear differences in electronic level structure were also observed for InP as compared to CdSe nanocrystals, the smaller spin–orbit splitting in the former producing 'a congestion' of near-band-edge electronic transitions (Banin *et al* 1997).

A wealth of information on the optical properties of II–VI nanocrystals has been derived from single-nanocrystal spectroscopy—this topic is discussed in section 5.4.

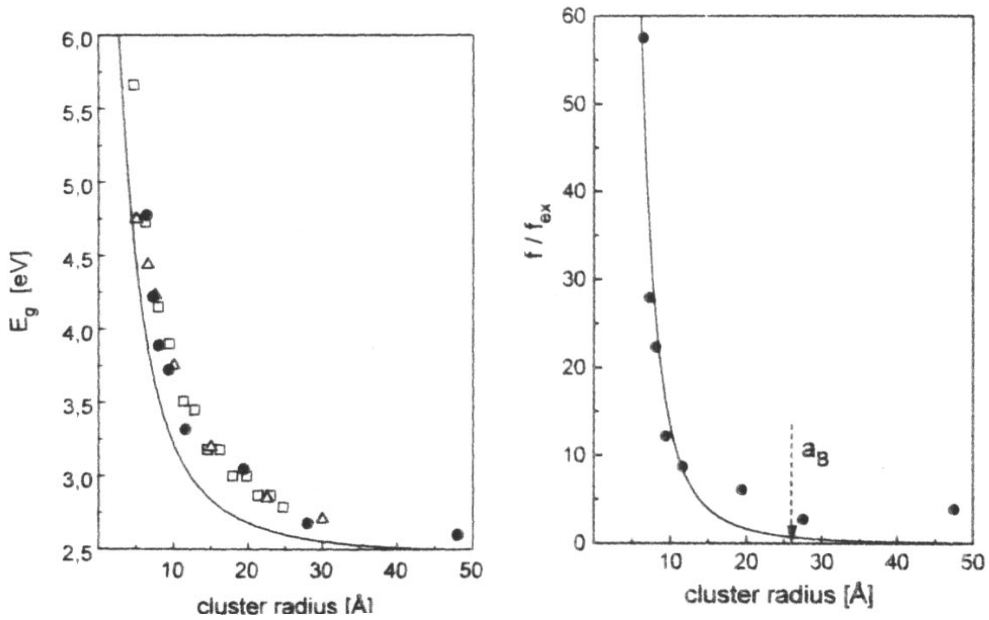


**Figure 30.** (a) The energy of the first electronic transition and (b) the normalized oscillator strength for CdSe nanocrystals as functions of size (Murray *et al* 1993).

### *5.3. Luminescence from Si nanocrystals*

A resurgence of interest in the optical properties of silicon—an indirect-band-gap semiconductor—was triggered by the discovery of relatively intense visible light emission in porous, nanostructured Si (synthesized via anodic etching in concentrated HF) at the beginning of the 1990s (Canham 1990). Three mechanisms were suggested to explain the luminescence: quantum confinement in Si nanocrystallites (Canham 1990, Cullis and Canham 1991), surface-state-related luminescence (Kanemitsu *et al* 1993) and luminescence from Si compounds such as siloxene (Brandt *et al* 1992). Although the precise luminescence mechanism remains a subject of debate, a considerable amount of information has been derived from studies of the nanometre-scale optical properties of porous silicon using photon emission STM (PESTM). This powerful technique, pioneered by Gimzewski *et al* (1988), uses the STM tip as a source of monochromatic electrons on a nanometre scale enabling, for example, local cathodoluminescence studies. The application of PESTM to porous Si (Dumas *et al* 1993, Ito *et al* 1995) has provided support for quantum confinement models of porous silicon luminescence.

More recent work on silicon luminescence has concentrated on the investigation of preformed Si nanoclusters deposited onto various substrates. What is perhaps most remarkable about this work is that, as discussed by both Dinh *et al* (1994) and, more recently, Huisken *et al* (1999), *in situ* passivated (with either hydrogen or oxygen) Si clusters do not exhibit any visible luminescence—it is only clusters that have been exposed to ambient conditions for prolonged periods of time that emit light. This is clearly illustrated in figure 32—the pronounced differences in luminescence intensity have been attributed to the presence of defects in $SiO_2$ ($SiO_2$ alone was found to be present only on air-oxidized samples whereas $SiO_x$ ($x$ ranging from 0 to 2) forms on *in situ* passivated clusters).

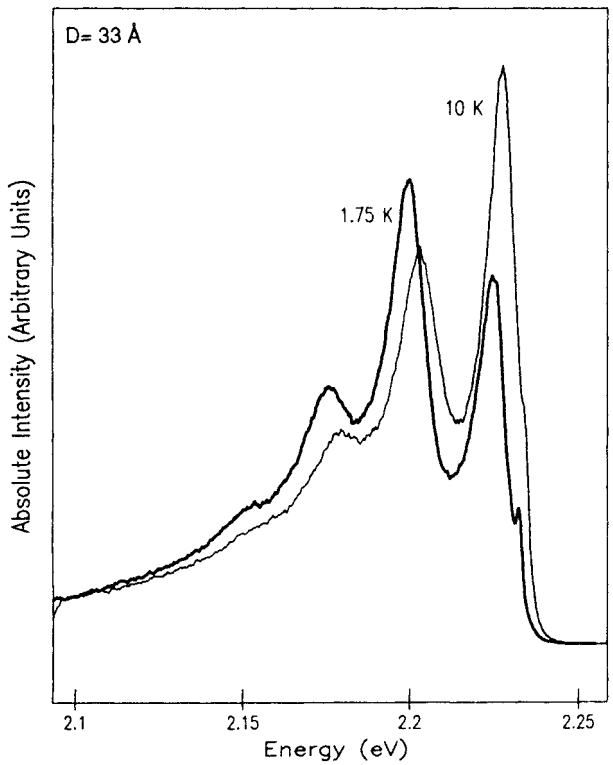


**Figure 31.** Fluorescence-line-narrowed spectra of 3.3 nm diameter CdSe nanocrystals at 1.75 K (heavy line) and 10 K (light line). A clear increase in the one-to-zero LO phonon ratio is observed. Note that the small shoulder/peak appearing at ∼2.23 eV in both the 1.75 K and 10 K spectra arises from scattered laser light (Nirmal *et al* 1994).

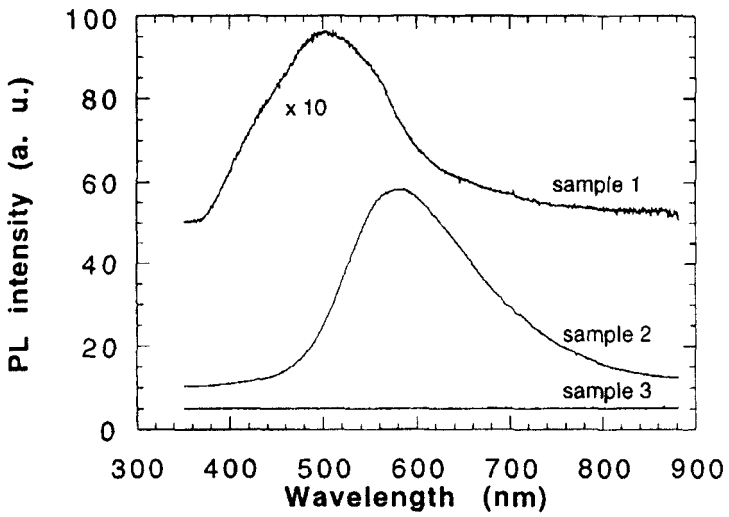


**Figure 32.** Photoluminescence spectra of oxidized silicon clusters. Sample 1 and sample 2 contained clusters of 3 nm and 5 nm diameter, respectively, and were exposed to air for more than four months. Sample 3 was oxidized in the vacuum system for five days using 300 mTorr of $O_2$ but exhibits no photoluminescence.

### *5.4. Single-cluster luminescence*

The discrete, atomic-like electronic structure of compound semiconductor nanocrystals has been verified by electronic transport measurements (section 4). One should then expect the spectral linewidths for nanocrystal optical transitions to be extremely narrow. However, as discussed by Bawendi and co-workers (Empedocles *et al* 1996, Norris and Bawendi 1996, Norris *et al* 1996, Empedocles *et al* 1999) the transition linewidths appear—in a wide range of experiments—very much broader than expected. While considerable broadening is always present in measurements on ensembles of clusters, which average over transitions related to clusters of various sizes and shapes, the nanocrystal linewidths remained wider than expected when size-selective optical techniques were used. For example, both fluorescence-line narrowing (Nirmal *et al* 1994) and two-photon microscopy (Blanton *et al* 1994) failed to produce narrow spectral features.

Techniques developed for single-molecule spectroscopy (Moerner 1994) have now been applied to the imaging and acquisition of emission spectra from nanocrystals. Bawendi and co-workers have recently presented a review of photoluminescence from individual semiconductor nanocrystals (Empedocles *et al* 1999) using single-quantum-dot spectroscopy. Here, we shall focus on just one out of the many exciting results produced using this technique: single-nanocrystal spectroscopy.

Figure 33(a) is an image of 4.5 nm diameter CdSe nanocrystals luminescing (at 10 K) under illumination from an Ar laser, with figure 33(b) illustrating the dramatic differences in linewidth between ensemble and single-nanocrystal spectra (although not shown here, there is also approximately an order-of-magnitude reduction in the linewidths observed with single-quantum-dot spectroscopy as compared with fluorescence-line-narrowing techniques; Empedocles *et al* 1996). (See Empedocles *et al* (1999) for details of the experimental set-up used to image and acquire spectra from single nanocrystals.) Differences in the luminescence intensity from nanocrystal to nanocrystal were proposed to arise from variations in the efficacy of the passivating organic layer (TOPO) capping each crystal. Longitudinal optical (LO)

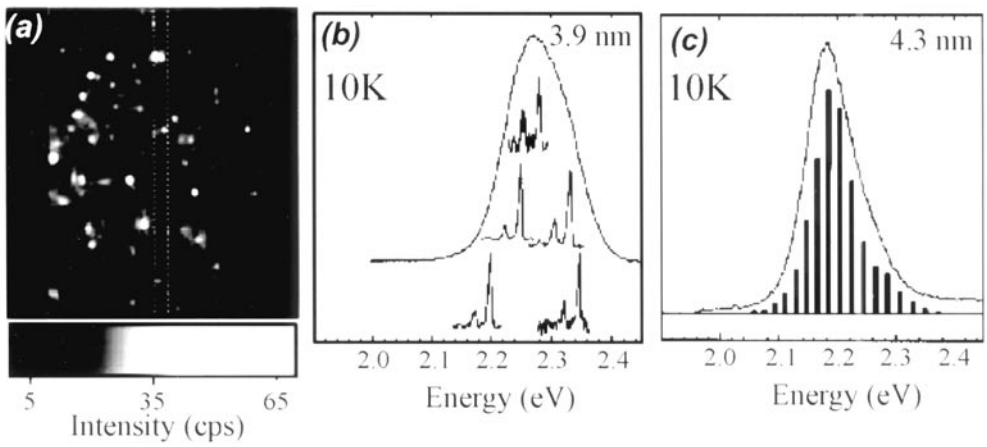


**Figure 33.** (a) A luminescence image of CdSe nanocrystals taken at 10 K. Each bright spot corresponds to luminescence from a single nanocrystal. (Note that the white dotted lines correspond to the width of the entrance slit during acquisition of a spectrum (not shown here).) (b) Ensemble and individual spectra from 3.9 nm diameter nanocrystals. (c) An ensemble spectrum plotted with a histogram of the energies of 513 single-nanocrystal spectra (including the scaled contributions of the various phonon satellites) (Empedocles *et al* 1996).

phonon satellites are clearly resolved in the single-nanocrystal spectra shown in figure 33(b) with the degree of coupling varying between crystals. Figure 33(c) shows that the ensemble spectrum can be 'recovered' from the integrated intensities of 513 individual nanocrystals (with appropriately scaled phonon line contributions) but that, as stressed by Bawendi, all information on the variation of phonon coupling is lost in the ensemble measurement.

Spectral diffusion—the shifting of spectral peaks from individual molecules due to changes in their environment—has also been observed for single nanocrystals (figure 34). A sensitive dependence of the optical properties of a nanocrystal on its environment was unexpected,

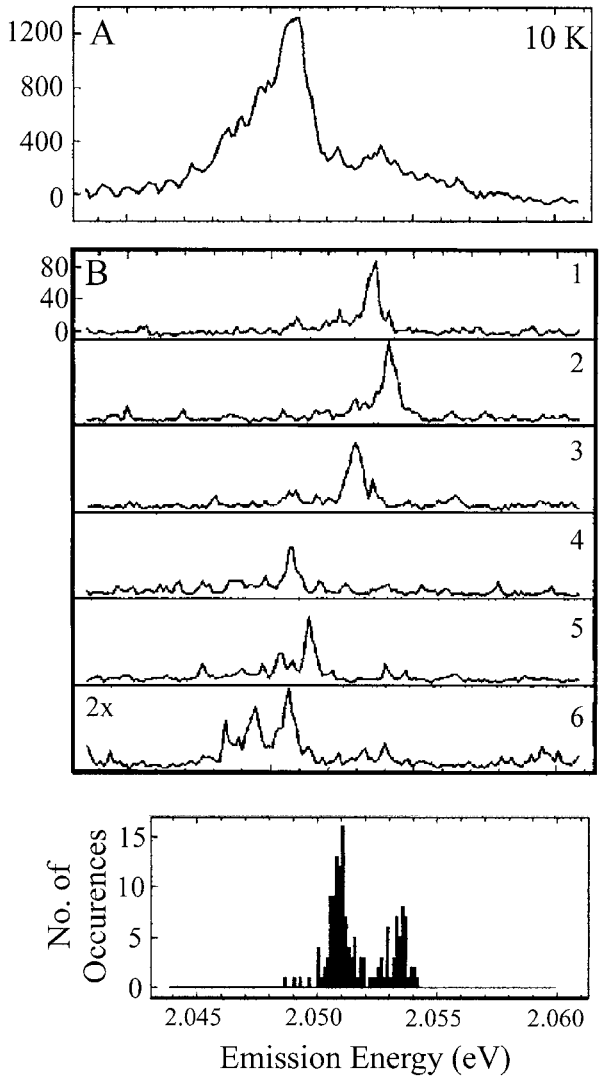


**Figure 34.** The role of spectral diffusion in luminescence spectra from a single CdSe nanocrystal. (a) A spectrum acquired with a ten-second integration time results from a superposition of a range of spectra which shift as a function of time as shown in (b). Spectra 1–6 in (b) represent spectra 1, 16, 35, 59, 84 and 150 out of 150 spectra taken during a fifteen-second period. (c) The histogram of peak positions for all 150 spectra (Empedocles *et al* 1999).

given that the exciton energy was found to be independent of the chemical state of the nanocrystal surface (Empedocles *et al* 1999). The origin of spectral diffusion in semiconductor nanocrystals has been attributed to variations in the electric field around a nanocrystal, thought to arise from movement of carriers between trap sites at (or near) the nanocrystal surface.

Scanning probe techniques, specifically scanning near-field optical microscopy (SNOM) (see Pohl (1995) for a review) and PESTM have been applied to investigate the optical properties of low-dimensional semiconductor structures. Gustafsson *et al* (1998) have reviewed recent work in this area, focusing on MBE-grown nanostructures. Both SNOM and PESTM have been shown to be capable of probing individual nanoclusters. Figure 35(a) is a PESTM photon map of light emission from an individual InAs quantum dot, with the inset showing the associated spectrum of light (Yamanaka *et al* 1998). Flack *et al* (1996) have resolved sharp, resolution-limited features attributable to the recombination of excitons confined to individual (MBE-grown) CdSe quantum dots (figure 35(b)).

As pointed out in Zrenner's review of single-quantum-dot spectroscopy (Zrenner 2000), important physics arises from the presence of tip–nanocluster interactions in both of these techniques. For SNOM, Bryant (1998) has shown that the near-field geometry selectively enhances light-hole over heavy-hole transitions and produces significant increases in oscillator strength for forbidden transitions. With PESTM, Stark effects due, for example, to inhomogeneous band bending by the electric field arising from the presence of the tip can lead to shifts in the spectral features of quantum dots (Lindahl *et al* 1996).

STM-induced light emission from individual Ag clusters has been reported by Nilius *et al* (2000) and Silly *et al* (2000). Clear size-dependent shifts in plasmon resonance were observed for (Vollmer–Weber-grown) Ag clusters on $Al_2O_3$ (figure 36). Quantum size effects were cited as playing an important role in determining the magnitude of the shift. Contrast variations in photon maps of passivated Ag clusters on Au(111) (Silly *et al* 2000) have been interpreted as representing the spatial variation of excited coupled plasmon modes.

### *5.5. Biological labelling with semiconductor nanocrystals*

In recent examples of the increasingly cross-disciplinary nature of nanoscientific research, Alivisatos's group at Berkeley (Bruchez *et al* 1998) and Chan and Nie at Indiana University (Chan and Nie 1998) have exploited the narrow luminescence spectra of semiconductor nanocrystals for fluorescence studies of biological cells. Bruchez *et al* (1998) functionalized the surface of CdS–CdSe nanocrystals with tri-methoxysilylpropyl urea and acetate groups which promoted strong binding of the nanocrystals with the nuclei of fibroblast cells (see figure 37(c)). Chan and Nie (1998) labelled ZnS–CdSe nanocrystals with the protein transferrin (via mercaptoacetic acid molecule inkers). These nanocrystal bioconjugates were subsequently transported into cultured living cells and imaged using an epifluorescence microscope (figures 37(a) and 37(b)). Furthermore, Chan and Nie have investigated the efficacy of nanocrystals for immunoassay, demonstrating that CdS–CdSe nanocrystals functionalized with immunomolecules could recognize specific antibodies and antigens. Both groups stress the distinct advantages of nanocrystal bioconjugates over organic dyes (for example, rhodamine)—namely, much greater brightness, much greater stability with respect to photobleaching (see figure 37(d)) and much narrower spectral linewidths.

## 6. Magnetic nanoclusters

It is difficult to overestimate the technological benefits associated with the synthesis of ever-smaller nanoscale magnetic clusters and finer-grained nanostructured magnetic materials: over

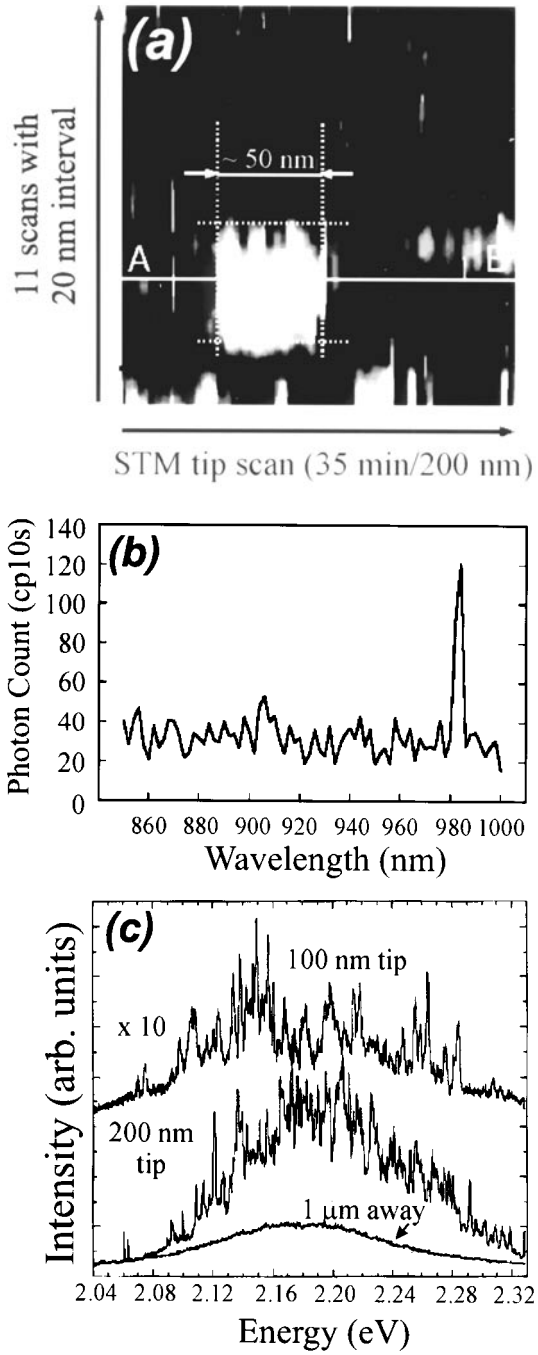


**Figure 35.** (a) Light emission from a single (MBE-grown) InAs nanocrystal excited by electron injection from the tip of an STM (bias voltage $-10$ V, current: 1 $\mu$A). (b) The spectrum of STM-induced light from the nanocrystal (Yamanaka *et al* 1998). (c) Scanning near-field optical microscope spectra from MBE-grown CdSe nanocrystals. The upper spectrum was taken with a 100 nm radius-of-curvature tip yielding a very high spatial resolution whereas the lower spectra were taken with a 200 nm tip in the near- and far-field regimes (Flack *et al* 1996).

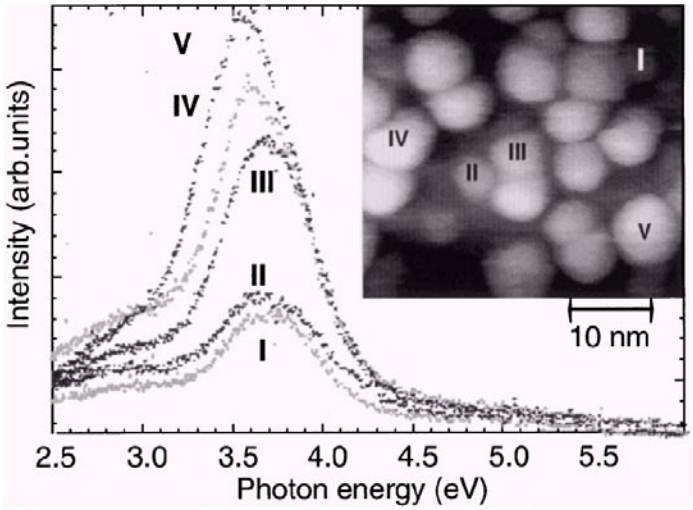


**Figure 36.** STM-induced light emission spectra for Ag nanoclusters on an $Al_2O_3$ substrate. A clear shift in the resonance position is observed as a function of cluster size (Nilius *et al* 2000).

the past five years or so the areal density of magnetic mass storage media has increased at an annual rate of 60%. Paralleling the intense interest associated with the development of alternatives to the top-down approach to semiconductor nanostructure fabrication, the study and exploitation of magnetism at the nanometre scale have been exceptionally active research areas over the past decade. A fundamental driving force in nanomagnetic research is the very close relationship between basic and industrially relevant applied research. This is best exemplified by the relatively short period that separated the discovery of the giant-magnetoresistance effect (Baibich *et al* 1988) and the construction of a prototype device based on that effect (Heim *et al* 1994, Oepen and Kirschner 1999).

*Magnetoelectronics* or *spintronics* (Prinz 1998, Awschalom and Kikkawa 1999)—the combination of low-dimensional/nanoscale semiconductor physics and sub-micron-scale magnetism—is a nascent field with vast potential in both fundamental research and device applications. Ohno *et al* (1999), building on previous work involving the synthesis of ferromagnetic semiconductors (Ohno 1998) and the demonstration that optically excited carriers in GaAs retain their spin integrity over very large (100 $\mu$m) distances (Kikkawa and Awschalom 1999), have very recently demonstrated *electrical* spin injection—in the absence of a magnetic field—using a III–V heterostructure. This impressive device concept not only provides a route to the integration of logic and memory functions in a single semiconductor unit but represents a significant step forward in terms of controlled manipulation of coherent electronic spin states in a solid-state device. The latter advance may be of particular significance in the area of quantum computing (Imamoglu *et al* 1999). (See DiVincenzo and Loss (1999) for a recent review of quantum computing.)

A novel alternative to the spintronic device architectures that are based on a combination of conventional semiconductors and magnetic materials has been put forward by Cowburn and Welland (2000). They have fabricated quantum cellular automata (QCA) networks that are based *solely* on the classical magnetostatic interactions between neighbouring nanoscale magnetic islands. The advantages of this device concept, as compared to other QCA networks which are based on single-electron devices (Amlani *et al* 1999, Andres *et al* 1996b), is that the magnetic dots do not have to be made ultrasmall ($\sim$2 nm) to enable room temperature

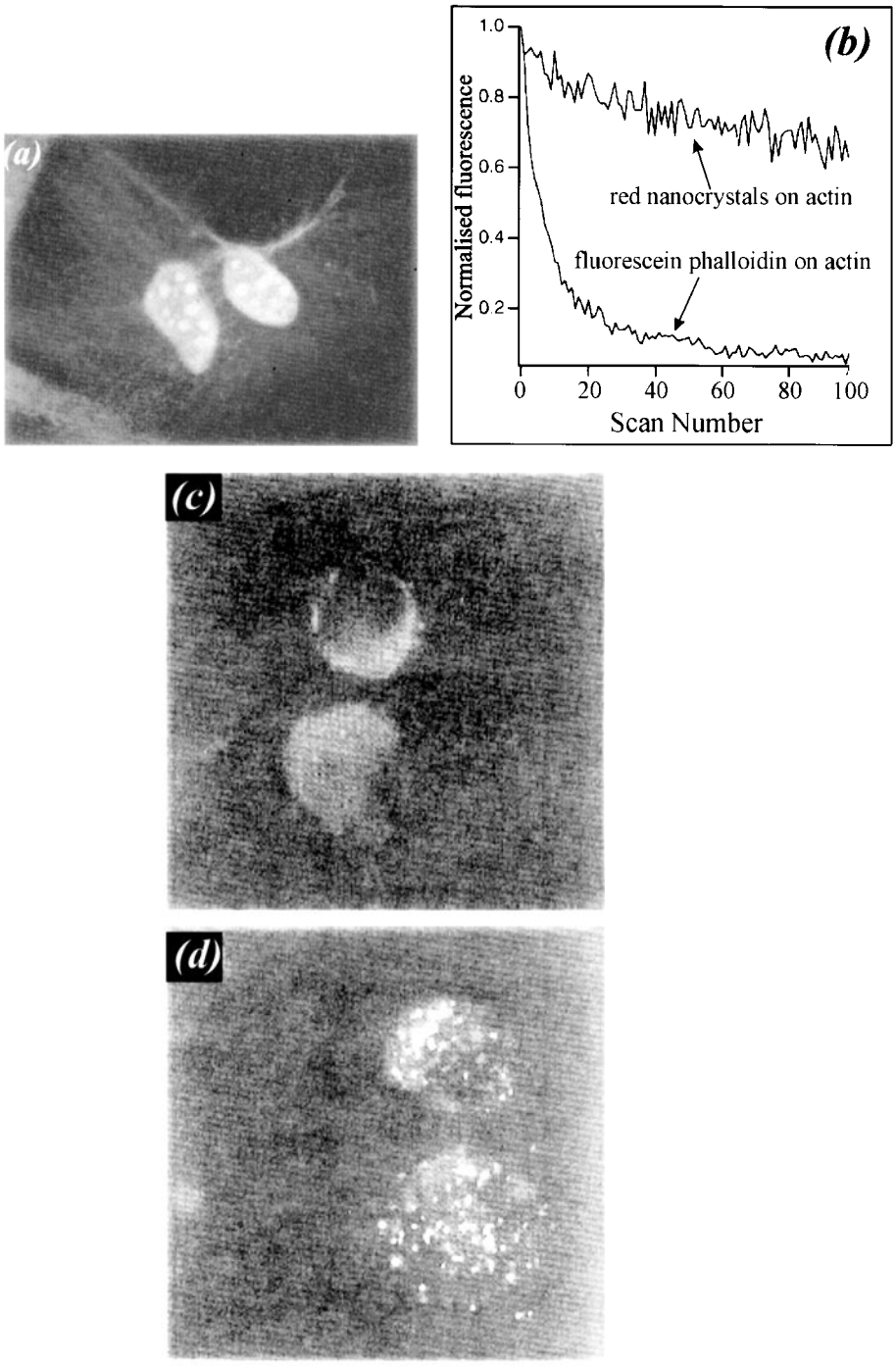


**Figure 37.** (a) Fluorescence from CdS–CdSe nanocrystals bound to cell nuclei via functional trimethoxysilylpropyl urea and acetate groups. (b) Comparison of photostability of fluorescein-phalloidin-labelled and nanocrystal-labelled actin fibres. (c), (d) Luminescence images of cultured HeLa cells that were incubated with mercapto–nanocrystal and transferrin–nanocrystal complexes respectively. Only for the latter are nanocrystals observed within the cell. ((a), (b) Bruchez *et al* (1998); (c), (d) Chan and Nie (1998).)

operation—the sizes of the (Supermalloy) islands used in the study were ∼100 nm. Logic states in the network were determined by the direction of magnetization of the single-domain islands and were set and read out using pulsed magnetic fields and magneto-optics respectively.

Although a comprehensive discussion of spintronics and nanoscale magnetism is outside the scope of this review, in the following sections we will briefly describe some of the key advances in our understanding of nanoscale magnetic properties and the synthesis of nanoscale magnetic clusters that have occurred over the last decade. The reader is referred to a number of recent reviews for more detailed information: Henry and Laughlin (2000), Grünberg (2000), Awschalom and Kikkawa (1999), Prinz (1999), Schuller *et al* (1999), Kodama (1999), Awschalom and DiVincenzo (1995) and Shi *et al* (1996).

### *6.1. Spin ordering in magnetic nanoparticles: superparamagnetism and the Stoner–Wohlfarth and Néel–Brown models*

Below a certain critical diameter, $d_{crit}$, given by $\sim 2(\sqrt{A_{ex}})/M_s$ (where $A_{ex}$ is the exchange constant and $M_s$ is the magnetic moment per unit volume; Frei *et al* 1957), a magnetic nanoparticle cannot support more than one domain. (The critical diameter generally falls in the 10–100 nm range; Kodama (1999).) In a single-domain cluster the atomic magnetic moments are coupled via exchange interactions to form a large net cluster moment—the cluster is termed a *superparamagnet*. For a given superparamagnetic nanocrystal there are rotational barriers to spin alignment arising from magnetocrystalline, magnetoelastic and shape anisotropies. The magnetic anisotropy energy for a uniaxial particle is generally written as

$$E(\theta) = -KV\cos^2\theta \tag{7}$$

where $K$ is the magnetic anisotropy constant, $V$ the volume of the particle and $\theta$ the angle between the magnetization vector and an easy direction of magnetization.

Figure 38 is a schematic illustration of the magnetic energy of an ellipsoidal superparamagnetic particle in the absence of an external magnetic field. This illustration summarizes the key concepts underlying both the Stoner–Wohlfarth (1948) and Néel–Brown (Néel 1949, Brown 1963) models of the magnetic dynamics of small magnetic particles. The ellipsoidal

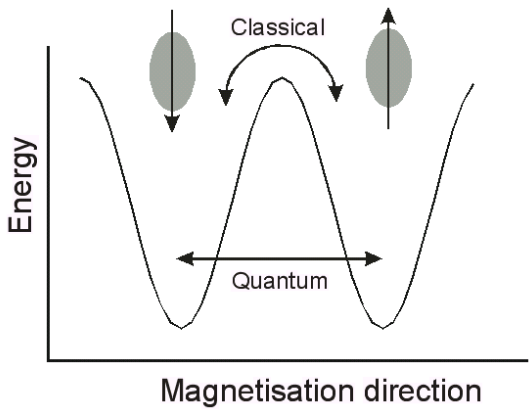


**Figure 38.** A simple schematic illustration of the energy of a magnetic nanoparticle versus the magnetization direction. There are two equivalent energy minima related to the 'spin-up' and 'spin-down' states of the cluster. The spin state can flip between these two minima either via a classical, barrier-surmounting path or via quantum mechanical tunnelling. (Adapted from Gider *et al* (1995).)

magnetic nanoparticle sketched in figure 36 has two stable states—one with its magnetization parallel to its easy axis and the other with the magnetization antiparallel. Stoner and Wohlfarth proposed that as the external magnetic field is varied, one of the states will become unstable with respect to the other and the total spin of the particle may flip. In an extension of this model, Néel and Brown proposed that the particle could overcome the barrier between the two spin orientations through thermal excitation. The frequency of thermally activated reversals is given by the Arrhenius relationship:

$$v = v_0 \exp(-\Delta E/kT) \tag{8}$$

where $v_0$ is the attempt frequency and $\Delta E$ is the barrier separating the two spin states (magnetic anisotropy energy). As the magnetic anisotropy energy scales with particle volume (equation (7)), at any given temperature there is a critical particle size below which thermal energy fluctuations are sufficient for demagnetization (and thus it is impossible to store data as the state of a magnetic bit) or, alternatively, for a particular cluster size there is a temperature limit (the *blocking temperature)* which must be reached to freeze out thermally activated hopping between spin states. Interestingly, the colloidally synthesized Co nanoparticles shown in figure 20 (synthesized by Petit *et al* 1999b) exhibit a blocking temperature of 63 K when the clusters are arranged in a 2D network, but this decreases to 58 K for isolated particles. Similarly, differences in the hysteresis loop behaviour for Co nanoparticles dispersed in pyridine and those forming a 2D lattice on a graphite surface have been attributed to a 'collective effect due to the 2D organization' (Petit *et al* 1999b)

As highlighted by Kodama (1999), although superparamagnetic dynamics is understood at a phenomenological level, the physical processes underlying thermally excited spin reversal have been the subject of some discussion. The ability to probe the dynamics of *individual* particles using magnetic force microscopy (MFM) (e.g. Shi *et al* 1996, Wirth *et al* 1999), high-sensitivity superconducting quantum interference device (SQUID) magnetometry (e.g. Wernsdorfer *et al* 1996, 1997a) and Lorentz microscopy (e.g. Majetich and Jin 1999, Salling *et al* 1994) has prompted recent debate over the validity of the classical Néel–Brown and Stoner–Wohlfarth models and the conditions under which those mechanisms are superseded by quantum mechanical tunnelling of the spin states of superparamagnetic clusters (see below).

A variety of investigations of single-particle dynamics (see Kodama (1999) for a discussion) strongly suggested that the Néel–Brown model was insufficient to describe the behaviour of single-domain magnetic nanoclusters (Ledermann *et al* 1994, Chang and Zhu 1994, Wernsdorfer *et al* 1995). The role of defects and, particularly, surfaces in determining the spin state and dynamics of the clusters has been cited as a key factor underlying disagreement with the Néel–Brown model. A large number of recent studies of ferrite and magnetic oxide-covered Fe single-domain nanoparticles (Kodama *et al* 1996, 1997, Kodama 1999, Bellouard *et al* 1996) highlight the contribution of surface spin disorder. In nominally single-domain particles, exchange coupling between the bulk of the cluster and the surface can lead to a much more complex spin arrangement and, subsequently, richer dynamics than that predicted for an ideal superparamagnetic particle. The very significant effects that surface structure and surface electronic properties have on the magnetic properties of nanoparticles are described in de Heer (1993), Kodama (1999) and Binns *et al* (1999).

However, in more recent work Wernsdorfer *et al* (1997c, d) have found that the magnetization reversal of both Co and barium ferrite nanoparticles as a function of time can be described by thermal activation over an energy barrier, i.e. their results strongly support the Néel–Brown model (figure 39). This group stresses the critical importance of sample quality—for particles with antiferromagnetic components (as would result from oxidation) they observed clear disagreement with Néel–Brown theory (Wernsdorfer *et al* 1997b). For temperatures lower

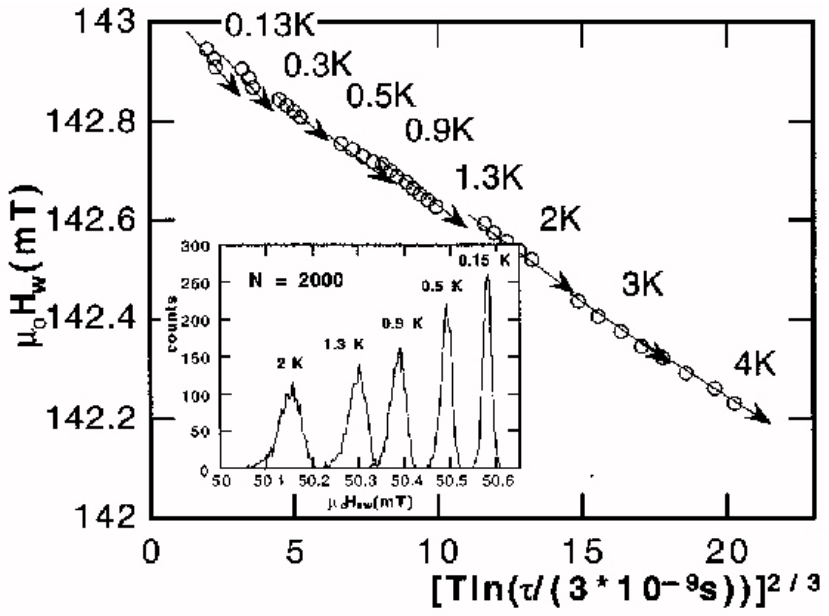


**Figure 39.** Magnetization switching times for a 20 nm Co particle. For a range of temperatures (0.1 s $< \tau(H_w, T) <$ 60 s), the magnetic field is increased to a value $H_w$ (the waiting field) and the time taken for magnetization to switch is measured (using a micro-bridge dc SQUID). Each arrow is a guide to the eye for data obtained at one temperature and a number of waiting fields. The field and temperature dependence of $\tau$ follow the following Néel–Brown relationship: $\tau(T, H) = \tau_0 \exp(E(H)/kT)$. The inset is a plot of the temperature dependence of the switching field distribution.

than ∼0.4 K, departures from the Néel model were observed for the barium ferrite particle. These differences were described in terms of quantum tunnelling of the magnetization of the particle—a topic that is covered in the following section.

### *6.2. Biological magnets and quantum mechanical tunnelling of spin states*

In section 3 Vollmer–Weber growth and colloidal synthesis of magnetic clusters were discussed. A number of alternative techniques have been used to fabricate nanoscale magnetic particles including advanced lithographic patterning (Chou *et al* 1996, Xu *et al* 1995, O'Barr *et al* 1997), STM in combination with chemical vapour deposition (Kent *et al* 1993, Wirth *et al* 1999) and metal deposition on colloidal (silica nanosphere) crystal surfaces (Li *et al* 2000). However, as with the hybrid bio-inorganic systems discussed in previous sections, there has been a great deal of interest in exploiting *naturally* occurring nanostructures as prototypical magnetic systems. As such, ferritin—an iron- ($Fe^{3+}$-) storing protein which is found in most animals (including humans) has attracted a considerable amount of attention (Awschalom and DiVincenzo 1995, Awschalom *et al* 1992b). (The use of biological systems to control the *ordering* of nanometre-scale magnets has also been explored (Field *et al* 1998).)

In ferritin, a protein shell approximately 12.5 nm in diameter encapsulates an iron nanoparticle. Synthetic biochemical techniques have been employed to load the empty protein shell with anywhere from a few to a few thousand ferric ions and, in addition, to encapsulate both antiferromagnetic and ferromagnetic species within the shell (Awschalom and DiVincenzo 1995). Figure 40(a) is a plot of the blocking temperature for artificial antiferromagnetic proteins

as a function of the amount of iron loading. A linear dependence of blocking temperature on particle size, as predicted by Néel–Brown theory, is observed. However, as the iron loading goes to zero (i.e. the particle size approaches the atomic limit), the blocking temperature of ferritin ceases to obey the Néel–Brown model and more exotic mechanisms of spin reversal need to be invoked.

Two key results of a theoretical study of the rate of magnetization switching in nanoscale ferromagnetic particles (Chudnovsky and Gunther 1988) were:

(i) at temperatures below a certain critical point, $T^*$, magnetic relaxation will become independent of temperature as the spin dynamics in that regime is determined by quantum mechanical tunnelling of the (collective) spin state of the nanocluster and
(ii) the tunnelling rate falls off exponentially with increased particle size.

(As pointed out by Awschalom and DiVincenzo (1995), it is somewhat difficult to directly relate conventional single-particle tunnelling to the collective process that occurs in tunnelling of magnetization. This problem is treated in depth by Chudnovsky and Gunther (1988).) Wernsdorfer *et al* (1997d) found that their magnetization measurements of a single barium ferrite particle at temperatures in the 0.13 K to 0.3 K range were best described by a tunnelling model.

Returning to the discussion of ferritin, at temperatures below 200 mK the coherent tunnelling of magnetization back and forth between two potential wells produces a resonance peak in magnetic susceptibility and noise spectra (figure 40(b)) (Awschalom *et al* 1992a). The exponential shift of the resonance as a function of nanoparticle volume agrees with the predictions of the theory put forward by Chudnovsky and Gunther (1988).

## 7. Carbon-based nanomaterials

Carbon, a group IV element like Si, is associated with a rich and diverse chemistry. However, despite this, it is the latter element that is at the core of the microelectronics and computing industries. This is largely because, prior to the discovery of fullerenes, there were only two known crystalline forms of solid carbon: diamond, whose band gap is $\sim$6 eV, and graphite, a semimetal. The structural and electronic properties of both crystals to a large extent precluded their use in advanced electronic applications (although there are exceptions, particularly for high-temperature applications). With the discovery (Kroto *et al* 1985) and then synthesis of macroscopic quantities (Krätschmer *et al* 1990) of fullerenes came the possibility of complementing (or, in the long term, perhaps even superseding) silicon-based devices with carbon-based electronics. Recent work—particularly with carbon nanotubes—has produced impressive results illustrating the flexibility of fullerene-based systems. Progress has been rapid—from electrical measurements on single molecules (Tans *et al* 1997, Porath and Millo 1997) just three years ago, rectifying junctions (Yao *et al* 1999), a single-molecule transistor (Tans *et al* 1998b) and coherent spin transport (Tsukagoshi *et al* 1999) in nanotubes have since been demonstrated. A common thread running through these—and the related experiments to be discussed below—is the use of fullerenes as prototypical nanoscale systems to probe fundamental low-dimensional physics. (Indeed, $C_{60}$ has recently been used as a powerful probe of fundamental quantum mechanics. It is the most massive object for which de Broglie interference has been observed (Arndt *et al* 1999).)

As a considerable number of texts and reviews covering the physics and chemistry of $C_{60}$, fullerenes and nanotubes have been published in recent years including a comprehensive overview by Dresselhaus *et al* (1996), the intent in the following is to complement—rather than repeat a discussion of—the material covered in those reviews. In particular we forego a

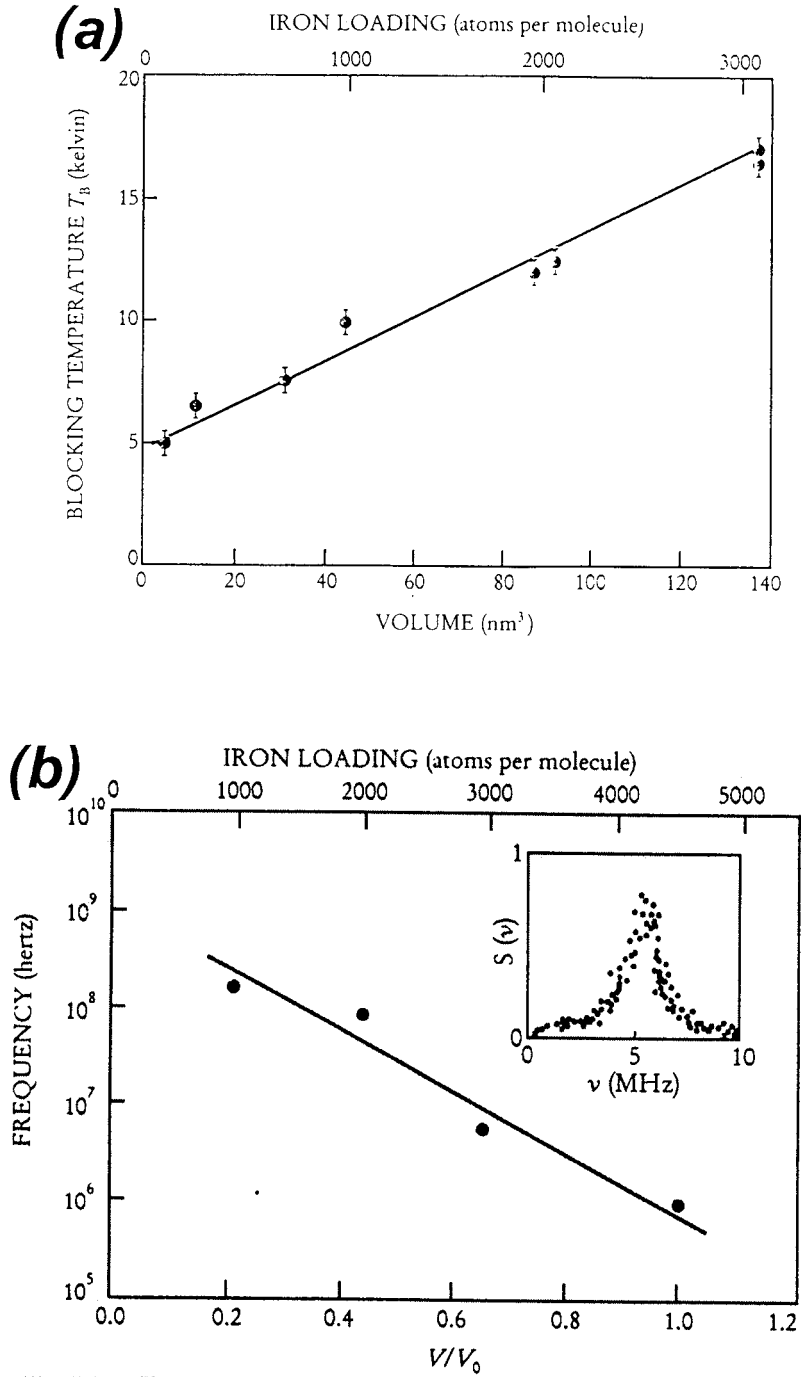


**Figure 40.** (a) The dependence of the blocking temperature $T_B$ on the mean magnetic particle size in artificially synthesized ferritin molecules. (b) The dependence of the magnetic noise resonance frequency (measured using a dc SQUID magnetometer) for ferritin on the particle size. The resonance frequency decreases exponentially with particle size, $V$, as predicted by quantum mechanical calculations. The inset is a typical noise resonance curve for a particle with an Fe loading of 3000 at 24.3 mK (Gider *et al* 1995, Awschalom and DiVincenzo 1995).

discussion of exohedral doping (for example, alkali and alkaline-earth metal intercalation) in fullerenes as this topic has been covered extensively in a number of recent reviews (Rosseinsky 1998, Fischer 1997, Dresselhaus *et al* 1996, Weaver and Poirier 1994).

### *7.1. Fullerenes*

Buckminsterfullerene ($C_{60}$) is, from a number of perspectives, a molecule almost 'custom built' for nanoscience. Discovered in 1985 by Kroto, Smalley and Heath (Kroto *et al* 1985) (the discovery led to the award of the Nobel Prize in Chemistry in 1996), $C_{60}$ is approximately 1 nm in diameter (the cage diameter is 0.71 nm; the intermolecular spacing in fullerite, the bulk crystal, is 1.004 nm (Dresselhaus *et al* 1996)), readily synthesized in large (i.e. gram) quantities (Krätschmer *et al* 1990) and—of key significance—its physical and chemical properties may be tuned via the addition of a range of elemental and molecular species either to the fullerene lattice, to the fullerene cage or *within* the cage.

In the following sections the fundamental structural, physical and chemical properties of a broad and representative subset of molecules from the fullerene family will be discussed. Particular emphasis is placed on electronic structure and the modification of electronic structure promoted via structural and chemical changes to the fullerene cage (through substitution or insertion of chemical species other than C). The focus on electronic structure is motivated by the central role that it plays in determining electrical transport, optical and chemical properties which in turn underlie a range of potentially technologically important phenomena including magnetoresistance and superconductivity, photoconductivity, crystal growth, surface passivation and electrochemistry.

*7.1.1. Geometric and electronic structure of the $C_{60}$ molecule.* Figure 41(b) is a room temperature nuclear magnetic resonance (NMR) spectrum for $C_{60}$ which clearly consists of a single sharp peak—a result that conclusively demonstrated that the truncated icosahedral structure originally proposed by Kroto *et al* (1985) and shown in figure 41(a) was correct. In figure 41(a) all C sites are equivalent—hence the single NMR line—with each atom bonded to three other atoms in an $sp^2$-related bonding geometry. (The bonding deviates somewhat from pure $sp^2$ character (towards $sp^3$ hybridization) due to the cage curvature.) The dark- and light-shaded lines in figure 41(b) represent double and single C–C bonds with bond lengths of 0.140 nm and 0.146 nm respectively (Taylor *et al* 1990, Johnson *et al* 1990, Tycko *et al* 1991, Johnson *et al* 1992a, b). Every pentagon in the cage structure is surrounded by five hexagons, therefore satisfying the Euler theorem, otherwise known as the isolated pentagon rule (Kroto 1987, Schmalz *et al* 1988). Note that the next largest fullerene to satisfy this rule is $C_{70}$.

The truncated icosahedron structure shown in figure 41(a) has 20 hexagonal faces, 12 pentagonal faces, 90 edges and 60 vertices (a C atom is found at each vertex). The icosahedral point group $I_h$ describing the symmetry operations possible for $C_{60}$ represents one of the highest degrees of symmetry attainable in nature. It comprises 120 symmetry operations, arising from: the identity operator, 12 fivefold rotations going through the centre of each of the pentagonal faces (i.e. about a $C_5$ axis), 20 threefold rotations going through the centre of each of the hexagonal faces (about a $C_3$ axis), 30 twofold rotations about the centre of a side of a hexagonal face (about a $C_2$ axis) and composites of the inversion operation with each of these.

Dresselhaus *et al* (1996) discuss in some depth the symmetry of the vibrational modes of $C_{60}$. Here we simply note that of the 174 vibrational degrees of freedom of the $C_{60}$ molecule, the high level of degeneracy imposed by icosahedral symmetry reduces the number of energetically distinct modes to 46. Of these, only four are infrared (IR) active and ten Raman active.

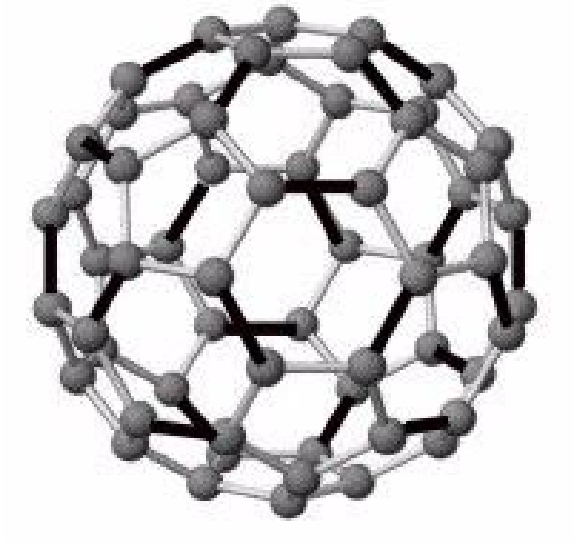

(a)

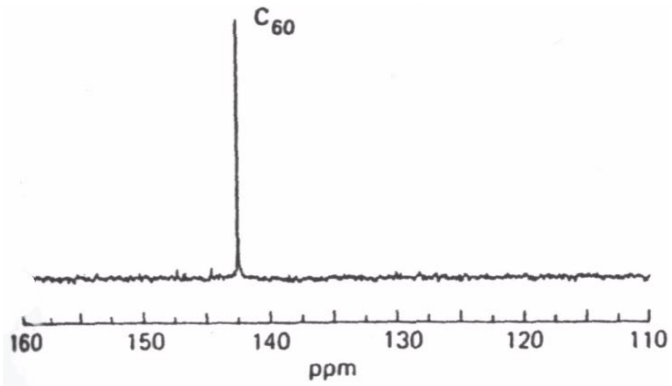


(b)

**Figure 41.** (a) A schematic diagram of the structure of $C_{60}$. Black lines represent double bonds, lighter lines single bonds. (Adapted from an image available at the Sussex Fullerene Group's Fullerene Gallery website: http://www.sussex.ac.uk/Users/kroto/fullgallery.html). (b) A C NMR spectrum from $C_{60}$—the presence of only one line conclusively shows that all C atoms adopt the same bonding geometry, as dictated by the icosahedral symmetry shown in (a). (Figure taken from Johnson *et al* (1992a, b).)

However, a large number of the IR- and Raman-silent modes may be probed with techniques such as inelastic neutron scattering, electron energy-loss spectroscopy and photoluminescence which are not subject to the same selection rules.

Turning to the electronic structure of $C_{60}$, of a total of 240 valence electrons, 180 are involved in relatively deep-lying $\sigma$-bonding energy levels (i.e. energy levels lying well below the Fermi level) with the electronic properties of the molecule primarily determined by the remaining 60 electrons involved in $\pi$-bonds. Importantly, due to the near-spherical shape of a truncated icosahedron, the electronic eigenstates may be considered in terms of spherical

harmonics and classified by angular momentum quantum numbers (Saito and Oshiyama 1991, Oshiyama *et al* 1992, Weaver *et al* 1991). A total of 50 (i.e. 2 + 6 + 10 + 14 + 18; see figure 42) electrons may be accommodated in angular momentum states with $l = 0$ to 4, leaving ten electrons to fill the $l = 5$ orbital angular momentum state. By reducing the symmetry from spherical to icosahedral (the symmetry reduction is treated in a perturbative fashion), the $l = 5$ state splits and the ten electrons are found to occupy a fivefold-degenerate (excluding spin degeneracy) level of $h_{1u}$ symmetry. This is the highest occupied molecular orbital (HOMO) in $C_{60}$. The lowest unoccupied molecular orbital (LUMO) is also derived from the $l = 5$ angular momentum state but has $t_{1u}$ symmetry and is threefold degenerate.

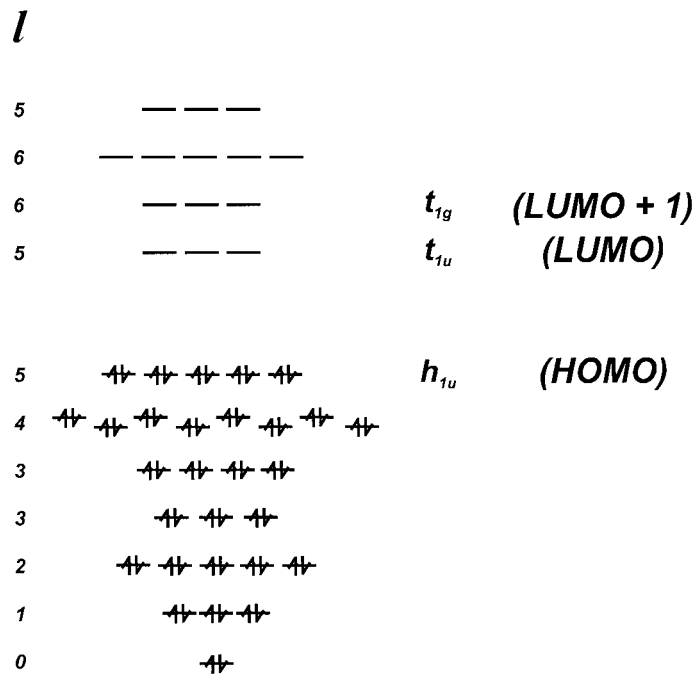


**Figure 42.** A schematic diagram of the molecular orbital (MO) scheme for the 60 $\pi$-electrons in $C_{60}$. Each of the numbers to the left represents the orbital angular quantum number of the spherical harmonic from which a MO is derived. The HOMO is fivefold degenerate whereas the LUMO is threefold degenerate.

*7.1.2. Intermolecular interactions in $C_{60}$ crystals.* The discovery of a simple method of preparing macroscopic amounts of fullerenes (Krätschmer *et al* 1990) established fullerene science as an area of research distinct from cluster physics and chemistry (the original studies of $C_{60}$ (Kroto *et al* 1985) were on clusters synthesized via laser ablation of a graphite target, producing minute quantities) and enabled the production of crystals of buckminsterfullerene. The term for the crystalline form of buckminsterfullerene, coined by Krätschmer *et al*, is *fullerite*.

The cohesive energy of the fullerite crystal (which adopts an fcc structure at room temperature with a lattice constant, $a_0$, of 1.4198 nm) is 1.6 eV/molecule (Saito and Oshiyama 1991), illustrating that relatively weak van der Waals forces underlie intermolecular interactions in the crystal. Similarly, Girifalco (1991) has calculated the $C_{60}$–$C_{60}$ interaction strength as $\sim$0.27 eV. Although the close similarity between photoemission spectra of gas-phase and bulk

$C_{60}$ (see Weaver (1992) and Golden *et al* (1995) for a discussion) is suggestive of a very high degree of molecular character in fullerite, local density approximation (LDA) calculations (Shirley and Louie 1993) predicted a significant dispersion of the HOMO-derived bands ($\sim$0.9 eV), suggesting the formation of delocalized electronic states. The first angle-resolved photoemission studies of fullerite failed to reveal significant dispersion in the HOMO-related bands (Wu *et al* 1992). As has been well documented, individual $C_{60}$ molecules in fullerite spin with rotational correlation times of the order of ps and an activation energy of order tens of meV (Tycko *et al* 1991). It was suggested that one factor contributing to the absence of band dispersion might be that the orientational disorder precluded the formation of extended electronic states (Wu *et al* 1992, Antropov *et al* 1993)

However, Gensterblum *et al* (1993), in higher-resolution angle-resolved photoemission work (facilitated by the choice of a very low photon energy (8.1 eV)), interpreted distinct emission angle-dependent modulations in the line shape of the HOMO-derived feature as arising, at least in part, from filled-state band dispersion. They argued that the dispersive feature was accompanied by vibronic sidebands, accounting for the total HOMO bandwidth of $\sim$1 eV. The choice of very low photon energy, while increasing $k$-resolution, leads to significant problems in the interpretation of the photoemission data. With low photon energies, the photoelectron is excited to a very structured empty density of states and, thus, the photoemission spectra manifest features that arise from the (matrix-element-coupled) joint density of filled *and* empty states. When this was considered (Benning *et al* 1994), dispersion in both filled and empty states was proposed to thoroughly account for the bandwidth of the $C_{60}$ valence features (i.e. the inclusion of vibronic losses was not necessary).

Although the preceding discussion illustrates that—despite significant orientational disorder—delocalized electronic states are supported in the fullerite crystal, it is important to remember that $C_{60}$ still retains a high degree of molecular character. Thus, the bandwidths are narrow and electron correlation effects play a significant role (Weaver 1992, Golden *et al* 1995, Rosseinsky 1998). Of particular importance is the ratio of the intramolecular electronic repulsion energy, $U$, to the bandwidth, $W$. It is possible to determine a value of $U$ for fullerite from a comparison of the C KVV Auger spectrum (where two electrons are ejected from the same molecule) with the self-convolution of the valence band spectrum (where the electrons are ejected from different molecules). Using this approach, an average value of $U$ of 1.4–1.6 eV was determined (Lof *et al* 1992, Merkel *et al* 1993)—appreciably larger than the bandwidth in fullerite. There has consequently been a considerable amount of debate regarding the role that electronic correlation plays in electrical transport in fullerenes (and particularly in exohedrally doped fullerenes) (Lu 1994, Lof *et al* 1992, Brühwiler *et al* 1993, Antropov *et al* 1992, Gunnarsson *et al* 1996).

*7.1.3. Fullerene–surface interactions.* Before moving on to discuss the modification of the electronic structure of fullerenes via substitutional or endohedral doping, we will outline recent work on the interaction of $C_{60}$ with solid surfaces. Fullerene–surface interactions have been the subject of a vast amount of research and only a small amount of that work can be discussed here. The reader is referred to recent and forthcoming reviews for more detailed discussion (Sakurai *et al* 1996, Hunt and Moriarty 2001). Fullerene–surface interactions are not only of fundamental interest—in that, for example, a wealth of information on the chemical bonding properties of the molecule can be derived from adsorption and surface science studies—but play a significant role in the nanometre-scale (STM-based) manipulation of fullerenes described in the introduction and in the potential exploitation of fullerenes as low-dimensional molecular conductors or as the active units in nanoscale electronic devices (Joachim and Gimzewski 1997, Cuberes *et al* 1996, Dunn *et al* 1997)

Figure 43 illustrates the morphological variations observed for fullerene overlayers (including submonolayers) on substrates whose surface free energies span a range of reactivities. On inert surfaces, such as graphite (Hunt and Palmer 1996), the dichalcogenides, e.g. GeS (Gensterblum *et al* 1993, Schwarz *et al* 1995), H- and Ag-passivated Si (figures 43(a) and 43(b) respectively) (Sanvitto *et al* 2000, Dumas *et al* 1996, Upward *et al* 1997b), the substrate–molecule interaction is similar in strength to the intermolecular binding energy in fullerite and, hence, the molecules are effectively physisorbed via van der Waals forces. On these surfaces, the $C_{60}$ films generally grow in a Vollmer–Weber mode (although adsorption on GeS, under certain growth conditions (Schwarz *et al* 1995) is a notable exception (Gensterblum *et al* 1993)), forming islanded overlayers which exhibit the hexagonal symmetry of a fullerite (111) plane with an intermolecular spacing very close to that in solid $C_{60}$. The $C_{60}$/GaAs(110) system also falls within this 'essentially physisorbed' category, although binding energy shifts of the substrate core-level photoemission features betray the contribution of a small amount of charge transfer (Ohno *et al* 1991).

A common feature of $C_{60}$ adsorption on noble-metal surfaces is the strong ionic character of the bonding which arises from a significant amount of charge transfer from the substrate near-Fermi-level surface states to the fullerene $t_{1u}$-derived LUMO. Charge transfer from the substrate has been observed in a range of studies of $C_{60}$ adsorption on: Au (Ohno *et al* 1991, Gimzewski *et al* 1994, Modesti *et al* 1993), Ag (Wertheim and Buchanan 1994, Hoogenboom *et al* 1998, Tjeng *et al* 1997) and Cu (Murray *et al* 1997, Tseu *et al* 1997, Chase *et al* 1992). Quantitative estimates of the degree of charge transfer have been made on the basis of the intensity of the LUMO-derived feature in ultraviolet photoemission (UPS) spectra and on the shift of the 'pentagonal pinch' vibrational mode observed in high-resolution electron energy-loss spectra (Modesti *et al* 1993, Hunt *et al* 1995). Maxwell *et al* (1994) have, however, highlighted that for Au(110), a significant amount of hybridization of the molecular orbitals and substrate surface states takes place in addition to charge transfer.

Although $C_{60}$ diffuses readily on metal substrates, decorating step edges and forming islands (figures 43(c) and 43(d) respectively), the increased adsorbate–substrate interaction is manifest as a higher level of commensurability of the adsorbate overlayer with the reconstructed surface lattice or, more dramatically, as a restructuring of the metal surface upon $C_{60}$ adsorption (Gimzewski *et al* 1994).

There has been considerable debate regarding the nature of the interaction of $C_{60}$ with Si surfaces. The Si(111)($7 \times 7$) surface, due to the presence of partially filled dangling bonds, is (weakly) metallic. It was therefore originally suggested (Wang *et al* 1992, Chen *et al* 1994) that, analogously to the $C_{60}$–noble-metal interactions described above, the fullerene–Si(111) interaction was ionic in character. High-resolution electron energy-loss spectroscopy (HREELS) data apparently supported this charge-transfer model with quantitative estimates of the degree of electron donation to the fullerene LUMO being as high as $3(\pm 1)$ electrons per molecule (Suto *et al* 1997). Photoemission measurements on this system (Moriarty *et al* 1998, Cepek *et al* 1999, Sakamoto *et al* 1998) have since shown that there is negligible electronic occupation of the fullerene LUMO, with the latter studies demonstrating that the bonding is strongly covalent in character (necessitating a complete reinterpretation of HREELS data (Suto *et al* 1997) for this system)—a clear Si–C-related peak is observed in both the core-level and valence band spectra. However, Sakamoto *et al* (1998) have suggested that as few as 27% of the molecules in a $C_{60}$ monolayer on Si(111) are covalently bound, with the rest being physisorbed. This result is rather at odds with recent photoemission measurements by our group. Our data for both the $C_{60}$/Si(111) (Cotier *et al* 2001) and $C_{60}$/Si(100) (Hunt *et al* 2001) systems strongly suggest that the apparent presence of a mixture of chemisorption and physisorption states may arise from an improper calibration of the $C_{60}$ deposition rate in

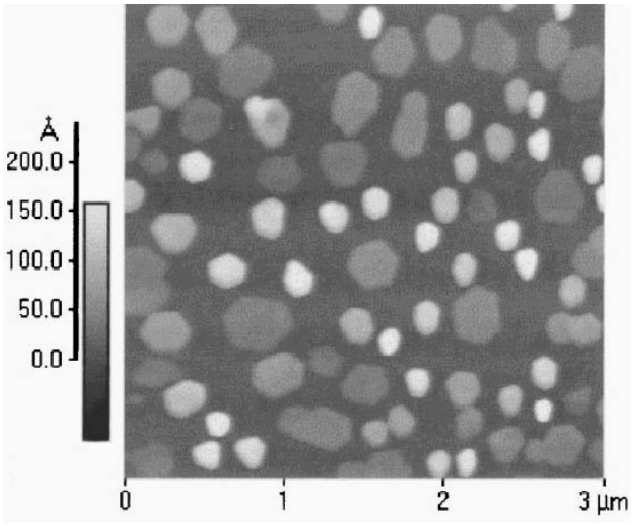


(a)

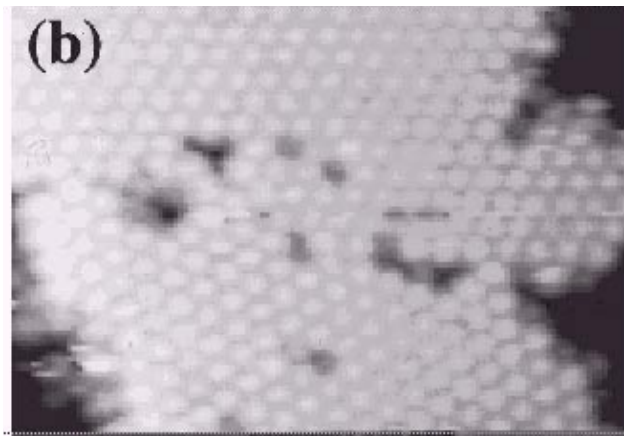


**Figure 43.** $C_{60}$ adsorption on solid surfaces. On low-free-energy hydrogen-passivated Si(100) or Ag-terminated Si(111) ((a), (b) Sanvitto *et al* (2000) and Upward *et al* (1997b) respectively), $C_{60}$ molecules interact weakly with the substrate and readily diffuse to form hexagonally close-packed islands. (c), (d) $C_{60}$ tends to preferentially adsorb at step edges on metal surfaces at low coverages. The molecules adsorbed at step edges then act as seeds for monolayer growth. Both images (c) and (d) are taken from Johansson *et al* (1998) and show submonolayer coverages of $C_{60}$ on Al(111). (e) Much stronger covalent interactions preclude a large amount of fullerene diffusion on silicon surfaces. As a result, $C_{60}$ monolayers on Si(100) exhibit only limited short-range order (Hashizume *et al* 1992) where the molecular spacings are commensurate with the underlying Si lattice. In (e) areas of both c(4 × 4) and c(4 × 3) symmetry are observed. (f), (g) Further evidence that $C_{60}$ is chemisorbed comes from STM molecular manipulation experiments. Attempts to push two $C_{60}$ molecules together with the STM tip in order to reduce the intermolecular separation to close to the van der Waals spacing (expected if the molecules are physisorbed) were unsuccessful. The smallest intermolecular spacing for two molecules adsorbed in the same trough between dimer rows (at submonolayer coverage) is 1.15 nm—three times the underlying Si surface lattice constant (Moriarty *et al* 1998a).

the work reported by Sakamoto *et al* (1998). A similar criticism regarding deposition rate calibration has recently been raised by Pesci *et al* (2000).

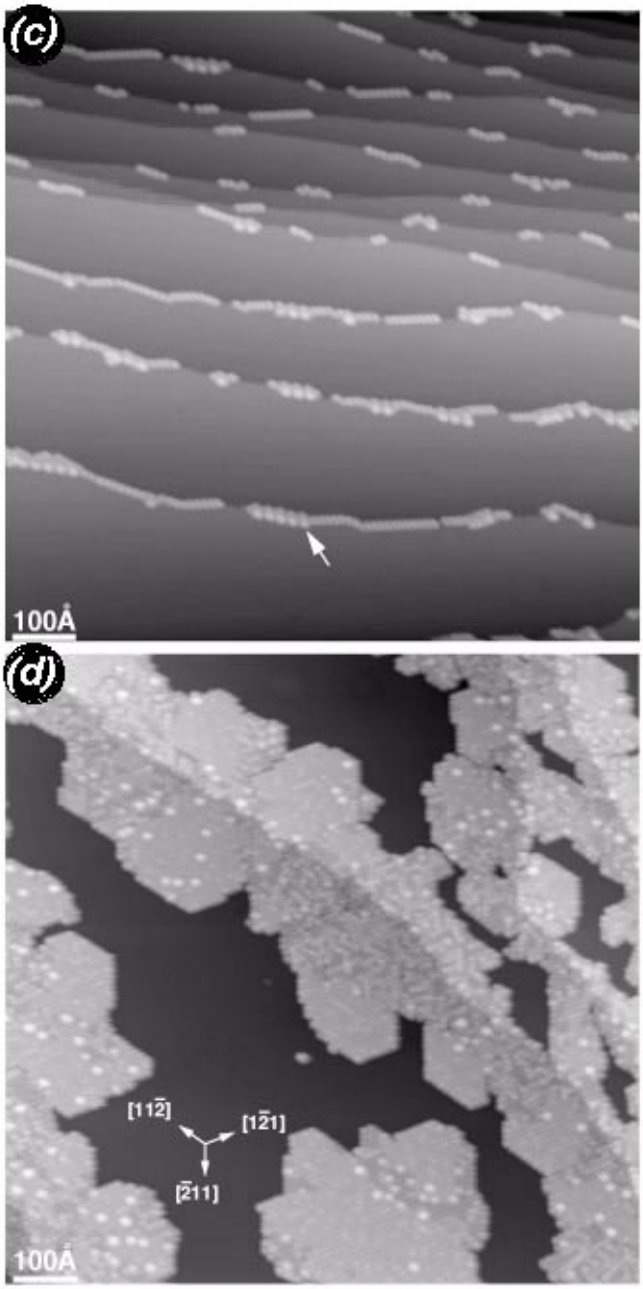


**Figure 43.** (Continued)

Arguments for the physisorption of $C_{60}$ on Si(100) (or, at least, the absence of an appreciable molecule–surface interaction that might outweigh intermolecular interactions) have also been put forward (Chen and Sarid 1995, Klyachko and Chen 1997) on the basis of STM measurements. Again, photoemission measurements (Moriarty *et al* 1998a, De Seta

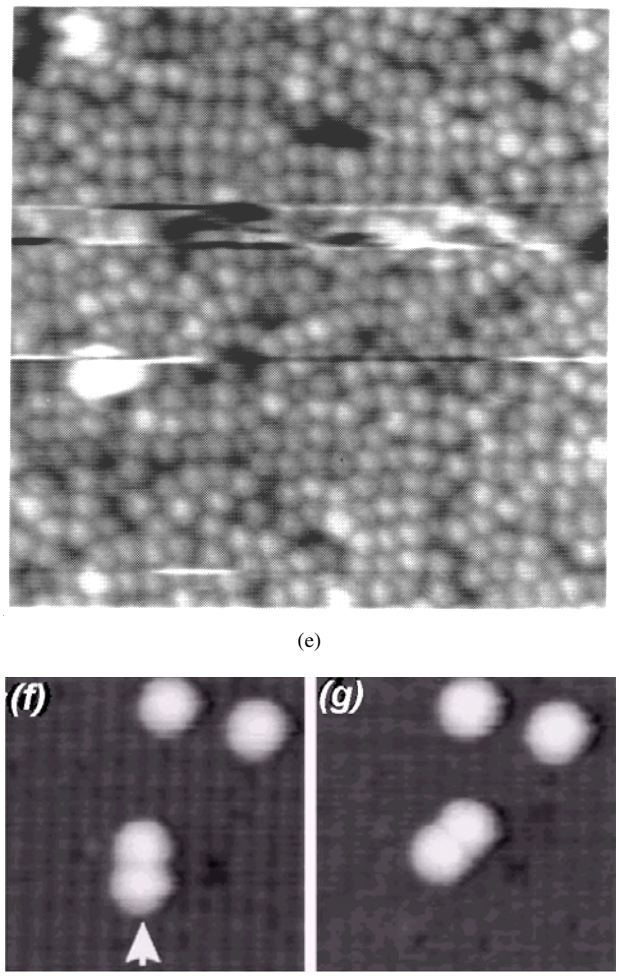


**Figure 43.** (Continued)

*et al* 1999, Sakamoto *et al* 1998) have clearly illustrated that $C_{60}$ is chemisorbed on Si(100)—the work of Sakamoto *et al* (1998) clearly illustrating the presence of a strong Si–C-related signal in valence band spectra. The commensurability of $C_{60}$ overlayers on Si(100) with the substrate lattice (see figure 43(e)) and researchers' inability, in STM-based molecular manipulation experiments, to reduce the separation of two $C_{60}$ molecules to less than 1.15 nm (this figure is substantially greater than the 1.004 nm spacing in fullerite, but represents $3a$ where $a$ is the lattice constant of the (unreconstructed) Si(100) surface), figure 43(f ), provide strong support for chemisorption models.

One argument that has been put forward in support of $C_{60}$ physisorption on Si(100) is the relative ease with which $C_{60}$ may be moved on this surface using an STM tip (Chen and Sarid 1995, Hersam *et al* 2000). However, it is not simply the magnitude of the $C_{60}$–surface bond energy which will determine the ease with which a molecule may be manipulated. Rather, the ability to initiate fullerene motion will depend critically on the potential energy surface that a fullerene has to traverse as it is pushed (in a particular direction) by the tip. The very significant differences in the atomic structure of the Si(111)(7 × 7) and Si(100)(2 × 1) reconstructions

are likely to lead to rather large differences in the magnitudes of the diffusion barriers for $C_{60}$ motion on the respective surfaces and, thus, it is somewhat misleading to base a judgment of the adsorption state of the molecule on the ease with which it is moved by the STM tip.

Although a number of groups have carried out scanning tunnelling spectroscopy measurements of adsorbed $C_{60}$ molecules, the most detailed study to date of the tunnelling spectra of individual fullerene molecules was carried out by Porath and Millo (1997). As for the spectroscopic measurements of InAs nanocrystals discussed in section 4, the STS data for isolated $C_{60}$ molecules exhibited rich structure arising from a combination of charging and electronic level effects.

*7.1.4. 'On-ball' and endohedrally doped fullerenes.* Conceptually, perhaps the simplest method of modifying the electronic properties of an individual fullerene molecule is to replace a C atom on the cage with an atom of higher or lower valence. We then have a process which might be considered analogous to the substitutional n- or p-type doping of a conventional inorganic semiconductor. Although this type of substitutional or 'on-ball' doping was theoretically investigated as early as 1992 (Andreoni *et al* 1992) and both $C_{60-n}N_n$ and $C_{60-n}B_n$ heterofullerenes were formed in molecular beam experiments in 1991 (Guo *et al* 1991, Pradeep *et al* 1991), it was not until 1995 that macroscopic quantities of the azafullerene, $C_{59}N$, in a dimerized (i.e. $(C_{59}N)_2$) form were produced via an organic synthesis route (Hummeln *et al* 1995).

The structure of the $(C_{59}N)_2$ dimer is illustrated in figure 44—a weak ($\sim$0.78 eV binding energy (Andreoni *et al* 1992)) C–C bond is formed between the C atoms directly adjacent to the nitrogen atom on each $C_{59}N$ cage. A detailed photoemission and high-energy electron energy-loss spectroscopy study by Pichler *et al* (1997b) was in good agreement with density functional theory (DFT) calculations of the electronic structure of the dimer. As shown in figure 44, although there is a close similarity between the valence electronic structure of $C_{60}$ and $(C_{59}N)_2$, the HOMO for the latter is derived from N orbitals and the interdimer C–C bond and appears as a shoulder at $\sim$1.5 eV in the valence band spectrum. In addition, as expected from the symmetry lifting and degeneracy lifting associated with the introduction of a N atom, the photoemission peaks for $(C_{59}N)_2$ are significantly broader.

Dimerization 'ties up' the free electron on the $C_{59}N$ cage and the dimer is, like $C_{60}$, free of states within the HOMO–LUMO gap. It is possible to sublime azafullerene *monomers* from the $(C_{59}N)_2$ solid and subsequently stabilize the monomeric form via adsorption on a silicon surface; see figure 45 (Butcher *et al* 1999). However, as also shown in figure 44, the strong fullerene–surface interaction saturates the partially filled state on the $C_{59}N$ cage and little difference between the electronic structure or bonding interaction of adsorbed $C_{60}$ and $C_{59}N$ is observed (Butcher *et al* 1999, 2000). In particular, there is no evidence for the N-derived state at $\sim$0.3 eV below the LUMO predicted from theoretical calculations for the monomer (Andreoni *et al* 1992).

A third method of modifying the electronic structure of individual fullerene molecules is to introduce atoms *inside* the cage—producing an exotic state of matter termed an *endohedral* fullerene (Heath *et al* 1985). Just prior to the submission of this review, Shinohara published a comprehensive report on the synthesis and characterization of endohedral metallofullerenes (Shinohara 2000). That report discusses the preparation and structural characterization of endohedral fullerenes in some depth. Here we will concentrate on some of the fundamental questions related to the electronic structure of this class of molecule that have been addressed in recent years.

The focus of the majority of work on the electronic properties of endofullerenes has been the determination of the degree of charge transfer between the atomic orbitals of the

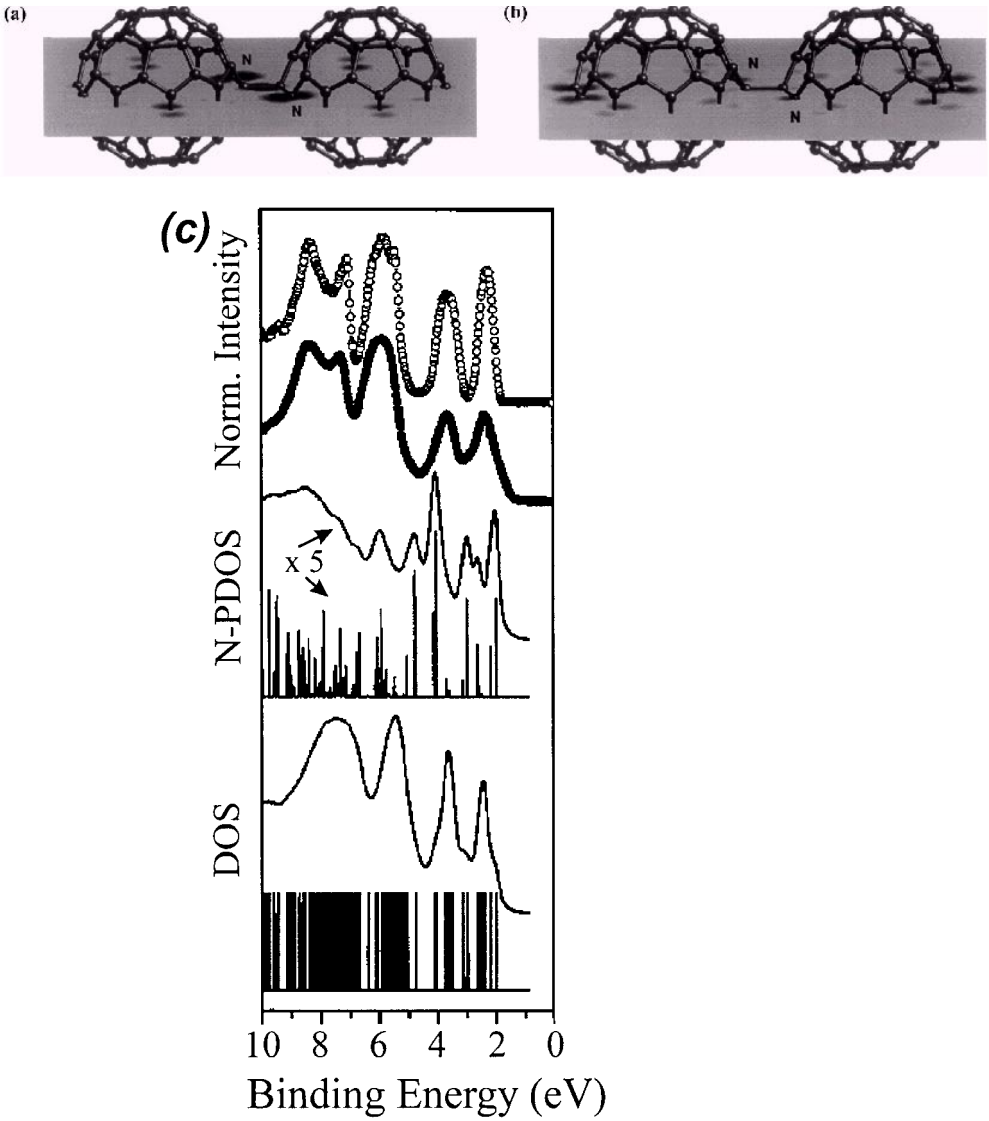


**Figure 44.** The structure of the $(C_{59}N)_2$ dimer. Also shown are the charge density of (a) the HOMO and (b) the LUMO in a plane passing through the N atoms and the intermolecular bond. Note the dominant contributions of the interdimer bond and N (lone-pair-derived) charge density to the HOMO. (c) From top to bottom: the valence band photoemission spectra of $C_{60}$ and $(C_{59}N)_2$, the calculated and broadened N partial density of states (PDOS) and the calculated and broadened total density of states (DOS) for the dimer. Note the shoulder at low binding energies that is present for the valence band spectrum of $(C_{59}N)_2$—this arises from the intermolecular and N charge density shown in (a) and in the calculated PDOS and DOS spectra.

encapsulated metal atom and the molecular orbitals of the fullerene. A related question is whether a picture of a purely ionic interaction is appropriate—or do the metal-atom orbitals hybridize significantly with the cage states? La@$C_{82}$ was one of the first endofullerenes to be synthesized in bulk quantities (Chai *et al* 1991, Bethune *et al* 1993a) and both electron spin-resonance (Johnson *et al* 1992a, b) and photoemission (Poirier *et al* 1994) measurements

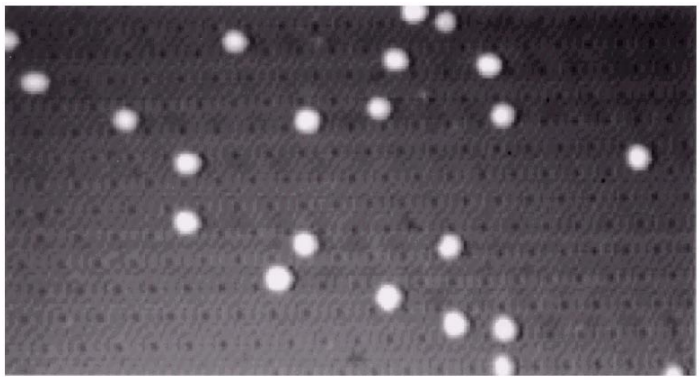

(a)

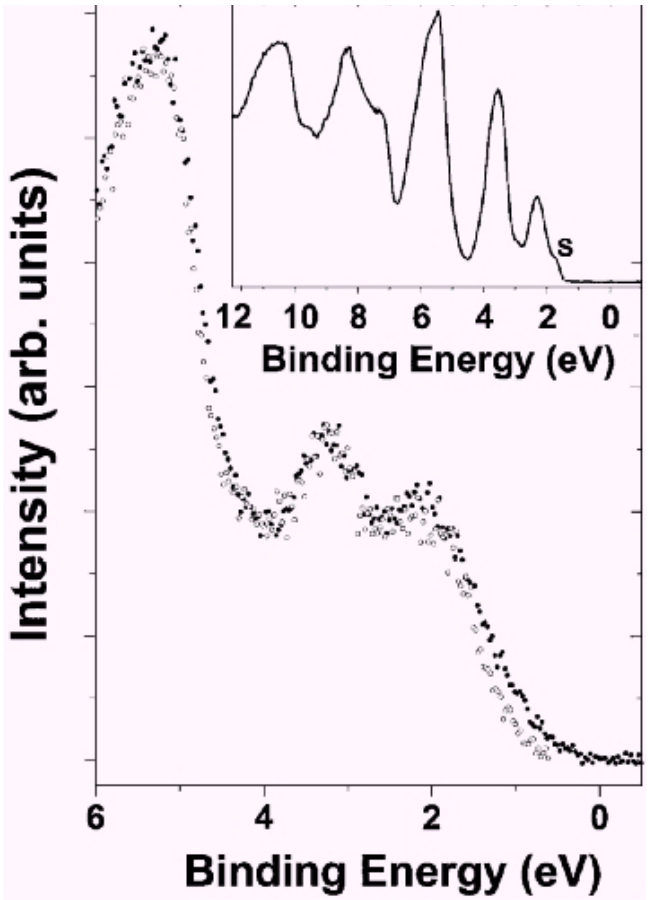


(b)

**Figure 45.** (a) An STM image of $C_{59}N$ monomers adsorbed on Si(111)(7 × 7). (b) There is little difference observed between valence band spectra for 1 ML of $C_{60}$ and 1 ML of $C_{59}N$ on Si(111)(7 × 7). In particular, for the latter we observe no density of states at the Fermi level nor binding energy shift associated with the presence of a partially filled, N-derived state in the fullerene HOMO–LUMO gap. The inset shows the valence band spectrum for a thick (18.5 ML) film of $C_{59}N$ which exhibits the low-binding-energy shoulder associated with dimerization (Butcher *et al* 1999, 2000).

initially provided strong support for a complete charge transfer from the La valence states to the unfilled molecular orbitals of the $C_{82}$ cage, leaving the La atom in a 3+ oxidation state. From an analysis of photoemission data which exploited the differences between the photoionization cross-sections for La 5d and C 2p orbitals, it was argued that the La 5d orbitals did not hybridize with the fullerene cage. A comparison of valence band photoemission spectra for the empty $C_{82}$ cage and La@$C_{82}$ illustrated that, although a feature arising from what was termed a singly occupied molecular orbital (SOMO) appeared above the HOMO-derived peak, it was present at an energy significantly below the Fermi level ($\sim$0.6 eV). Both solid-state crystal-field effects and electron correlation were suggested as possible origins of the splitting of the SOMO band, producing an insulating solid as opposed to the metallic state that one would expect on the basis of a simple one-electron picture.

More recent resonant photoemission measurements by Kessler *et al* (1997) suggest that there is incomplete charge transfer between the La atom and the fullerene molecular orbitals, with $\sim$1/3 of an electronic charge residing in the La 5d orbital. Moreover, the resonant photoemission data provide strong evidence of significant mixing between the La 5d and $C_{82}$ molecular orbitals, ruling out a simple charge-transfer picture and indicating some degree of hybridization between the atomic and molecular orbitals. This contrasts with the Tm@$C_{82}$ system where a complete charge transfer from Tm to the $C_{82}$ cage occurs with no hybridization of the respective atomic and molecular orbitals (Pichler *et al* 1997a). ESR results (Weaver *et al* 1992) indicate that Y in Y@$C_{82}$ similarly exists in a 3+ oxidation state while there is controversy over whether the charge state of Sc in Sc@$C_{82}$ is 3+ or 2+ (Shinohara *et al* 1992, Ruebsam *et al* 1996). However, photoemission data for $Sc_2$@$C_{84}$ clearly illustrate the absence of a half-filled band and, thus, suggest the transfer of an even number of electrons to the fullerene cage.

Although STM can be used to provide data on the absorption sites and packing of submonolayers, monolayers and thin films of endohedral fullerenes (for an overview of this field, see Hashizume and Sakurai 2000) and, in certain cases, indirectly provide information on the nature of endofullerene interactions (Shinohara *et al* 1995), it is not possible to determine the position of the endohedral atom within the cage using STM. Molecular dynamics simulations by Andreoni and Curioni (1996, 1998) predicted a fascinating dynamical intramolecular motion of the La atom.

In an area of nanoscale science that has already produced a wide variety of novel molecules over the past decade, two recently synthesized endohedral fullerenes merit special mention. N@$C_{60}$, which at first glance might be considered an endohedral complement to the $C_{59}N$ molecule is, in fact, remarkably different from its substitutionally doped cousin. Discovered by Almeida Murphy *et al* (1996), N@$C_{60}$ differs dramatically from the endohedral molecules discussed above in that there is negligible interaction between the N atom and the fullerene cage. In addition, the N atom sits at the centre of the $C_{60}$ molecule. The fullerene cage acts as a trap for atomic N, preserving its atomic ground-state configuration—a remarkable result considering the reactive nature of the nitrogen atom. As shown by Pietzak *et al* (1998) via an analysis of the electron paramagnetic resonance signal of the encapsulated N atom, it is possible to use N@$C_{60}$ as a probe of chemical modifications to the $C_{60}$ cage or, as they suggest, as a tracer to monitor fullerene diffusion processes.

Small-band-gap endohedral fullerenes consisting of a $C_{80}$ cage stabilized by an encapsulated metallic nitride cluster have been synthesized by Stevenson *et al* (1999). In addition to the relatively small band gap of $Sc_3N$@$C_{80}$ (0.8 eV), and the different chemical reactivity pathways (as compared to those for $C_{60}$) imposed by the unique structure of the $C_{80}$ cage, a remarkable result of this study is that approximately four $\pi$-electrons are proposed to be withdrawn *from* the fullerene cage via a strong interaction with the central nitrogen atom.

### *7.2. Carbon nanotubes*

Carbon nanotubes—graphitic sheets that are curled up into seamless cylinders—have revolutionized experimental low-dimensional physics and are utilized in a wide variety of state-of-the-art nanoscientific research. Representing arguably the ideal self-assembled quantum wire or, alternatively, a readily 'contactable' single molecule, over the past three to four years there has been intense research activity associated with the exploitation of nanotubes as carbon-based electronic devices.

Nanotubes fall into two broad classes: multi-walled and single walled. The earliest observations (figure 46) were of micron-long multi-walled nanotubes (Iijima 1991) found in the soot that results from fullerene growth via the carbon arc method (Krätschmer *et al* 1990). Each vertical line in the TEM images shown in figure 46 represents a wall of a tube, i.e. a single graphitic sheet. The coaxial arrangement of the tubes is clearly visible. Shortly after the synthesis of multi-walled tubes, Iijima and Ishihashi (1993) and Bethune *et al* (1993b) discovered that transition metals catalysed the growth of single-walled nanotubes (SWNTs) whose diameters could be controllably changed via variations in the growth parameters. While SWNTs typically have diameters ranging from 0.7 nm (the diameter of a $C_{60}$ molecule) to $\sim$3 nm, they can be several microns in length. When this is coupled with their unprecedented high strength and stiffness (the Young's modulus and tensile strength of nanotubes are higher than those of any other material (Mintmire and White 1997, Wong *et al* 1997)) and, as discussed below, their range of electronic behaviour, the motivating factors underlying the recent intense research interest in nanotubes are obvious.

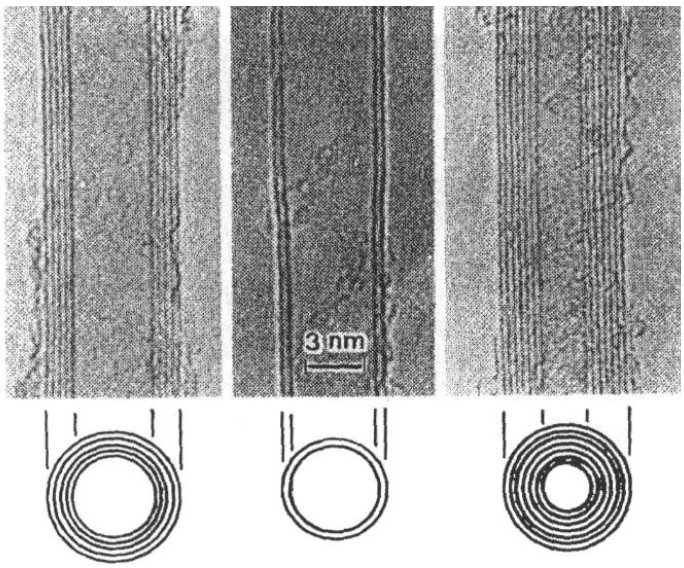


**Figure 46.** TEM images of multi-walled carbon nanotubes (Iijima 1991).

There are a vast number of ways in which a graphite sheet can be rolled up to form a seamless cylinder and hence a wide variety of nanotubes exist. Nanotubes are characterized by their *chiral* (or *wrapping*) vector, $\boldsymbol{c}$ (Dresselhaus *et al* 1996) such that $\boldsymbol{c} = n\boldsymbol{a}_1 + m\boldsymbol{a}_2$ where $\boldsymbol{a}_1$ and $\boldsymbol{a}_2$ are the basis vectors of the graphite (more correctly, graphene) lattice and $m, n$ are integers (figure 47). The chiral vector spans the circumference of the tube formed by joining the dotted lines shown in figure 47. Those tubes with chiral vectors of the form $(n, 0)$ are

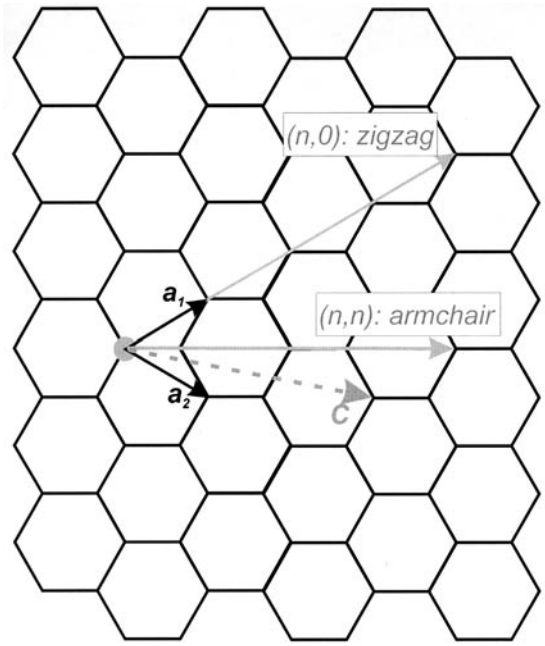


**Figure 47.** The relationship between the graphite lattice basis vectors $\boldsymbol{a}_1$, $\boldsymbol{a}_2$ and the chiral vector $\boldsymbol{c} = n\boldsymbol{a}_1 + m\boldsymbol{a}_2$ used to characterize carbon nanotubes. Two limiting cases are shown: $(n, 0)$ indices are associated with zigzag tubes whereas $(n, n)$ indices are associated with armchair tubes. All other tubes are chiral.

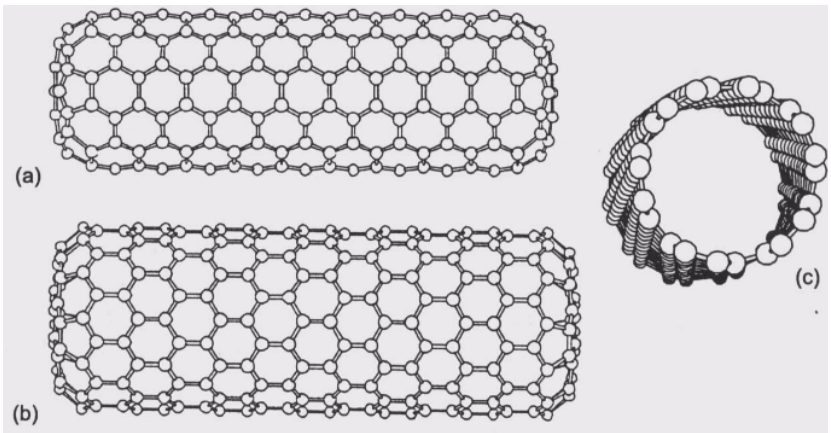


**Figure 48.** Diagrams of the three types of nanotube: (a) armchair, (b) zigzag and (c) chiral. (Reproduced from Tans (1997) with permission.)

termed zigzag tubes (figure 48(a)) whereas when $n = m$ a so-called 'armchair' tube results (figure 48(b)). All other values of $n$ and $m$ produce a chiral tube (figure 48(c)).

Closely following the synthesis of nanotubes came the remarkable theoretical prediction that their electronic properties could be changed between metallic or semiconducting simply by varying the tube diameter or its helicity, i.e. by changing the values of $n$ and $m$ (Hamada *et al* 1992, Saito *et al* 1992, Mintmire *et al* 1992). A key theoretical result is that armchair

nanotubes are metallic, whereas for all other SWNTs, when $n-m = 3l$ ($l$ an integer) the tubes are metallic; otherwise they are semiconducting.

These striking electronic properties can be understood within a tight-binding framework (Hamada *et al* 1992, Saito *et al* 1992, Mintmire *et al* 1992, Dresselhaus *et al* 1996). In the direction along $\boldsymbol{c}$ (i.e. along the circumference of the tube), periodic boundary conditions constrain the values of electron wavevector to those given by

$$\boldsymbol{c}\cdot\boldsymbol{k} = 2\pi q \qquad (q = 1, \ldots, n). \tag{9}$$

Taking the particular example of an armchair nanotube, this can be reduced to

$$k_x n\sqrt{3}a_0 = 2\pi q \tag{10}$$

where $a_0 = (\sqrt{3})0.142$ nm is the graphite lattice constant and $n$ defines the chiral vector for the armchair tube (in this case $\boldsymbol{c} = n(\boldsymbol{a}_1 + \boldsymbol{a}_2)$).

The well-known tight-binding dispersion relation for a 2D graphite sheet (Ashcroft and Mermin 1976) is

$$E_{2D}(k_x, k_y) = \pm\gamma_0\left\{1 + 4\cos\left(\frac{\sqrt{3}k_x a_0}{2}\right)\cos\left(\frac{k_y a_0}{2}\right) + 4\cos^2\left(\frac{k_y a_0}{2}\right)\right\}^{1/2}. \tag{11}$$

$\gamma_0$ is the C–C overlap integral. Substituting into (11) the allowed values of $k_x$ given by (10) yields

$$E^A_{1D}(k_y) = \pm\gamma_0\left\{1 \pm 4\cos\left(\frac{q\pi}{n}\right)\cos\left(\frac{k_y a_0}{2}\right) + 4\cos^2\left(\frac{k_y a_0}{2}\right)\right\}^{1/2} \qquad (-\pi < k_y a_0 < \pi) \tag{12}$$

where the superscript $A$ denotes that (12) is valid only for armchair tubes. It is assumed that the value of the overlap integral for graphite and the nanotube are identical. The 1D dispersion relations given by (12) are shown graphically in figure 49 for the case of a (5, 5) armchair SWNT. There are six dispersion curves for both the valence and conduction bands. In each case, four bands are doubly degenerate (bold continuous lines) and two bands are non-degenerate (thin, dashed lines). Thus ten electronic levels comprise the valence bands and ten comprise the conduction bands, as expected from the fact that there are ten hexagons around the circumference of a (5, 5) nanotube. There are two particularly noteworthy features of the dispersion relations shown in figure 48. First, there is a very high degree of degeneracy at the Brillouin zone boundary. This can be readily understood from the fact that at $k_y a_0 = \pi$, equation (12) reduces to

$$E^A_{1D} = \pm\gamma_0.$$

The second, and more important feature of figure 48 in terms of the electronic properties of armchair nanotubes is that the highest valence band and lowest conduction band are degenerate at $k_y = \pm 2\pi/(3a_0)$ and each cross the Fermi energy ($E = 0$) at that point. This is true of *all* armchair nanotubes—thus, all armchair nanotubes should be metallic.

Note that (10)–(12) represent taking a 1D slice—*in a direction given by equation (7)*—through the 2D graphite band structure. As described in detail by Dresselhaus *et al* (1996), the crossing at $E = 0$ in figure 49 occurs because the corresponding 2D graphite bands cross at the K points (i.e. the corners) of the 2D Brillouin zone. For armchair tubes, there is always an allowed $k$-vector that goes through a K point of the 2D lattice. However, this alignment of the tube wavevector and K points of the graphite Brillouin zone does not automatically occur for zigzag or chiral tubes and hence these can have semiconducting character. Only for $n-m = 3l$ is there an alignment of an allowed $k$-vector and a K point of the 2D Brillouin zone, giving

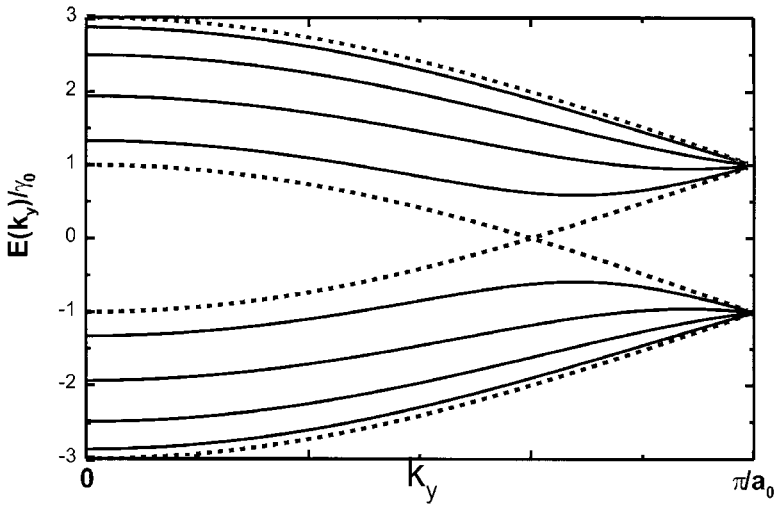


**Figure 49.** The one-dimensional dispersion relation for an armchair (5, 5) nanotube. See the text for details.

rise to metallic behaviour (Dresselhaus 1998, Hamada *et al* 1992, Saito *et al* 1992, Mintmire *et al* 1992).

Although a number of groups carried out conductance measurements on multi-walled tubes using both scanning tunnelling spectroscopy (Dresselhaus *et al* 1996, Zhang and Lieber 1993, Sattler 1995) and two- and four-probe geometries (Ebbesen *et al* 1996, Langer *et al* 1996), conclusive experimental verification of the theoretical predictions outlined above appeared only recently (Wildöer *et al* 1998, Odom *et al* 1998). Figure 50 shows atomically resolved STM images of a range of nanotubes: armchair, zigzag and chiral tubes with different degrees of chirality. By acquiring scanning tunnelling spectra for each of these types of tube it was possible to correlate their structural and electronic properties.

Figure 51(a) shows the tunnelling spectra, acquired at 4 K, for various tubes. Their derivatives ($\mathrm{d}I/\mathrm{d}V$) are shown in figure 51(b). These—apart from the contribution of a bias-dependent transmission term (Feenstra 1993)—provide a good measure of the local density of states of the tubes. Wildöer *et al* observe two distinct 'families' of $\mathrm{d}I/\mathrm{d}V$ spectra for chiral tubes: those with a gap of ∼0.5–0.6 V (spectra 1–4 in figure 50(a)) and those with a much larger apparent gap, 1.7–2.0 V (spectra 5–7). The gap values for the first family of curves are plotted versus the tube diameter in figure 51(c). The solid line is a fit to $E_g = 2\gamma_0 a/d$ where $a$ is the carbon–carbon spacing (0.142 nm) and $d$ the tube diameter. The fit yields a value of 2.7 eV for $\gamma_0$, very close to the 2.5 eV value of the overlap integral in graphite.

The authors argue that the wider gaps in spectra 5–7 in figure 51(b) arise not from a true semiconducting gap but from density-of-states peaks at the band edges associated with the next highest 1D band in a metallic chiral tube. The spacings of these peaks are in good agreement with those expected from the 1D dispersion relations described above. Furthermore, when the interaction with the Au substrate was taken into account it was found that there was indeed a finite DOS near the Fermi level associated with metallic chiral tubes. Furthermore, 1D energy bands exhibit Van Hove singularities where the DOS rises as $1/\sqrt{E}$ (or $1/\sqrt{V}$ for the tunnel spectra) at the band edges. This was first shown theoretically for nanotubes by Saito *et al* (1992) and, as illustrated in figure 51(d), when the normalized conductance, $(\mathrm{d}I/\mathrm{d}V)/(I/V)$, is plotted (which provides a better representation of the DOS), sharp peaks which closely

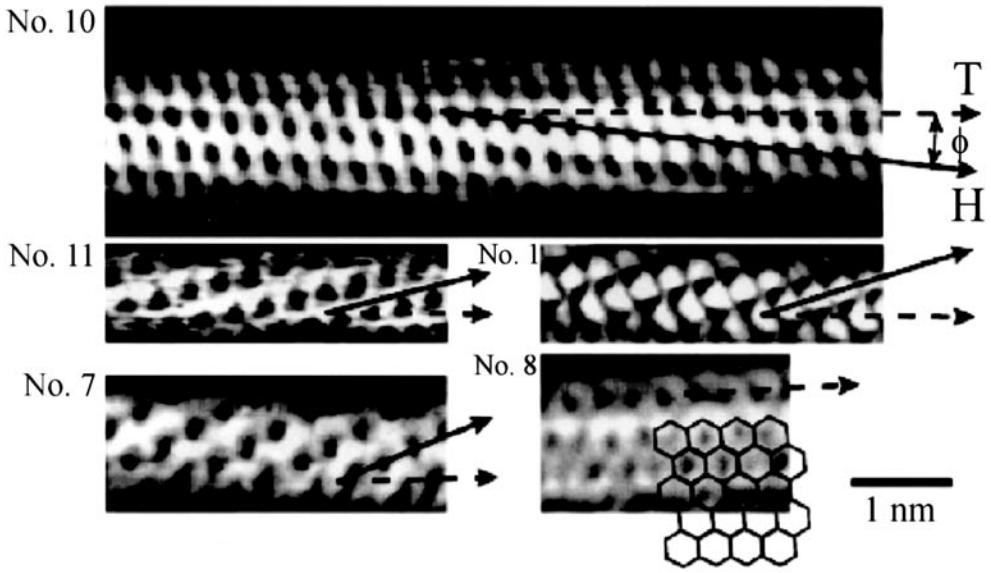


**Figure 50.** Atomically resolved STM images of single-walled carbon nanotubes. Dashed arrows represent the tube axis T and solid arrows indicate the direction of the hexagons comprising the graphene lattice (H). The angle between T and H is the chiral angle. Tubes Nos 10, 11 and 1 are chiral whereas tubes Nos 7 and 8 are of zigzag and armchair type respectively (Wildöer *et al* (1998); figure downloaded from C Dekker's online seminar at http://online.itp.ucsb.edu/online/qhall_c98/dekker/).

resemble broadened versions of those observed in the theoretically calculated DOS spectrum are observed. The broadening was proposed to arise from interactions (orbital hybridization) with the Au substrate.

The Delft group have carried out a variety of fascinating transport measurements on SWNTs. In one of the earliest studies, Tans *et al* (1997) verified that armchair tubes behave as quantum wires with electrical conduction occurring through discrete electron states that are coherent over long distances (>100 nm). Figure 52(a) is an AFM tapping mode image of the device geometry used in the experiments. A SWNT, 1 nm in diameter, bridges two Pt electrodes (spaced by 140 nm) on a $Si/SiO_2$ substrate. The third electrode (upper left section of the AFM image) enables a gate voltage to be applied in order to vary the electrostatic potential of the tube. Clear Coulomb charging effects were observed in the $I(V)$ characteristics of the tube. Measurements of a single conductance ($G = I/V_{bias}$) peak (at low bias voltage, 10 $\mu$V) as a function of temperature (figure 51(b)) were consistent with resonant tunnelling through a discrete energy level of the tube (represented schematically by the solid line in the inset on the left-hand side of figure 52(b)) when the level is aligned with the Fermi energy of the electrodes. As stressed by Tans *et al*, this is a remarkable result—resonant tunnelling not only implies that individual molecular orbitals carry the current, but also that these orbitals maintain phase coherence and extend over a distance of at least 140 nm (the distance between contacts). At higher bias voltages, conduction via higher-lying energy levels was observed. For a finite-length tube, the component of momentum *along* the axis of the tube is also quantized, with a spacing between energy levels of $hv_F/2L$ where $v_F$ is the Fermi velocity and $L$ is the length of the tube. The energy level spacing measured by Tans *et al* was consistent with the value expected from this simple formula.

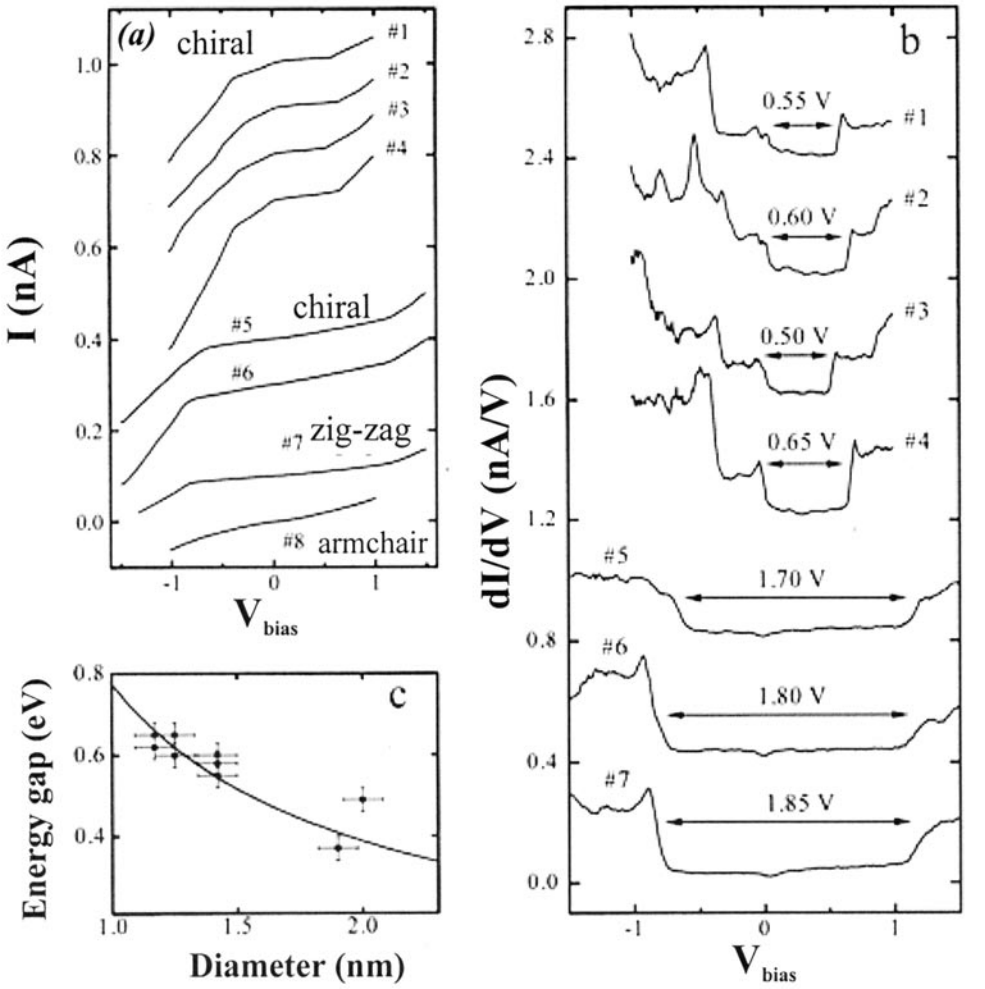


**Figure 51.** (a) Scanning tunnelling spectra of various carbon nanotubes. Tubes 1–6 are chiral whereas 7 and 8 are zigzag and armchair respectively. (b) $\mathrm{d}I/\mathrm{d}V$ plots which provide a measure of the tube density of states. (c) Energy gap versus diameter for semiconducting chiral tubes. (d) Normalized differential conductance $((\mathrm{d}I/\mathrm{d}V)/(I/V))$ spectra for nanotube No 9. Sharp peaks are observed which closely match the shape of the theoretical density-of-states curve shown in the inset to the right. (The peaks arise from the $1/\sqrt{E}$ dependence of the 1D density of states.) The left inset shows the raw $\mathrm{d}I/\mathrm{d}V$ data. See the text for more details (Wildöer *et al* (1998); figure downloaded from C Dekker's online seminar at http://online.itp.ucsb.edu/online/qhall_c98/dekker/).

Following closely on the publication of the data described above, theoretical work (White and Todorov 1998) showed that electron transport through a small-diameter armchair tube (such as that studied by Tans *et al*) is ballistic even in the presence of weak disorder (induced by, for example, physisorption on a substrate). Furthermore, a striking conclusion drawn from the results of these calculations was that conduction electrons in armchair nanotubes subject to a fixed amount of disorder will have mean free paths that *increase* with tube diameter. It was predicted that the typical armchair nanotubes studied experimentally would have exceptional ballistic transport properties with localization lengths in excess of 10 $\mu$m!

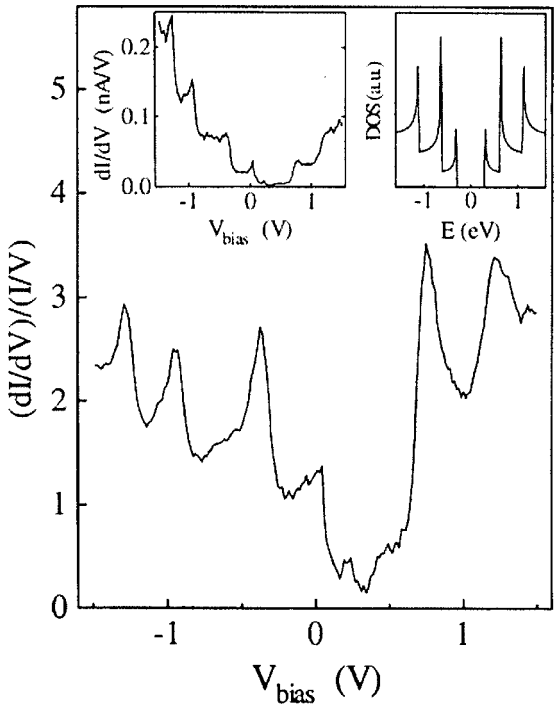


(d)

**Figure 51.** (Continued)

(Resistance increases with localization length, $\xi$, as $R(L) \sim e^{L/\xi}$ where $L$ is the length of the 1D system.)

The transport measurements and calculations discussed above implicitly assumed that individual electrons within nanotubes did not interact (although the authors of the theoretical work described in the previous paragraph stressed that they did not expect electron–electron interactions to alter their conclusions). However, comprehensive magnetotransport measurements (Tans *et al* 1998a) pointed to significant electron–electron correlations in metallic SWNTs. At low magnetic fields, all electrons enter a nanotube *with the same spin*—i.e. the nanotube is spin polarized and, in a one-electron picture, this is possible only if significant exchange interactions are present. A number of other measurements, in particular, the ability to flip spin states via changes in the gate voltage, could not be explained on the basis of one-electron states and it was proposed that the capacitance of the tube depends on its many-body quantum state. Very recently, Bockrath *et al* (1999) have carried out transport measurements on nanotube bundles (although a seemingly valid assumption is that the transport properties are dominated by the contribution of a single tube) which provide strong evidence that electrons in nanotubes behave as a Luttinger liquid (Egger and Gogolin 1997, Kane *et al* 1997)

Following the demonstration of spin-polarized transport in SWNTs by Tans *et al* (1998a), Tsukagoshi *et al* (1999) injected spin-polarized electrons from ferromagnetic contacts into a metallic nanotube, finding that the spin scattering length was at least 130 nm. A theoretical investigation of nanotube-based spin-polarized tunnel junctions has elucidated the transport mechanisms underlying the spin-valve effect observed experimentally (Mehrez *et al* 2000).

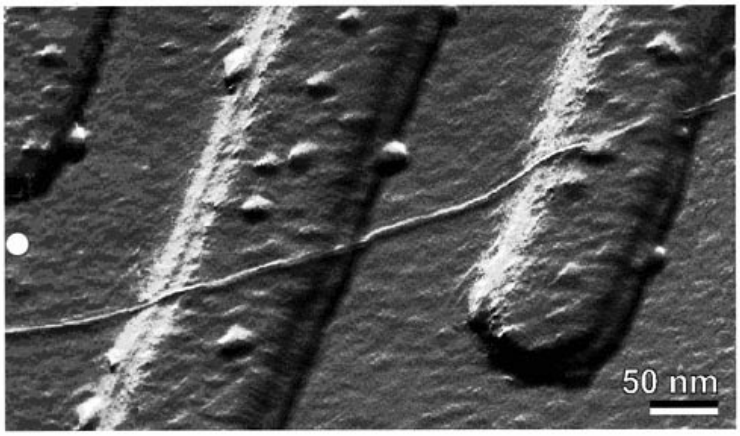


(a)

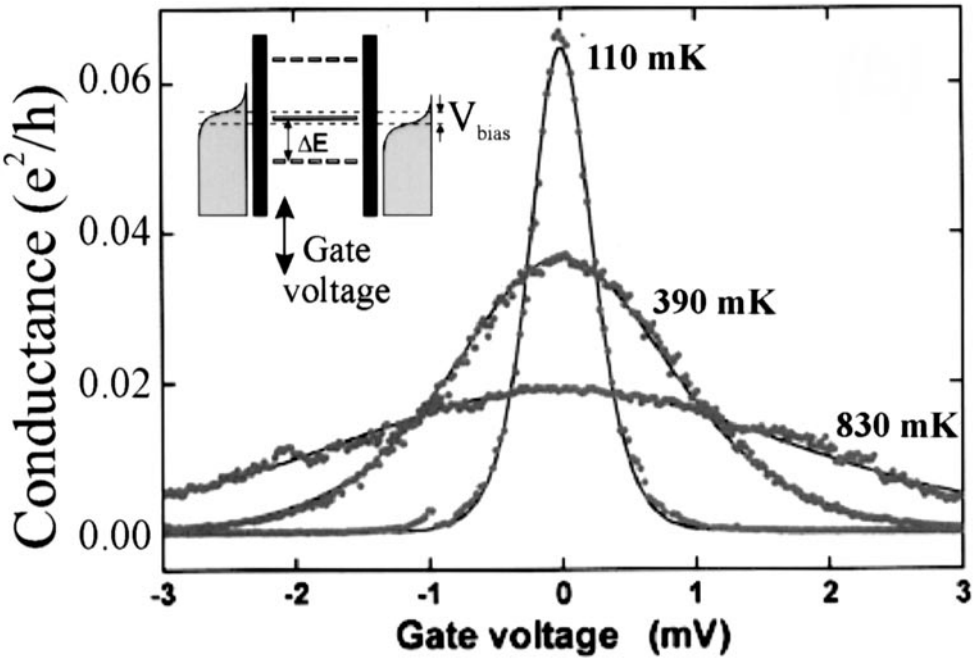


(b)

**Figure 52.** (a) An AFM tapping mode image of a carbon nanotube on top of a $Si/SiO_2$ substrate with two 15 nm thick Pt electrodes. (b) Conductance versus gate voltage at low bias voltage for the tube shown in (a). The solid lines are fits corresponding to a model of a single molecular level weakly coupled to two electrodes as depicted in the inset (Tans *et al* (1997); figure downloaded from C Dekker's online seminar at http://online.itp.ucsb.edu/online/qhall_c98/dekker/).

The work described thus far represents only a small amount of the wealth of exciting fundamental and applied physics that has been observed in nanotubes in recent years—a comprehensive discussion of nanotube science would require a separate review. From the fabrication of single-nanotube field-effect transistors (TUBEFETs) (Tans *et al* 1998b)—whose

operation seems to be describable within the same band-bending framework as is used for conventional semiconductor devices—and the synthesis of Y-junction nanotube 'interconnects' (Li *et al* 1999), to the observation of quantum interference within individual tubes (the Aharonov–Bohm effect) (Bachtold *et al* 1999) and the use of nanotubes as 'templates' for the fabrication of superconducting nanowires (Bezryadin *et al* 2000), the possibilities associated with exploiting nanotubes as core elements of carbon-based (nano)electronic devices seem limited almost only by the collective imagination of the nanoscale research community!

## 8. Conclusions and future prospects

This review has covered only a subset—albeit a broad and, I hope, representative subset—of the rapidly expanding body of literature on nanostructured materials. As discussed in the introduction, in focusing on nanoclusters the intent was to present the reader with a range of systems that exemplify fundamental nanoscale physical properties and behaviour. In addition, as illustrated throughout the review, nanocluster research has been at the heart of a vast amount of state-of-the-art nanoscience. A complementary branch of nanoscience, which has not (due to constraints of space) been covered in the review, involves the exploitation of organic molecules as the building blocks of nanostructured materials and as circuit elements (wires, logic gates, switches) in nanoscale devices. The work on carbon nanotubes discussed in section 7.2 represents one facet of this molecular approach. However, the broader topic of molecular electronics—first suggested in the 1970s (see, for example, Aviram and Ratner 1974)—has enjoyed a resurgence of interest of late. This has to some extent been driven by the syntheses of a molecular logic gate with chemically driven inputs and an optical (fluorescence) output (Credi *et al* 1997) and molecular systems which are capable of carrying out simple mathematical operations (DeSilva and McClenaghan 2000).

While both of the preceding examples have involved liquid-phase chemistry, solid-state molecular logic gates have recently been fabricated (Collier *et al* 1999). These were based on rotaxane molecules—novel 'axle-and-hoop' molecules first synthesized by Bissel *et al* (1994). When this ability to synthesize molecular logic gates is considered alongside the recent demonstration of single-molecule electrical measurements (Reed *et al* 1997, Tans *et al* 1997, Porath *et al* 2000, Fink and Schonenberger 1999) and the fabrication of single-molecule transistors (Tans *et al* 1998b, Joachim and Gimzewski 1997) it is clear that we are beginning to tap the potential of carbon-based materials as nanoscale circuit elements although there is obviously a vast amount of work to be done before organic molecules supersede, or even start to complement, Si technology on a commercial basis.

Concluding, and echoing a point made in the introduction, a large factor contributing to the advances in our understanding of materials at the nanometre level made over the past decade has been the strong cross-disciplinary character of nanoscientific research. In the decades to come, the continued convergence of the traditional physical, chemical and biological disciplines at the nanometre level will play a defining role in the evolution of fundamental and applied condensed matter science.

## Acknowledgments

I gratefully acknowledge the various researchers who have given permission for the reproduction of their results, figures and diagrams throughout this review.

## References


Abeln G C, Lee S Y, Lyding J W, Thompson D S and Moore J S 1997 *Appl. Phys. Lett.* **70** 2747
Alivisatos A P 1996 *Science* **271** 933
Alivisatos A P, Johnsson K P, Peng X G, Wilson T E, Loweth C J, Bruchez M P and Schultz P G 1996 *Nature* **382** 609
Almeida Murphy T, Pawlik T, Weidinger A, Höhne M, Alcala R and Spaeth J M 1996 *Phys. Rev. Lett*. **77** 1075
Altshuler B L, Lee P A and Webb R A (ed) 1991 *Mesoscopic Phenomena in Solids* (Amsterdam: Elsevier)
Alvarez M M, Khoury J T, Schaaf T G, Shafigullin M N, Vezmar I and Whetten R L 1997 *J. Phys. Chem.* B **101** 3706
Amlani I, Orlov A O, Toth G, Bernstein G H, Lent C S and Snider G L 1999 *Science* **284** 289
Andreoni W and Curioni A 1996 *Phys. Rev. Lett.* **77** 834
Andreoni W and Curioni A 1998 *Appl. Phys.* A **66** 299
Andreoni W, Gygi F and Parrinello M 1992 *Chem. Phys. Lett.* **190** 159
Andres R P, Bein T, Dorogi M, Feng S, Henderson J I, Kubiak C P, Mahoney W, Osifchin R G and Reifenberger R 1996a *Science* **272** 1323
Andres R P, Bielefeld J D, Henderson J I, Janes D B, Kolagunta V R, Kubiak C P, Mahoney W J and Osifchin R G 1996b *Science* **273** 1690
Antropov V P, Gunnarsson O and Jepsen O 1992 *Phys. Rev.* B **46** 13 647
Antropov V P, Gunnarsson O and Liechtenstein A I 1993 *Phys. Rev.* B **48** 7561
Arndt M, Nairz O, Vos-Andreae J, Keller C, van der Zouw G and Zeilinger A 1999 *Nature* **401** 680
Ashcroft N W and Mermin N D 1976 *Solid State Physics* (Philadelphia, PA: Saunders College Publishing)
Aviram A and Ratner M 1974 *Chem. Phys. Lett.* **29** 277
Avouris P and Lyo I W 1994 *Science* **264** 942
Awschalom D D and DiVincenzo D P 1995 *Phys. Today* **43** (4) 43
Awschalom D D, DiVincenzo D P and Smyth J F 1992a *Science* **258** 414
Awschalom D D and Kikkawa J M 1999 *Phys. Today* **52** (6) 33
Awschalom D D, Smyth J F, Grinstein G, DiVincenzo D P and Loss D 1992b *Phys. Rev. Lett.* **68** 3092
Bachtold A, Strunk C, Salvetat J-P, Bonard J M, Forró L, Nussbaumer T and Schönenberg C 1999 *Nature* **397** 673
Baibich M N, Broto J M, Fert A, Nguyen van Dau F, Petroff F, Etienne P, Creuzet G, Friederich A and Chazelas J 1988 *Phys. Rev. Lett.* **61** 2472
Baker S H, Thornton S C, Keen A M, Preston T I, Norris C, Edmonds K W and Binns C 1997 *Rev. Sci. Instrum.* **68** 1
Bakkers E P A M, Reitsma E, Kelly J J and Vanmaekelbergh D 1999 *J. Phys. Chem.* B **103** 2781
Banin U, Cao Y W, Katz D and Millo O 1999 *Nature* **400** 542
Banin U, Cerullo G, Guzelian A A, Bardeen C J, Alivisatos A P and Shank C 1997 *Phys. Rev.* B **55** 7059
Bardeen J 1947 *Phys. Rev.* **71** 717
Bardotti L, Jensen P, Hoareau A, Treilleux M and Cabaud B 1995 *Phys. Rev. Lett.* **74** 4694
Bäumer M and Freund H-J 1999 *Prog. Surf. Sci*. **61** 127
Bellouard C, Mirebeau I and Hennion M 1996 *Phys. Rev.* B **53** 5770
Belotskii E D and Tomchuck P M 1992 *Int. J. Electron.* **73** 955
Benning P J, Olson C G, Lynch D W and Weaver J H 1994 *Phys. Rev.* B **50** 11 239
Bethune D S, Johnson R D, Salem J R, de Vries M S and Yannoni C S 1993a *Nature* **366** 123
Bethune D S, Kinag C H, de Vries M S, Gorman G, Savoy R, Vazquez J and Beyers R 1993b *Nature* **363** 605
Beton P H, Dunn A W and Moriarty P 1995a *Appl. Phys. Lett.* **67** 1075
Beton P H, Wang J, Mori N, Eaves L, Main P C, Foster T J and Henini M 1995b *Phys. Rev. Lett.* **75** 1996
Bezryadin A, Dekker C and Schmid G 1997 *Appl. Phys. Lett.* **71** 1273
Bezryadin A, Lau C N and Tinkham M 2000 *Nature* **404** 971
Bigioni T P, Harrell L E, Cullen W G, Guthrie D E, Whetten R L and First P N 1999 *Eur. Phys. J.* D **6** 355
Binnig G, Rohrer H, Gerber Ch and Weibel E 1982a *Phys. Rev. Lett.* **49** 57
Binnig G, Rohrer H, Gerber Ch and Weibel E 1982b *Appl. Phys. Lett.* **40** 178
Binns C, Baker S H, Demangeat C and Parlebas J C 1999 *Surf. Sci. Rep.* **34** 105
Bissel R A, Cordova E, Kaifer A E and Stoddart J F 1994 *Nature* **369** 133
Blanton S A, Dehestani A, Lin P C and Guyotsionne P 1994 *Chem. Phys. Lett.* **229** 317
Bockrath M, Cobden D H, Lu J, Rinzler A G, Smalley R E, Balents L and McEuen P L 1999 *Nature* **397** 598
Bohren C F and Huffman D R 1983 *Absorption and Scattering of Light by Small Particles* (New York: Wiley)
Boland J J 1992 *Surf. Sci.* **261** 17
Brandt M S, Fuchs H D, Stutzmann M, Weber J and Cardona M 1992 *Solid State Commun.* **81** 307
Braun E, Eichen Y, Sivan U and Ben-Yoseph G 1998 *Nature* **391** 775
Brom H P, van Staveren M P J and de Jongh L J 1991 *Z. Phys.* D **20** 281
Brown W F 1963 *Phys. Rev*. **130** 1677

Bruchez M, Moronne M, Gin P, Weiss S and Alivisatos A P 1998 *Science* **281** 2013
Brühwiler P A, Maxwell A J, Rudolf P, Gutleben C D, Wästberg B and Mårtensson N 1993 *Phys. Rev. Lett.* **71** 3721
Brus L E 1984 *J. Chem. Phys.* **80** 4403
Brus L E 1986 *J. Phys. Chem.* **90** 2558
Brus L E 1991 *Appl. Phys.* A **53** 465
Brust M, Bethell D, Schiffrin D J and Kiely C J 1995 *Adv. Mater.* **7** 795
Brust M, Walker M, Bethell D, Schiffrin D J and Whyman R 1994 *J. Chem. Soc., Chem. Commun.* 801
Bryant G W 1998 *Appl. Phys. Lett.* **72** 768
Burrows V A, Chabal Y J, Higashi G S, Raghavachari K and Christman S B 1988 *Appl. Phys. Lett.* **53** 998
Butcher M J, Jones F H and Beton P H 2000 *J. Vac. Sci. Technol.* B **18** 13
Butcher M J, Jones F H, Beton P H, Moriarty P, Cotier B N, Upward M D, Prassides K, Kordatos K, Tagmatarchis N, Wudl F, Dhanak V, Johal T K, Crotti C, Comicioli C and Ottaviani C 1999 *Phys. Rev. Lett.* **83** 3478
Canham L T 1990 *Appl. Phys. Lett.* **57** 1046
Carroll S J, Hall S G, Palmer R E and Smith R 1998a *Phys. Rev. Lett.* **81** 3715
Carroll S J, Seeger K and Palmer R E 1998b *Appl. Phys. Lett.* **72** 305
Cepek C, Schiavuta P, Sancrotti M and Pedio M 1999 *Phys. Rev.* B **60** 2068
Chai Y, Guo T, Hjin C, Haufler R E, Chibante L P F, Fure J, Wang L, Alford J M and Smalley R E 1991 *J. Phys. Chem.* **95** 7564
Chan W C W and Nie S 1998 *Science* **281** 2016
Chang T and Zhu J G 1994 *J. Appl. Phys.* **75** 5553
Chase S J, Basca W S, Mitch M G, Pilione L J and Lannin J S 1992 *Phys. Rev.* B **46** 7873
Chen D, Chen J and Sarid D 1994 *Phys. Rev.* B **50** 10 905
Chen D and Sarid D 1994 *Phys. Rev.* B **49** 7612
Chen D and Sarid D 1995 *Surf. Sci.* **329** 206
Chey S J, Huang L and Weaver J H 1999 *Phys. Rev.* B **59** 16 033
Chi L F, Hartig M, Drechsler T, Schaak T, Seidel C, Fuchs H and Schmid G 1998 *Appl. Phys.* A **66** 187
Chou S Y, Krauss P R and Kong L 1996 *J. Appl. Phys.* **79** 6101
Chudnovsky E M and Gunther L 1988 *Phys. Rev. Lett.* **60** 661
Clark G W and Kesmodel L L 1993 *J. Vac. Sci. Technol.* B **11** 131
Collier C P, Wong E W, Belohradsky M, Raymo F M, Stoddart J F, Kuekes P J, Williams R S and Heath J R 1999 *Science* **285** 391
Connolly S and Fitzmaurice D 1999 *Adv. Mater.* **11** 1202
Cooper E B, Manalis S R, Fang H, Dai H, Matsumoto K, Minne S C, Hunt T and Quate C F 1999 *Appl. Phys. Lett.* **75** 3566
Copel M, Ruter M C, Vonhoegen M H and Tromp R M 1990 *Phys. Rev.* B **42** 11 682
Cotier B N C, Butcher M J, Hunt M R C, Moriarty P, Beton P H and Dhanak V R 2001 in preparation
Cowburn R P and Welland M E 2000 *Science* **287** 1466
Credi A, Balzani V, Langford S J and Stoddart J F 1997 *J. Am. Chem. Soc.* **119** 2679
Crommie M F, Lutz C P and Eigler D M 1993 *Science* **262** 218
Cuberes M T, Schlittler R R and Gimzewski J K 1996 *Appl. Phys. Lett.* **69** 3016
Cullis A G and Canham L T 1991 *Nature* **353** 225
Danek M, Jensen K F, Murray C B and Bawendi M G 1994 *Appl. Phys. Lett.* **65** 2795
de Heer W A 1993 *Rev. Mod. Phys.* **65** 611
Deng X and Krishnamurthy M 1998 *Phys. Rev. Lett.* **81** 1473
De Seta M, Sanvitto D and Evangelisti F 1999 *Phys. Rev.* B **59** 9878
DeSilva A P and McClenaghan N D 2000 *J. Am. Chem. Soc.* **122** 3965
Devoret M H and Grabert H (ed) 1992 *Single Charge Tunneling—Coulomb Blockade Phenomena in Nanostructures (NATO ASI Series vol 294)* (New York: Plenum)
Dinh L N, Chase L L, Balooch M, Terminello L J and Wooten F 1994 *Appl. Phys. Lett.* **65** 3111
Dinh L N, Hayes S, Saw C K, McLean W, Balooch M and Reimer J A 1999 *Appl. Phys. Lett.* **75** 2208
DiVincenzo D P and Loss D 1999 *J. Magn. Magn. Mater.* **200** 202
Doremus R H 1965 *J. Chem. Phys.* **42** 414
Dorogi M, Gomez J, Osifchin O and Andres R P 1995 *Phys. Rev.* B **52** 9071
Dresselhaus M S 1998 *Nature* **391** 19
Dresselhaus M S, Dresselhaus G and Eklund P C 1996 *Science of Fullerenes and Carbon Nanotubes* (San Diego, CA: Academic)
Dubois J G A, Gerritsen J W, Shafranjuk S W, Boon E J G, Schmid G and van Kempen H 1996 *Europhys. Lett.* **33** 279
Duke C B 1996 *Chem. Rev.* **96** 1237

Dumas Ph, Gruyters M, Rudolf P, He L M, Yu L M, Gensterblum G, Caudano R and Chabal Y J 1996 *Surf. Sci.* **368** 330
Dumas Ph, Gu M, Syrykh C, Gimzewski J K, Makarenko I, Halimaoui A and Slavan F 1993 *Europhys. Lett*. **23** 197
Dunn A W, Cotier B N, Nogaret A, Moriarty P, Beton P H and Beaumont S P 1997 *Appl. Phys. Lett.* **71** 2937
Durston P J, Schmidt J, Palmer R E and Wilcoxon J P 1997 *Appl. Phys. Lett.* **71** 2940
Ebbesen T W, Lezec H J, Hiura H, Bennet J W, Ghaemi H F and Thio T 1996 *Nature* **382** 54
Egger R and Gogolin A 1997 *Phys. Rev. Lett.* **79** 5082
Eigler D M and Schweizer E K 1990 *Nature* **344** 524
Eldridge M D, Madden P A and Frenkel D 1993 *Nature* **365** 35
Empedocles S A, Neuhauser R, Shimizu K and Bawendi M G 1999 *Adv. Mater.* **11** 1243
Empedocles S A, Norris D J and Bawendi M G 1996 *Phys. Rev. Lett.* **77** 3873
Faraday M 1857 *Phil. Trans. R. Soc.* **147** 145
Feenstra R M 1993 *Scanning Tunneling Microscopy* ed J A Stroscio and W J Kaiser (Boston, MA: Academic)
Feldheim D L, Grabar K C, Natan M J and Mallouk T E 1996 *J. Am. Chem. Soc.* **118** 7640
Feynman R P 1959 http://www.zyvex.com/nanotech/feynman.html (originally published in the February 1960 edition of the *Caltech Engineering and Science Journal*)
Field M, Smith C J, Awschalom D D, Mendelson N H, Mayes E L, Davis S A and Mann S 1998 *Appl. Phys. Lett.* **73** 1739 and references therein
Fink H W and Schonenberger C 1999 *Nature* **398** 407
Fischer J E 1997 *J. Phys. Chem. Solids* **58** 1939
Fishlock T W, Oral A, Egdell R G and Pethica J B 2000 *Nature* **404** 743
Flack F, Samarth N, Nikitin V, Crowell P A, Shi J, Lecy J and Awschalom D D 1996 *Phys. Rev.* B **54** R17 312
Fragstein C V and Kreibig U 1969 *Z. Phys.* **224** 307
Frei E H, Shtrikman S and Treves D 1957 *Phys. Rev.* **106** 446
Frens G 1973 *Nature Phys. Sci.* **241** 20
Freund H-J 1997 *Angew. Chem. Int. Edn Engl.* **36** 452
Ganz E, Sattler K and Clarke J 1988 *Phys. Rev. Lett.* **60** 1856
Ganz E, Sattler K and Clarke J 1989 *Surf. Sci.* **219** 33
Gay S C A and Srivastava G P 1999 *Surf. Sci.* **443** 253
Gensterblum G, Pireaux J-J, Thiry P A and Caudano R 1993 *Phys. Rev.* B **48** 14 756
Georgsson K, Carlsson N, Samuelson L, Seifert W and Wallenberg L R 1995 *Appl. Phys. Lett.* **67** 2981
Gider S, Awschalom D D, Douglas T, Mann S and Chaparala M 1995 *Science* **268** 77
Gimzewski J K, Modesti S and Schlittler R R 1994 *Phys. Rev. Lett.* **72** 1036
Gimzewski J K, Reihl B, Coombs J H and Schlittler R R 1998 *Z. Phys.* B **72** 497
Girifalco L A 1991 *J. Phys. Chem.* **95** 5370
Goldby I M, Kuipers L, von Issendorff and Palmer R E 1996 *Appl. Phys. Lett.* **69** 2819
Golden M S, Knupfer M, Fink J, Armbruster J F, Cummins T R, Romberg H A, Roth M, Sing M, Schmidt M and Sohmen E 1995 *J. Phys.: Condens. Matter* **7** 8219
Gorter C J 1951 *Physica* **17** 777
Grabar K C, Freeman R G, Hommer M B and Natan M J 1995 *Anal. Chem.* **67** 735
Green M and O'Brien P 1998 *Chem. Commun.* **22** 2459
Grünberg P 2000 *Acta Mater.* **48** 239
Grundmann M, Ledentsov N N, Heitz R, Eckey L, Christen J and Bimberg D 1994 *Phys. Status Solidi* b **118** 249
Gunnarsson O, Koch E and Martin R M 1996 *Phys. Rev.* B **54** R11 026
Guo T, Jin C and Smalley R E 1991 *J. Phys. Chem.* **95** 4948
Gurevich L, Canali L and Kouwenhoven L 1999 *Appl. Phys. Lett.* **76** 384
Gustafsson A, Pistol M E, Montelius L and Samuelson L 1998 *J. Appl. Phys.* **84** 1715
Guzelian A A, Banin U, Kadavanich A V, Peng X and Alivisatos A P 1996 *Appl. Phys. Lett.* **69** 1432
Hamad K S, Roth R, Rockenberger J, van Buuren T and Alivisatos A P 1999 *Phys. Rev. Lett.* **83** 3474
Hamada N, Sawada S-I and Oshiyama A 1992 *Phys. Rev. Lett.* **68** 1579
Hang S H and Mirkin C A 2000 *Science* **288** 1808
Harrell L E, Bigioni T P, Cullen W G, Whetten R L and First P N 1999 *J. Vac. Sci. Technol.* B **17** 2411
Hashizume T and Sakurai T 2000 *Advances in Scanning Probe Microscopy (Springer Advances in Materials Research Series)* ed T Sakurai and Y Watanabe (Berlin: Springer)
Hashizume T, Wang X D, Nishina Y, Shinohara H, Saito Y, Kuk Y and Sakurai T 1992 *Japan. J. Appl. Phys.* II **31**
Heath J R, Knobler C M and Leff D V 1997 *J. Phys. Chem.* B **101** 189
Heath J R, O'Brien S C, Zhang Q, Liu Y, Curl R F, Kroto H W, Tittl F K and Smalley R E 1985 *J. Am. Chem. Soc.* **107** 779

Heilweil E J and Hochstrasser R M 1985 *J. Chem. Phys.* **82** 4762
Heim D E, Fontana R E, Tsang C, Speriosu V, Gurney B A and Williams M L 1994 *IEEE Trans. Magn.* **30** 316
Hellier J, Turkevich J and Stevenson P C 1951 *Trans. Faraday Soc. Discuss.* **11** 55
Henini M, Sanguinetti S, Fortina S C, Grilli E, Guzzi M, Panzarini G, Andreani L C, Upward M D, Moriarty P, Beton P H and Eaves L 1998 *Phys. Rev.* B **57** R6815
Henry M E and Laughlin D E 2000 *Acta Mater.* **48** 223
Hersam M C, Guisinger N A and Lyding J W 2000 *Nanotechnology* **11** 70
Higashi G S, Becker R S, Chabal Y J and Becker A J 1991 *Appl. Phys. Lett.* **58** 1656
Hoogenboom B W, Hesper R, Tjeng L H and Sawatzky G A 1998 *Phys. Rev.* B **57** 11 939
Hovel H S, Fritz A H, Kreibig U and Vollmer M 1993 *Phys. Rev.* B **48** 18 178
Huang L, Chey S J and Weaver J H 1998 *Phys. Rev. Lett.* **80** 4095
Huffman D R 1990 *Optical Properties Associated with Small Particles* ed R K Chang and P N Barber (Singapore: World Scientific)
Huisken F, Kohn B and Paillard V 1999 *Appl. Phys. Lett.* **74** 3776
Hummeln J C, Knight B, Pavlovich J, Gonzalez R and Wudl F 1995 *Science* **269** 1554
Hunt M R C, Butcher M J, Cotier B N C, Moriarty P, Beton P H and Dhanak V R 2001 in preparation
Hunt M R C, Modesti S, Rudolf P and Palmer R E 1995 *Phys. Rev.* B **51** 10 039
Hunt M R C and Moriarty P 2001 in preparation
Hunt M R C and Palmer R E 1996 *Surf. Rev. Lett.* **3** 937
Hunt M R C, Rudolf P and Modesti S 1997a *Phys. Rev.* B **55** 7882
Hunt M R C, Rudolf P and Modesti S 1997b *Phys. Rev.* B **55** 7889
Iijima S 1991 *Nature* **354** 56
Iijima S and Ishihashi T 1993 *Nature* **363** 603
Imamoglu A, Awschalom D D, Burkard G, DiVincenzo D P, Loss D, Sherwin M and Small A 1999 *Phys. Rev. Lett.* **83** 4204
Ito K, Ohyama S, Uehara Y and Ushioda S 1995 *Appl. Phys. Lett.* **67** 2536
Jin G, Liu J L and Wang K L 2000 *Appl. Phys. Lett.* **76** 3591
Joachim C and Gimzewski J K 1997 *Chem. Phys. Lett.* **265** 353
Johansson M K J, Maxwell A J, Gray S M, Brühwiler P A and Johansson L S O 1998 *Surf. Sci.* **397** 314
Johnson R D, Bethune D S and Yannoni C S 1992a *Acc. Chem. Res.* **25** 169
Johnson R D, de Vries M S, Salem S, Bethune D S and Yannoni C S 1992b *Nature* **355** 239
Johnson R D, Meijer G and Bethune D S 1990 *J. Am. Chem. Soc.* **112** 8983
Jung T A, Schlittler R R, Gimzewski J K, Tang H and Joachim C 1996 *Science* **271** 181
Junno T, Deppert K, Montelius L and Samuelson L 1995 *Appl. Phys. Lett.* **66** 3627
Kane C, Balents L and Fisher M P A 1997 *Phys. Rev. Lett.* **79** 5086
Kanemitsu Y, Uto H, Masumoto Y, Matsumoto T, Futagi T and Mimura H 1993 *Phys. Rev.* B **48** 2827
Kästner M and Voigtländer B 1999 *Phys. Rev. Lett.* **82** 2745
Katari J E B, Colvin V L and Alivisatos A P 1994 *J. Phys. Chem.* **98** 4109
Kawabata A and Kubo R 1966 *J. Phys. Soc. Japan* **21** 1765
Kent A D, Shaw T M, von Molnár S and Awschalom D D 1993 *Science* **262** 1249
Kern R, Masson A and Metois J J 1979 *Current Topics in Materials Science* ed E Kaldis (Amsterdam: North-Holland)
Kessler B, Bringer A, Cramm S, Schlebusch C, Eberhardt W, Suzuki S, Achiba Y, Esch F, Barnaba M and Cocco D 1997 *Phys. Rev. Lett.* **79** 2289
Kiely C J, Fink J, Brust M, Bethell D and Schiffrin D J 1998 *Nature* **396** 444
Kiely C J, Fink J, Zheng J G, Brust M, Bethell D and Schiffrin D J 2000 *Adv. Mater.* **12** 640
Kikkawa J M and Awschalom D D 1999 *Nature* **397** 139
Klein D L, McEuen P L, Katari J E B and Alivisatos A P 1996a *Nanotechnology* **7** 397
Klein D L, McEuen P L, Katari J E B, Roth R and Alivisatos A P 1996b *Appl. Phys. Lett.* **68** 2574
Klein D L, Roth R, Lim A K L, Alivisatos A P and McEuen P L 1997 *Nature* **389** 699
Klyachko D and Chen D M 1997 *J. Vac. Sci. Technol.* B **15** 1295
Knall J and Pethica J B 1992 *Surf. Sci.* **265** 156
Kodama R H 1999 *J. Magn. Magn. Mater.* **200** 359
Kodama R H and Berkowitz A E 1999 *Phys. Rev.* B **59** 6321
Kodama R H, Berkowitz A E, McNiff A E and Foner S 1996 *Phys. Rev. Lett.* **77** 394
Kodama R H, Berkowitz A E, McNiff A E and Foner S 1997 *J. Appl. Phys.* **81** 5552
Kouwenhoven L and Marcus C 1998 *Phys. World* **11** (6) 6
Krätschmer W, Lamb L D, Fostiropoulos P and Huffman D R 1990 *Nature* **347** 354
Kreibig U and Genzel U 1985 *Surf. Sci.* **156** 678

Kreibig U and Vollmer M 1995 *Optical Properties of Metal Clusters* (Berlin: Springer)
Kroto H W 1987 *Nature* **329** 529
Kroto H W, Heath J R, O'Brien S C, Curl R F and Smalley R E 1985 *Nature* **318** 162
Kubo R, Kawabata A and Kobayashi S 1984 *Annu. Rev. Mater. Sci.* **14** 49
Kuk Y, Jarrold M F, Silverman P J, Bower J E and Brown W L 1989 *Phys. Rev.* B **39** 11 168
Langer L, Bayot V, Grivei E, Issi J P, Heremans J P, Olk C H, Stockman L, VanHaesendonck C and Bruynseraede Y 1996 *Phys. Rev. Lett.* **76** 479
Ledermann M, Schultz S and Ozaki 1994 *Phys. Rev. Lett.* **73** 1986
Lee H J and Ho W 1999 *Science* **286** 1719
Leonard D, Pond K and Petroff P M 1994 *Phys. Rev.* B **50** 11 687
Li J, Papadopoulos C and Xu J 1999 *Nature* **402** 253
Li S P, Lew W S, Xu Y B, Hirohata A, Samad A, Baker F and Bland J A C 2000 *Appl. Phys. Lett.* **76** 748
Lindahl J, Pistol M-E, Montelius L and Samuelson L 1996 *Appl. Phys. Lett.* **68** 60
Link S and El-Sayed M A 1999 *J. Phys. Chem.* B **103** 4212
Littau K A, Szajowski P J, Muller A J, Kortan A R and Brus L E 1993 *J. Phys. Chem.* **97** 1224
Lof R W, van Veenendaal M A, Koopmans B, Jonkman H T and Sawatzky G A 1992 *Phys. Rev. Lett.* **68** 3924
Logunov S L, Ahmadi T S, El-Sayed M A, Khoury J T and Whetten R L 1997 *J. Phys. Chem.* B **101** 3713
Lopinski G P, Wayner D D M and Wolkow R A 2000 *Nature* **406** 48
Lu J P 1994 *Phys. Rev.* B **49** 5687
Luedtke W D and Landman U 1996 *J. Phys. Chem.* **100** 13 323
Lüth H 1997 *Surfaces and Interfaces of Solid Materials* (Berlin: Springer)
Majetich S A and Jin Y 1999 *Science* **284** 470
Manoharan H C, Lutz C P and Eigler D M 2000 *Nature* **403** 512
Markovich G, Collier C P and Heath J R 1998 *Phys. Rev. Lett.* **80** 3807
Marsen B and Sattler K 1999 *Phys. Rev.* B **60** 11 593
Maxwell A J, Brühwiler P A, Nilsson A, Mårtensson N and Rudolf P 1994 *Phys. Rev.* B **49** 10 717
McComb D W, Collings B A, Wolkow R A, Moffatt D J, MacPherson C D, Rayner D M, Hackett P A and Hulse J E 1996 *Chem. Phys. Lett.* **251** 8
McEuen L 1997 *Science* **278** 1682
Medeiros-Ribeiro G, Kamins T I, Ohlberg D A A and Williams R S 1999 *Mater. Sci. Eng.* B **67** 31
Mehrez H, Taylor J, Guo H, Wang J and Roland C 2000 *Phys. Rev. Lett.* **84** 2682
Meirav U and Foxman E B 1995 *Semicond. Sci. Technol.* **10** 255
Merkel M, Knupfer M, Golden M S, Fink J, Seeman R and Johnson R L 1993 *Phys. Rev.* B **47** 11 470
Mews A, Eychmüller A, Gietrseg M, Schoos D and Weller H 1994 *J. Phys. Chem.* **98** 934
Micic O I, Curtis C J, Jones K M, Sprague J R and Nozik A J 1994 *J. Phys. Chem.* **98** 4966
Micic O I, Jones K M, Cahill A and Nozik A J 1998 *J. Phys. Chem.* B **102** 9791
Micic O I and Nozik A J 1996 *J. Lumin.* **70** 95
Micic O I, Sprague J R, Lu Z and Nozik A J 1996 *Appl. Phys. Lett.* **68** 3150
Mie G 1908 *Ann. Phys., Lpz.* **25** 377
Millo O, Katz D, Cao Y and Banin U 2000 *Phys. Rev.* B **61** 16 773
Mintmire J W, Dunlap B I and White C T 1992 *Phys. Rev. Lett.* **68** 631
Mintmire J W and White C T 1995 *Carbon* **33** 893
Mirkin C A 2000 *Inorg. Chem* **39** 2258
Mirkin C A, Letsinger R L, Mucic R C and Storhoff J J 1996 *Nature* **382** 607
Mitchell G P, Mirkin C A and Letsinger R L 1999 *J. Am. Chem. Soc*. **121** 8122
Mizes H A and Foster J S 1989 *Science* **244** 559
Mo Y-W, Savage D E, Swartzentruber R S and Lagally M G 1990 *Phys. Rev. Lett.* **65** 1020
Modesti S, Cerasari S and Rudolf P 1993 *Phys. Rev. Lett.* **71** 2469
Moerner W E 1994 *Science* **265** 46
Moriarty P, Ma Y R, Upward M D and Beton P H 1998a *Surf. Sci.* **407** 27
Moriarty P, Ma Y R, Upward M D and Beton P H 1998b unpublished
Moriarty P, Upward M D, Dunn A W, Ma Y-R, Beton P H and Teehan D 1998c *Phys. Rev.* B **57** 362
Mui D S L, Leonard D, Coldren L A and Petroff P M 1995 *Appl. Phys. Lett.* **66** 1620
Murray C B, Kagan C R and Bawendi M G 1995 *Science* **270** 1335
Murray C B, Norris D B and Bawendi M G 1993 *J. Am. Chem. Soc.* **115** 8706
Murray P W, Pederson M Ø, Læsgaard E, Stensgaard I and Besenbacher F 1997 *Phys. Rev.* B **55** 9360
Néel L 1949 *Ann. Geophys.* **5** 99
Neugebauer C A and Webb M B 1962 *J. Appl. Phys.* **33** 74

Ngo T T, Petroff P M, Sakaki H and Merz J L 1996 *Phys. Rev.* B **53** 9618
Nilius N, Ernst N and Freund H-J 2000 *Phys. Rev. Lett.* **84** 3994
Nirmal M, Murray C B and Bawendi M G 1994 *Phys. Rev.* B **50** 2293
Norris D J and Bawendi M G 1996 *Phys. Rev.* B **53** 16 338
Norris D J, Efros A L, Rosen M and Bawendi M G 1996 *Phys. Rev.* B **53** 16 347
Nötzel R, Fukui T, Hasegawa H, Temmyo J and Tamamura T 1994a *Appl. Phys. Lett.* **65** 2854
Nötzel R, Temmyo J and Tamamura T 1994b *Nature* **369** 131
Nozik A J and Micic O I 1998 *MRS Bull.* **23** 24
O'Barr R, Yamamoto S Y, Schultz S, Xu W and Scherer A 1997 *J. Appl. Phys.* **81** 4730
Odom T W, Huang J-L, Kim P and Lieber C M 1998 *Nature* **391** 62
Oepen H P and Kirschner J 1999 *Curr. Opin. Solid State Mater. Sci.* **4** 217
Ogawa S, Fan F-R F and Bard A J 1995 *J. Phys. Chem.* **99** 11 182
Oghi T, Sheng H-Y and Nejoh H 1998 *Appl. Surf. Sci.* **130** 919
Ohara P C, Leff, D V, Heath J R and Gelbart W M 1995 *Phys. Rev. Lett.* **75** 3466
Ohno H 1998 *Science* **281** 951
Ohno T R, Chen Y, Harvey S E, Kroll G H, Weaver J H, Haufler R E and Smaller R E 1991 *Phys. Rev.* B **44** 13 747
Ohno Y, Young D K, Beschoten B, Matsukura F, Ohno H and Awschalom D D 1999 *Nature* **402** 790
Olshavsky M A, Goldstein A N and Alivisatos A P 1990 *J. Am. Chem. Soc.* **112** 9438
Oshiyama A, Saito S, Hamada N and Miyamoto Y 1992 *J. Phys. Chem. Solids* **53** 1457
Palasantzas G, Ilge B, DeNijs J and Geerligs L J 1999 *J. Appl. Phys.* **85** 1907
Papavassiliou G C 1980 *Prog. Solid State Chem.* **12** 185
Park K-H, Ha J S, Yun W S and Lee E H 1998 *Surf. Sci.* **405** 46
Peng X G, Manna L, Yang W D, Wickham J, Scher E, Kadavanich A and Alivisatos A P 2000 *Nature* **404** 59
Persson N J 1993 *Surf. Sci.* **281** 153
Pesci A, Ferrari L, Comicioli C, Pedio M, Cepek C, Schiavuta P, Pivetta M and Sancrotti M 2000 *Surf. Sci.* **454** 832
Petit C, Cren T, Roditchev D, Sacks W, Klein J and Pileni M P 1999a *Adv. Mater.* **11** 1198
Petit C, Taleb A and Pileni M P 1998 *Adv. Mater.* **10** 259
Petit C, Taleb A and Pileni M P 1999b *J. Phys. Chem.* B **103** 1805
Pichler T, Golden M S, Knupfer M, Fink J, Kirbach U, Kuran P and Dunsch L 1997a *Phys. Rev. Lett.* **79** 3026
Pichler T, Golden M S, Kuran P, Dunsch L, Knupfer M, Fink J, Hunt M R C, Rudolf P, Inakuma M and Shinohara H 1999 *Proc. Electronic Properties of Novel Materials—Science and Technology of Molecular Nanostructures (Kirchberg, Austria)*
Pichler T, Knupfer M, Golden M S, Haffner S, Friedlein R, Fink J, Andreoni W and Curioni A 1997b *Phys. Rev. Lett.* **78** 4249
Piednoir A, Perrot E, Granjeaud S, Humbert A, Chapon C and Henry C R 1997 *Surf. Sci.* **391** 19
Pietzak B, Waiblinger M, Almeida Murphy T, Weidinger A, Höhne M, Dietel E and Hirsch A 1998 *Carbon* **36** 613
Pohl D W 1995 *Thin Solid Films* **264** 250
Poirier D M, Knupfer M, Weaver J H, Andreoni W, Laasonen K, Parrinello M, Bethune D S, Kikuchi K and Achiba Y 1994 *Phys. Rev.* B **49** 17 403
Porath D, Bezryadin A, de Vries S and Dekker C 2000 *Nature* **403** 635
Porath D and Millo O 1997 *J. Appl. Phys.* **81** 2241
Pradeep T, Vijayakrishnan V, Santra A K and Rao C N R 1991 *J. Phys. Chem.* **95** 10 564
Prinz G A 1998 *Science* **282** 1660
Prinz G A 1999 *J. Magn. Magn. Mater.* **200** 57
Roberti T W, Smith B A and Zhang J Z 1995 *J. Chem. Phys.* **102** 3860
Ross F M, Tersoff J and Tromp R M 1998 *Phys. Rev. Lett.* **80** 984
Rosseinsky M J 1998 *Chem. Mater.* **10** 2665
Ruan L and Chen D M 1997 *Surf. Sci.* **393** L113
Ruebsam M, Schweitzer P and Dinse K P 1996 *Fullerenes and Fullerene Nanostructures* ed H Kuzmany (London: World Scientific)
Saito R, Fujita M, Dresselhaus G and Dresselhaus M S 1992 *Appl. Phys. Lett.* **60** 204
Saito S and Oshiyama A 1991 *Phys. Rev. Lett.* **66** 2637
Sakamoto K, Harada M, Kondo D, Kimura A, Kakizaki A and Suto S 1998 *Phys. Rev.* B **58** 13 951
Sakurai T, Wang X D, Xue Q K, Hasegawa Y, Hashizume T and Shinohara H 1996 *Prog. Surf. Sci.* **51** 263
Salling C, O'Barr R, Schultz S, McFayden I and Ozaki M 1994 *J. Appl. Phys.* **75** 7989
Sanvitto D, De Seta M and Evangelisti F 2000 *Surf. Sci.* **452** 191
Sato T, Ahmed H, Brown D and Johnson B F G 1997 *J. Appl. Phys.* **82** 696
Sattler K 1995 *Carbon* **33** 915

Schaaf T G, Shafigullin M N, Khoury J T, Vezmar I, Whetten R L, Cullen W G, First P N, Gutiérrez-Wing C, Ascensio J and Jose-Yacamán M J 1997 *J. Phys. Chem.* B **101** 7885
Scheier P, Marsen B, Lonfat M, Schneider W-D and Sattler K 2000 *Surf. Sci.* **458** 113
Schmalz T G, Seitz W A, Klein D J and Hite G E 1988 *J. Am. Chem. Soc.* **110** 1113
Schmid G and Chi L F 1998 *Adv. Mater.* **10** 515
Schmid G, Pfeil R, Boese R, Bandermann F, Meyer S, Calis S G and van der Velden J W A 1981 *Chem. Ber.* **114** 5634
Schuller I K, Kim S and Leighton C 1999 *J. Magn. Magn. Mater.* **200** 571
Schwarz U D, Allers W, Gensterblum G, Pireaux J J and Wiesendanger R 1995 *Phys. Rev.* B **52** 5967
Shchukin V A, Ledentsov N N, Kop'ev P S and Bimberg D 1995 *Phys. Rev. Lett.* **75** 2968
Shen T C, Wang C, Abeln G C, Tucker J R, Lyding J W, Avouris Ph and Walkup R E 1995 *Science* **268** 1590
Shi J, Gider S, Babcock K and Awschalom D D 1996 *Science* **271** 936
Shinohara H 2000 *Rep. Prog. Phys.* **63** 843
Shinohara H, Inakuma M, Kishida M, Yamazaki S, Hashizume T and Sakurai T 1995 *J. Phys. Chem.* **99** 13 769
Shinohara H, Sato H, Ohchochi M, Ando Y, Kodama T, Shida T, Kato T and Saito Y 1992 *Nature* **357** 52
Shirley E L and Louie S G 1993 *Phys. Rev. Lett.* **71** 133
Silly F, Gusev A O, Taleb A, Charra F and Pileni M P 2000 *Phys. Rev. Lett.* **84** 5840
Simon U, Flesch R, Wiggers H, Schon G and Schmid G 1998 *J. Mater. Chem.* **8** 517
Srivastava G P 1997 *Rep. Prog. Phys.* **60** 561
Stella A, Nisoli M, De Silvestri S, Svelto O, Lanzani G, Cheyssac P and Kofman R 1996 *Phys. Rev.* B **53** 15 497
Stevenson S, Rice G, Glass T, Harich K, Cromer F, Jordan M R, Craft J, Hadju H, Bible S, Olmstead M M, Maitra A, Fisher A J, Balch A L and Dorn H C 1999 *Nature* **401** 55
Stoner E C and Wohlfarth E P 1948 *Phil. Trans. R. Soc.* A **240** 599
Stroscio J A and Kaiser W J (ed) 1993 *Scanning Tunneling Microscopy* (Boston, MA: Academic)
Sun S H and Murray C B 1999 *J. Appl. Phys.* **85** 4325
Sun S H, Murray C B, Weller D, Folks L and Moser A 2000 *Science* **287** 1989
Suto S, Sakamoto K, Wakita T, Hu C W and Kasuya A 1997 *Phys. Rev.* B **56** 7439
Taleb A, Petit C and Pileni M P 1997 *Adv. Mater.* **9** 950
Taleb A, Silly F, Gusev A O, Charra F and Pileni M P 2000 *Adv. Mater.* **12** 633
Tans S J 1997 *PhD Thesis* Delft University of Technology
Tans S J, Devoret M H, Dai H, Thess A, Smalley R E, Geerligs L J and Dekker C 1997 *Nature* **386** 474
Tans S J, Devoret M H, Groeneveld R J A and Dekker C 1998a *Nature* **394** 761
Tans S J, Verscheuren A R M and Dekker C 1998b *Nature* **393** 49
Taylor M D R, Moriarty P and Brust M 2000a unpublished
Taylor M D R, Moriarty P, Cotier B N, Butcher M J, Beton P H and Dhanak V R 2000b *Appl. Phys. Lett.* **77** 1144
Taylor R, Hare J P, Abdul Sada and Kroto H W 1990 *J. Chem. Soc., Chem. Commun.* **20** 1423
Terrill R H, Postlethwaite T A, Chen C H, Poon C D, Terzis A, Chen A D, Hutchison J E, Clark M R, Wignall G, Londono J D, Superfine R, Falvo M, Johnson C S, Samulski E T and Murray R W 1995 *J. Am. Chem. Soc.* **117** 12 537
Tjeng L H, Hesper R, Heessels A C L, Heeres A, Jonkman H T and Sawatzky G A 1997 *Solid State Commun.* **103** 31
Tölkes C, Zeppenfeld P, Krzyowski M A, David R and Comsa G 1997 *Phys. Rev.* B **55** 13 932
Trindade T, O'Brien P and Zhang X-M 1997 *Chem. Mater.* **9** 523
Tsue K-D, Yuh J-Y, Tzeng C-T, Chu R-Y, Chung S-C and Tsang K-L 1997 *Phys. Rev.* B **23** 15 412
Tsukagoshi K, Alphenaar B W and Ago H 1999 *Nature* **401** 572
Tycko R, Dabbagh G, Fleming R M, Haddon R C, Makhija A V and Zahurak S M 1991 *Phys. Rev. Lett.* **67** 1886
Uchida H, Curtis C J, Kamat P V, Jones K M and Nozik A J 1992 *J. Phys. Chem.* **96** 1156
Uchida H, Curtis C J and Nozik A J 1991 *J. Phys. Chem.* **95** 5382
Upward M D, Moriarty P and Beton P H 1997a *Phys. Rev.* B **56** R1704
Upward M D, Moriarty P, Beton P H, Baker S H, Binns C and Edmonds K W 1997b *Appl. Phys. Lett.* **70** 2114
van Kempen H, Dubois J G A, Gerritsen J W and Schmid G 1995 *Physica* B **204** 51
Vdovin E E, Levin A, Patanè A, Eaves L, Main P C, Khanin Y N, Dubrovskii Y V, Henini M and Hill G 2001 *Science* at press
Vettiger P, Despont M, Drechsler U, Durig U, Haberle W, Lutwyche M I, Rothuizen M E, Stutz R, Widmer R and Binnig G K 2000 *IBM J. Res. Dev.* **44** 323
Voigtländer B, Meyer G and Amer N M 1991 *Phys. Rev.* B **44** 10 354
Wang H, Hou J G, Takeuchi O, Fujisuku Y and Kawazu A 2000 *Phys. Rev.* B **61** 2199
Wang X D, Hashizume T, Shinohara H, Saito Y, Nishina Y and Sakurai T 1992 *Japan. J. Appl. Phys.* II **31** 1983
Weaver J H 1992 *Carbon* **30** 263
Weaver J H, Chai Y, Kroll G H, Jin C, Ohno T R, Haufler R E, Guo T, Alford J M, Conceicao J, Chibante L P F, Jain

A, Palmer G and Smalley R E 1992 *Chem. Phys. Lett.* **190** 460
Weaver J H, Martins J L, Komeda T, Chen Y, Ohno T R, Kroll G H, Troullier N, Haufler R E and Smalley R E 1991 *Phys. Rev. Lett.* **66** 1741
Weaver J H and Poirier D M 1994 *Solid State Physics* vol 48 (New York: Academic) p 1
Weisbuch C and Vinter B 1991 *Quantum Semiconductor Structures: Fundamentals and Applications* (London: Academic)
Wernsdorfer W, Doudin B, Mailly D, Hasselbach K, Benoit A, Meier J, Ansermet J-P and Barbara B 1996 *Phys. Rev. Lett.* **77** 1873
Wernsdorfer W, Hasselbach K, Benoit A, Barbara B, Doudin B, Meier J, Ansermet J-P and Mailly D 1997a *Phys. Rev.* B **55** 11 552
Wernsdorfer W, Hasselbach K, Mailly D, Barbara B, Benoit A, Thomas L and Suran S 1995 *J. Magn. Magn. Mater.* **145** 33
Wernsdorfer W, Orozco E B, Barbara B, Hasselbach K, Benoit A, Mailly D, Doudin B, Meier J, Wegrowe J E, Ansermet J P, Demoncy N, Pascard H, Demoncy N, Loiseau A, Francois L, Duxin N and Pileni M P 1997b *J. Appl. Phys.* **81** 5543
Wernsdorfer W, Orozco E B, Hasselbach K, Benoit A, Barbara B, Demoncy N, Loiseau A, Pascard H and Mailly D 1997c *Phys. Rev. Lett.* **78** 1791
Wernsdorfer W, Orozco E B, Hasselbach K, Benoit A, Mailly D, Kubo O, Nakano H and Barbara B 1997d *Phys. Rev. Lett.* **79** 4014
Wertheim G K and Buchanan D N E 1994 *Phys. Rev.* B **50** 11 070
Whetten R L, Khoury J T, Alvarez M M, Murthy S, Vezmar I, Wang Z L, Stephens P W, Cleveland C L, Luedtke W D and Landman U 1996 *Adv. Mater.* **8** 428
White C T and Todorov T N 1998 *Nature* **393** 240
Wiesendanger R 1994 *Scanning Probe Microscopy and Spectroscopy: Methods and Applications* (Cambridge: Cambridge University Press)
Wilcoxon J P, Martin J E, Parsapour F, Wiedenman B and Kelley D F 1998 *J. Chem. Phys.* **108** 9137
Wilcoxon J P, Williamson R L and Baughman R 1993 *J. Chem. Phys.* **98** 9933
Wildöer J W G, Venema L C, Rinzler A G, Smalley R E and Dekker C 1998 *Nature* **391** 59
Winningham T A, Gillis H P, Choutov D A, Martin K P, Moore J T and Douglas K 1998 *Surf. Sci.* **406** 221
Wirth S, von Molnár S, Field M and Awschalom D D 1999 *J. Appl. Phys.* **85** 5249
Wong W, Sheehan P E and Lieber C M 1997 *Science* **277** 1971
Woodruff D P and Delchar T A 1994 *Modern Techniques of Surface Science* (Cambridge: Cambridge University Press)
Wu J, Shen Z X, Dessau D S, Cao R, Marshall D S, Pianetta P, Lindau I, Yang X, Terry J, King D M, Wells B O, Elloway D, Wendt H R, Brown C A, Hunziker H and deVries M S 1992 *Physica* C **197** 251
Xhie J, Sattler K, Müller U, Venkateswaran N and Raina G 1991 *Phys. Rev.* B **43** 8917
Xie Q, Kobayashi N P, Ramachandran T R, Kalburge A, Chen P and Madhukar A 1996 *J. Vac. Sci. Technol.* B **14** 2203
Xie Q, Madhukar A, Chen P and Kobayashi N 1995 *Phys. Rev. Lett.* **75** 2542
Xin S H, Wang P D, Yin A, Kim C, Dobrowolska M, Merz J L and Furdyna J K 1996 *Appl. Phys. Lett.* **69** 3884
Xu H and Ng K Y S 1995 *J. Vac. Sci. Technol.* B **13** 2160
Xu H and Ng K Y S 1997 *J. Vac. Sci. Technol.* B **15** 186
Xu W, Wong J, Cheng C C, Johnson R and Scherer A 1995 *J. Vac. Sci. Technol.* B **13** 2372
Yamaguchi H, Fahy M R and Joyce B A 1996 *Appl. Phys. Lett.* **69** 776
Yamanaka K, Suzuki K, Ishida S and Arakawa Y 1998 *Appl. Phys. Lett.* **73** 1460
Yao Z, Postma H W C, Balents L and Dekker C 1999 *Nature* **402** 273
Yoon B, Akulin V M, Cahuzac P, Carlier F, de Frutos M, Masson A, Mory C, Colliex C and Brechignac C 1999 *Surf. Sci.* **443** 76
Zhang Z and Lieber C M 1993 *Appl. Phys. Lett.* **62** 2792
Zrenner A 2000 *J. Chem. Phys.* **112** 7790